DEVELOPMENT AND CHARACTERIZATION OF AUTO-LOCKED LASER SYSTEMS AND APPLICATIONS TO PHOTON ECHO LIFETIME MEASUREMENTS

HERMINA C. BEICA

A DISSERTATION SUBMITTED TO THE FACULTY OF GRADUATE STUDIES
IN PARTIAL FULFILMENT OF THE REQUIREMENTS
FOR THE DEGREE OF

DOCTOR OF PHILOSOPHY

GRADUATE PROGRAM IN PHYSICS AND ASTRONOMY
YORK UNIVERSITY
TORONTO, ONTARIO
SEPTEMBER 2019

Abstract

We have developed and characterized a new class of vacuum-sealed, auto-locking diode laser systems with an auto-locking controller that allows these instruments to be operated with greater ease and control at desired wavelengths in the visible and near-infrared spectral range. These laser systems can be tuned and frequency stabilized with respect to atomic, molecular, and solid-state resonances without human intervention using a variety of control algorithms programmed into the same controller. We show that these lasers have exceptional long-term stability, with an Allan deviation (ADEV) floor of 2×10^{-12}, and a short-term linewidth of 200 kHz. These performance characteristics are related to reducing current noise and ensuring vacuum sealing. We demonstrate accurate measurements of gravitational acceleration at the level of a few parts-per-billion by incorporating the laser into an industrial gravimeter. We also realize the basis of a LIDAR transmitter that can potentially operate in a spectral range in which frequency references are not readily available.

We have also developed a technique for precise measurements of atomic lifetimes

using optical photon echoes. We report a measurement of (26.10 ± 0.03) ns for the $5^2P_{3/2}$ excited state in ^{85}Rb vapour that has a statistical uncertainty of 0.11% in 4 hours of data acquisition over several weeks. We show that the best statistical uncertainty that can be obtained with the current configuration is 0.013%, which has been exceeded by only one other lifetime measurement. An analysis of the technical limitations based on a simple model shows that these limitations can be overcome using a feedback loop with a reference interferometer. Our studies indicate that it should be possible to investigate systematic effects at the level of 0.03% in 10 minutes of data acquisition. Such an outcome could potentially result in the most accurate measurement of any atomic lifetime.

Other applications of the laser systems include the development of free-space optical dipole force traps. Determinations of the spring constant of the trap and the time constant of the auto-correlation function of trapped particles have paved the way for experiments in which the kinematics can be studied on the time scale of the damping time associated with Brownian motion. These results may be applicable for the rapid in situ identification of trapped particles. Finally, we show that the laser systems can support a number of upper-level undergraduate laboratory experiments related to laser spectroscopy and atom trapping.

Acknowledgements

Throughout the past six years of my graduate studies at York University I have had the privilege of meeting many people without whom this work would not have been possible. I would first like to thank my supervisor, Dr. A. Kumarakrishnan, for having given me the opportunity to work in his lab. At a time when it seemed like pursuing a PhD in his group would be unlikely, he went above and beyond to ensure that I would have the opportunity to pursue my ostensibly far-fetched dream. His unwavering support and understanding throughout my degree made it possible to persevere when challenges were met. Kumar, even though these past years were not as stress-free as you had originally hoped, I was prepared to accept that pursuing a PhD would be no easy feat. Ultimately, this experience has shaped me into a stronger (and hopefully wiser) person, and it has allowed me to appreciate the world of physics at a much deeper level. For this, and for much more, I am very grateful. Thank you for all your time and effort you put into helping me complete one of the most influential and meaningful chapters of my life.

I would also like to thank members of my research group, who were outstanding sources of knowledge and friendship. In particular, Alex Pouliot, who made significant contributions within the group, especially by helping construct the TA systems, which were essential to the photon echo experiment. His help with technical issues and involvement in wide-ranging discussions were very stimulating and much appreciated. And after having spent so much time in the lab by myself, his joining the group created a much livelier lab atmosphere and a level of camaraderie I was missing. I would also like to thank Gehrig Carlse for his help in developing the TA system and his involvement in discussions relating to the echo experiment. I especially enjoyed our discussions ranging from deep physics questions to topics as simple as bread. I would like to thank Adam Carew for his help when I first joined Kumar's group, and for making my transition into a new lab that much easier. His involvement with the laser systems, troubleshooting the echo signal, and helpful discussions made a big impact on me and my work. Thank you to Andrew Vorozcovs for developing the auto-lock controllers and feedback algorithms for the laser systems, and for his help with the tweezers experiment. Especially, thank you for your willingness to work late hours in the lab with me on multiple occasions. I would also like to thank Thomas Vacheresse for his help on the photon echo experiment and the IF laser characterization, for all the baked goods, and for making lunch breaks more fun and enjoyable. I would like to thank Patrick Dowling for his development of the data acquisition

system for the echo experiment, and for helping to troubleshoot modifications of the program with me on multiple occasions. I would like to thank Nima Afkhami-Jeddi for his original work on the 780-nm lasers. I would also like to thank Boris Barron for his discussions involving ADEV theory and fitting algorithms. I would like to thank Carson Mok and Brynle Barrett for troubleshooting the atom trapping course experiments. In particular, I would like to thank Brynle for discussions associated to the review article and photon echo experiment. Thank you to Eric Rotberg for his help relating to the previous photon echo experiment. I would also like to thank Shira Jackson and Kevin Borsos for their help on the tweezers experiment, and Aidan Schiff for his involvement in the laser project.

I would also like to thank my supervisory committee members, Jim Martin, Cody Storry, and Louis Marmet, for their helpful discussions and feedback during yearly research evaluations. In particular, I would like to thank Louis for his deep involvement in our research group, his willingness to spend long hours with me to discuss and troubleshoot problems, and for his development of the theoretical model relating to the photon echo. I would also like to thank Cody and Eric's lab for their loans of equipment.

I would like to thank Scott Beattie for his loan of the wavemeter and for agreeing to be part of my Examination Committee.

I would like to thank Jerry Grech for his help in the machine shop with the laser

cavity construction. Additionally, I would like to thank Marlene Caplan, Cristalina Del Biondo, and Janaki DeCamillis for their help with administrative matters throughout the years.

I would like to thank Monika Aggarwal and Emily Yorke for their friendships and their support throughout my PhD years.

I would like to thank the Podmore family for welcoming me into their home and for their support as my degree came to an end. I especially appreciated their thoughtful Christmas gifts which kept me warm when I had to work long hours in the cold lab. In particular, I want to thank Alice for having made it her mission to keep my spirits high in the last year of my PhD, and whose friendship I treasure dearly.

To Hugh, words cannot express how much your presence in my life has meant to me all these years. Thank you for your unconditional love, patience, support, and understanding during this long process. I could not have managed to stay afloat without you.

To my family, and in particular my parents, thank you for all your love, help, and understanding, and for always being there for me during hard times. Without you, I could not have completed this journey.

Table of Contents

List of Tables

List of Figures

Abbreviations

Abbreviation	Long form
ECDL	External cavity diode laser
IF	Interference filter
FWHM	Full width at half-maximum
ADEV	Allan deviation
FBG	Fiber-Bragg grating
TA	Tapered amplifier
AOM	Acousto-optic modulator
PMT	Photo-multiplier tube
TTL	Transistor-transistor logic
RF	Radio frequency
EOM	Electro-optic modulator
FPI	Fabry-Perot interferometer
LO	Local oscillator
PSD	Position-sensitive detector
MOT	Magneto-optical trap
FID	Free-induction decay
LIDAR	Light detection and ranging
DIAL	Differential-absorption LIDAR
PLL	Phase-locked loop
VCO	Voltage-controlled oscillator
ODF	Optical-dipole force
FORT	Far-off resonance trap
cw	Continuous wave
ppb	Part-per-billion

1 Introduction

The goal of this dissertation is to develop a new class of pressure-sealed, auto-locked diode lasers for precision metrology, to utilize these lasers to develop optical dipole force traps (optical tweezers) to study the kinematics of dielectric particles, and to carry out a precise measurement of atomic lifetime in rubidium vapour. At the time when I began my PhD studies, my research group was faced with the challenge of developing stand-alone laser systems for precision metrology relevant to industrial applications for natural resource exploration. In particular, we wanted to develop a stable diode laser system that could be incorporated into a commercial gravimeter used in large area surveys for oil and natural gas prospecting. Another challenge was the need to develop laser sources at multiple wavelengths that could be controlled by an untrained operator. We also wanted to capitalize on the industrial project to develop high-power lasers suitable for atomic physics experiments. One of the limitations that we faced was that a single ageing titanium-sapphire (Ti:Sapph) laser was being shared for a number of cold-atom experiments [1]. These experiments were

also being operated near resonance due to the limited optical power that was available after passing through acousto-optic modulator (AOM) chains and optical fibers. As a result, precise measurements were impacted by near-resonant systematic effects such as the index of refraction.

To realize our goals, we developed low-cost ($5,000) external cavity diode lasers (ECDLs) that could be frequency stabilized to spectral features without the need for human intervention [1, 2, 3, 4]. The output of these auto-locking lasers (∼50 mW) was coupled into semi-conductor waveguide tapered amplifiers (TAs) to realize power outputs of ∼2 W, which enabled the simultaneous operation of independent experiments that could be operated off resonance due to the increased optical power. We also developed pulsing modules and high-speed data acquisition systems for applications such as optical tweezers, LIDAR transmission, atomic vapour-based magnetometry [5, 6, 7], and a variety of atom trapping experiments [1, 8]. We then carried out a precise measurement of the excited state lifetime in rubidium (Rb) vapour by exploiting the improvement in signal-to-noise that is a consequence of the high repetition rates (up to 1 MHz) that can be achieved in vapour-cell experiments.

1.1 Laser development

In the first part of the dissertation, we demonstrate the performance characteristics of a new class of vacuum-sealed, auto-locking diode laser systems and their

applications to precision metrology [2]. The laser is based on adaptations of a design [9, 10] that uses optical feedback from an interference filter (IF) and it includes a vacuum-sealed cavity, an interchangeable base-plate, and an auto-locking digital controller. A change of the base-plate allows operation at desired wavelengths in the visible and near infra-red spectral range, whereas the auto-locking ability allows the laser to be tuned and frequency stabilized with respect to atomic, molecular, and solid-state resonances without human intervention using a variety of control algorithms programmed into the same controller. We characterize the frequency stability of this laser system based on the Allan deviation (ADEV) [11] of the beat note and of the lock signal. We find that the ADEV floor of 2×10^{-12} and short-term linewidth of $\sim$200 kHz are strongly influenced by current noise and vacuum sealing. Reducing the current noise and cavity pressure decreases the ADEV floor and increases the averaging time at which the floor occurs, which is a signature of long-term stability. We also show that evacuating the cavity to $\sim$1 Torr reduces the range of the correction signal of the feedback loop by approximately one order of magnitude, thereby increasing the lock duration of the controller. The long-term stability allows the laser to be incorporated into a commercial gravimeter for accurate measurements of gravitational acceleration at the level of a few parts-per-billion (ppb), which are comparable to values obtained with an iodine-stabilized He-Ne laser. The auto-locking and pattern-matching features of the controller allow the laser to be tuned and sta-

bilized with respect to a temperature tunable transmission spectrum of a fiber-Bragg grating (FBG). This capability may be suitable for the development of a differential absorption LIDAR transmitter that can generate data at both on-line and off-line lock points using a single laser.

Therefore, the initial phase of my thesis consisted of evaluating the relative advantages of widely-used designs for ECDLs. Fig. 1.1 shows two commonly-used types of ECDLs. In the Littrow configuration described in reference [12] and references therein, the external cavity consists of the laser diode and the diffraction grating, while the internal cavity consists of the polished end faces of the laser diode, as shown in Fig. 1.1(a). The first-order diffracted beam from the external cavity is used to slave the internal cavity, and the zeroth-order reflection constitutes the laser output. In this design, the laser frequency can be scanned by applying a voltage to a pizeo-electric transducer attached to the grating. However, a drawback is that the grating has to be positioned at a carefully-chosen pivot point so that the alignment of the feedback is maintained during the scan. Furthermore, the direction of the output beam will change slightly when the laser frequency is scanned. The Littman-Metcalf design shown in Fig. 1.1(b) allows the output beam direction to remain fixed by using a carefully-positioned scanning mirror to send the optical feedback to the laser diode. Since the feedback light is diffracted twice from the grating, the laser linewidth is generally narrower than a Littrow laser, at the expense of greater external cavity

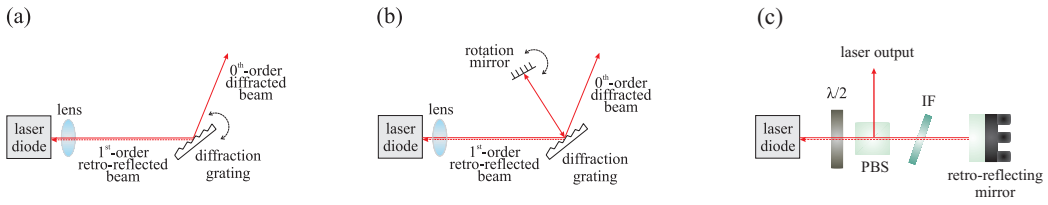

Figure 1.1: Representations of ECDL designs. (a) A Littrow cavity. (b) A Littman-Metcalf cavity. (c) An IF cavity. Here, $\lambda/2$ denotes a half wave-plate and PBS is a polarizing beam-splitting cube.

losses. In both designs, the spatial profile of the output beam is compromised by scattering from the grating. The beam distortion is particularly prominent in old-style diffraction gratings, and greatly reduced in holographic gratings. Based on these comparisons, we focused on adaptations of an interference filter (IF)-stabilized ECDL [9, 10], shown in Fig. 1.1(c). In this design, an IF with a narrow pass-band selects the light for optical feedback without significantly distorting the spatial profile. Further, a variable aperture in the laser cavity can act as a spatial filter and eliminate feedback from secondary modes. The laser frequency can be scanned without changing the direction of the output beam by changing the length of the external cavity with a piezo-mounted mirror. The optical feedback can be varied in a convenient manner by using a polarizing beam splitter (which also serves as the output coupler) and a half wave-plate.

This low-cost laser system was designed [13] using components from original equipment manufacturers coupled with specially-machined parts and powerful central pro-

cessors. My role was to assemble, align, and characterize the lasers, identify design modifications, and to carry out comparative studies to test the improvements. Rigorous testing and troubleshooting allowed the determination of the ideal amount of feedback light for different classes of non-AR coated laser diodes used in various applications. My experiments also compared the performance of two different kinds of optical feedback assemblies – one involving a corner-cube reflector and a second a "cat's eye" reflector, consisting of a mirror located at the focal length of a lens. However, the cat's eye reflector was preferred, since the corner-cube did not allow for smooth tuning of the laser cavity. Furthermore, two different gear assemblies were tested to ensure fine control of the angle of the IF from outside the laser cavity. I also experimented with different kinds of vacuum seals required to evacuate the cavity within minutes and maintain the seal for several months. Under these conditions, tests confirmed our hypothesis that pressure sealing extends the range of the feedback controller and improves the long-term frequency stability of the laser. Improvements associated with vibration isolation and reduction in current noise were also identified. The IF design relies on a laser cavity with an interchangeable optics kit consisting of a laser diode and optical feedback elements to operate in the desired wavelength range. This feature has enabled the development of these lasers at three distinct wavelengths: 633 nm for spectroscopy in iodine, and 780 nm and 795 nm for spectroscopy in rubidium vapour. The auto-lock digital controller allows the laser system to be locked or

scanned with respect to a spectral line or solid-state frequency markers. Therefore, our laser design realized performance characteristics that extended beyond those of commercial diode lasers that rely only on temperature and current control.

1.2 Optical tweezers

The IF laser systems were also used in conjunction with TAs to develop an optical tweezers experiment [14, 15, 16, 17, 18, 19, 20]. Here, dielectric particles were trapped at the focus of a laser beam using the optical dipole force. In my initial experiments, I trapped polystyrene beads in saline solution. Later on, I developed a free-space version of this experiment by ablating the tip of a Sharpie marker at the focus of the laser beam, so that carbon-black particles of the Sharpie ink could be introduced without any drift velocity and thus become easily trapped. Although the trapped particles are buffeted by air at the rate of $\sim 10^{16}$/s, the damping time of the particles is ~ 1 μs, and as a result, the particles undergo Brownian motion on longer time scales. The mean-squared displacement of these particles was measured using a CCD camera operating at a rate of $\sim$100 frames per second (fps). The spring constant of the trap is proportional to the laser intensity, resulting in an inverse relation between the mean-squared displacement and the intensity. Since the experiment is carried out at room temperature, the equipartition theorem can also be used to measure the spring constant and its linear dependence on laser intensity. By tracking the particle on a fast

time scale of $\sim$50 μs in the saline solution using a position-sensitive detector, it was possible to construct the position auto-correlation function of the trapped particle. The independent measurements of the spring constant and the correlation times could be used to infer the damping rate of the Brownian motion. Over the last few years, this experiment has been used to study a variety of particles trapped in free space on even faster time scales using a sensitive high-speed CMOS camera that is capable of operating at over 100,000 fps. In these experiments, we are attempting to measure the damping rate both from the motion of the falling particle and its trajectory when it is restored to the trap center by the laser force. The combination of the correlation time and the spring constant also provides an independent measure of the damping rate. We are currently studying the feasibility of rapid in situ identification of trapped particles that may be relevant to characterizing the constituents of flue gases including biological specimens [14].

I have also incorporated the optical tweezers experiments into PHYS 4061, which is an upper-level laboratory course on laser spectroscopy integrated with a graduate course [15]. The auto-locked laser systems developed as part of this thesis were also envisioned to support a number of laser spectroscopy experiments in PHYS 4061/5061 and a follow-up semester-length course on atom trapping (PHYS 4062/5062). These courses constitute a powerful approach for teaching experimental physics in a manner that is both contemporary and capable of providing the background and skills relevant

to a variety of research areas. Along with other group members, I have developed and edited the laboratory manual for these courses and obtained representative data for a tutorial article that discusses the motivation, course format, overview of key experiments, pedagogical aspects and outcomes, budgetary requirements, challenges related to long-term maintenance, and the overall impact on student training.

1.3 Atomic lifetime measurements

The final phase of my thesis involves using the aforementioned pulsed laser systems to set up a coherent-transient experiment based on the technique of photon echoes to measure the $5^2P_{3/2}$ excited-state lifetime in rubidium vapour [21]. This experiment established the suitability of the laser systems for precision measurements in atomic physics, apart from being well-matched with the timeline for the completion of the thesis. The measurement explores the sensitivity of the photon echo technique for achieving precise measurements of atomic lifetimes. Using short-pulse excitation of atomic rubidium vapour, we report a measurement of the $5^2P_{3/2}$ lifetime of (26.10 $\pm$ 0.03) ns with a statistical uncertainty of 0.11% in 4 hours of data acquisition over several weeks that agrees with the most precise measurement in this atomic system. We show that the best statistical uncertainty achieved with the current configuration is 0.013%, which has been exceeded by only one other lifetime measurement. The experiment primarily relies on heterodyne detection for measuring the signal-to-noise

ratio of the coherent release of energy along the direction of excitation. The energy release exhibits an exponential decay as a function of pulse separation T. Furthermore, the experiment can be carried out with large repetition rates that are feasible in a gently-heated vapour cell. We have developed an understanding of the technical limitations responsible for lifetime measurement variations on the basis of a simple model, which also enables us to propose a feedback scheme to limit these effects. Studies of the fractional uncertainty of the lifetime suggest that the statistical precision of this technique can be extended from the current level of 0.3% in 66 seconds of data acquisition for a single exponential decay to the level of 0.03% in 10 minutes of data acquisition if the technical limitations are addressed. Under these conditions, a rigorous investigation of systematic effects could potentially allow the echo technique to achieve the most accurate measurement of atomic lifetimes. My role in the lifetime measurement included the deployment of laser systems, implementation of a high-speed data acquisition system, set-up of an RF network and optical alignment to produce short excitation pulses, as well as troubleshooting and data analysis.

We now provide an overview of experimental techniques for realizing atomic lifetime measurements. We also introduce the principles and the relative advantages of the photon echo technique that has been developed in this work. The established techniques for precise lifetime measurements involve frequency-domain experiments, in which a laser is scanned across an atomic resonance to measure the transition

linewidth, or time-domain techniques in which the decay of the excited-state population through spontaneous emission is measured as a function of time from an atomic sample following laser excitation, as shown in Fig. 1.2. In these experiments, the linewidth of the absorption spectrum shown in Fig. 1.2(a) is $\Gamma_N = \Gamma/2\pi$, where Γ is the radiative rate of the excited state. The radiative lifetime shown in Fig. 1.2(b) is given by $\tau_1 = 1/\Gamma$. Some prominent experiments include:

(1) A linewidth measurement using laser-cooled atoms and absorption spectroscopy [22]. The most prominent systematic effect in absorption measurements is the laser linewidth, making it necessary to develop lasers with ultra-narrow linewidths (on the order of a few kilohertz). Since the laser linewidth is a Lorentzian, the measured linewidth is the sum of the natural linewidth and the laser linewidth. Other corrections to the measured linewidth include the effect of power broadening [23].

(2) Measurements of radiative lifetime in fast atomic beams [24]. Here, a supersonic atomic beam is laser excited, and a histogram of atomic decay events is mapped out as a function of time through photon counting. Alternatively, the distance over which excited atoms fluoresce can be converted to time from the knowledge of the speed distribution of the atomic beam. These experiments require a sizeable apparatus to generate the atomic beam, as well as the development of a photon counting apparatus and intricate imaging systems. Such photon-counting measurements have also been carried out in laser-cooled atomic samples [25]. For these measurements,

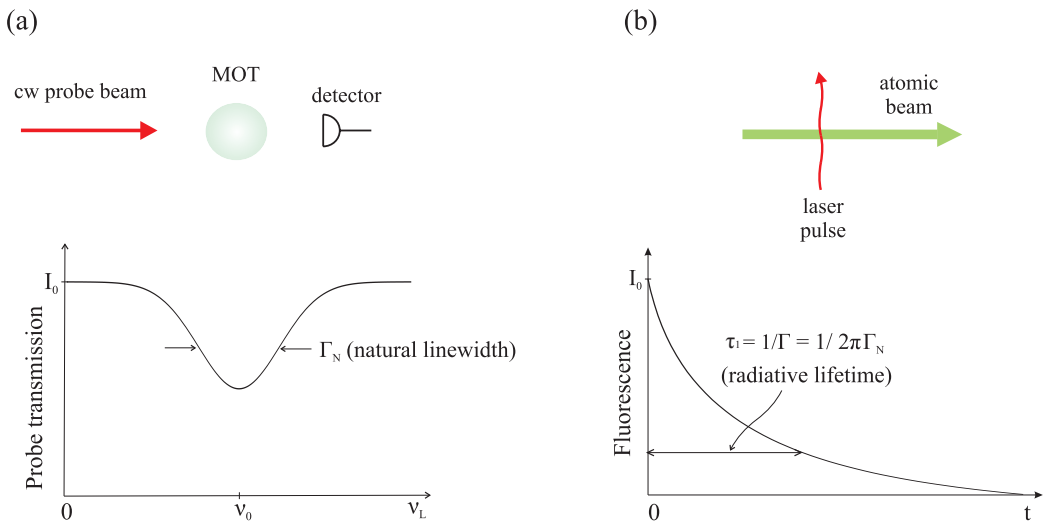

Figure 1.2: Principles of established techniques for linewidth and lifetime measurements. (a) Absorption detection. Here, MOT refers to a magneto-optical trap. (b) Fluorescence detection.

additional requirements include the apparatus for atom trapping, the need to state select cold atoms, and operate at low densities to avoid the systematic effect of radiation trapping, which increases the lifetime value.

The photon echo technique which has been developed in this work constitutes a general method for cancelling the effect of inhomogeneous (Doppler) broadening in atomic gases. This technique was first used in nuclear magnetic resonance [29], and its optical analog was later demonstrated in a ruby crystal [27]. We have adopted this technique since it does not require ultra-narrow laser linewidths, and it does not impose specialized requirements on sample preparation or signal detection. Here, a

two-level atomic sample consisting of a ground state and an excited state is excited by two travelling-wave pulses applied at $t = 0$ and $t = T$. The first pulse excites a coherent superposition of ground and excited states, which is equivalent to a radiating dipole moment in a classical picture. The radiation, known as free-induction decay (FID), decays on a time scale $\tau_D = \lambda/u$, where τ_D is the dephasing time, λ is the wavelength of light, and u is the most probable speed of the Doppler-broadened velocity distribution. The decay of the signal can be described as being due to a dephasing that occurs when individual atoms travel a distance that is larger than the wavelength of light. As long as the excited state has not decayed, the second excitation pulse can cancel the effect of Doppler broadening and rephase the atomic radiators on a time scale τ_D, so that the rephasing is complete at $t = 2T$. As a result, the sample emits a coherent burst of radiation along the direction of the excitation pulses, known as a photon echo. Our measurement technique consists of measuring the exponential decay of the radiated energy as a function of T, since the time constant of the decay is the radiative lifetime τ_1. Fig. 1.3, adapted from references [28, 30], provides a simple classical description of the echo technique. At $t = 0$, a starter fires a gun and runners representing individual atoms start off in the same direction on a racetrack. Doppler dephasing is represented by the distribution in the positions of the runners who travel with different (fixed) speeds. At $t = T$, the starter fires the gun a second time, causing the runners to stop and run back with the same speeds. Since

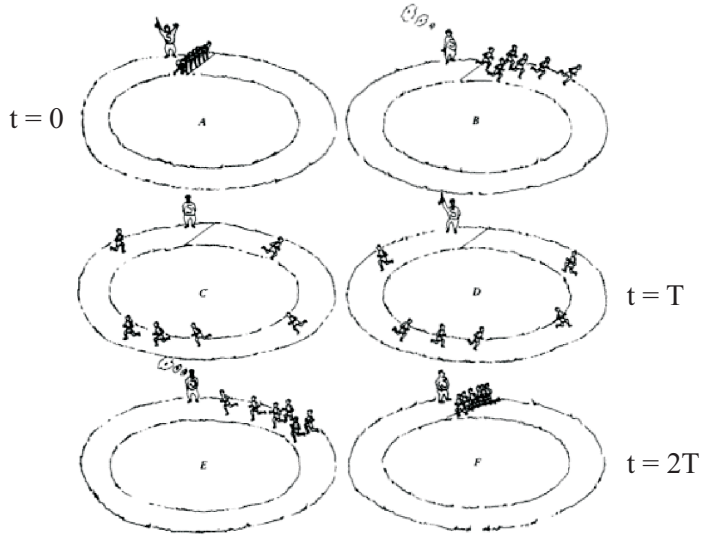

Figure 1.3: Classical analogy for the photon echo technique showing runners on a racetrack, adapted from references [30, 28].

the slower runners are now closer to the starting point, the faster runners catch up with them at a time $t = 2T$. The simultaneous arrival of the runners at the starting point is analogous to the rephasing of the atomic sample.

A more sophisticated semi-classical description of the photon echo technique was the so-called "billiard ball model" introduced in reference [31]. A representation of this single-atom description is shown in Fig. 1.4. Here, at $t = 0$, the first excitation pulse creates a superposition state consisting of a ground-state wavepacket shown in red, and an excited-state wavepacket shown in blue. In this picture, the photon momentum $\hbar k$ associated with the laser pulse is entirely absorbed by the excited-state wavepacket, which acquires a recoil velocity $v_{rec} = \hbar k/m$, and separates from

the ground-state wavepacket. Here, $\hbar = h/2\pi$, $k = 2\pi/\lambda$ is the wave vector, and m is the atomic mass. The figure shows the central mass separation between the wavepackets as a function of time. Here, the FID is associated with the overlap of the wavepackets, and terminates when the wavepackets separate. The dispersion of the wavepackets can also be considered, but this effect does not affect the conclusions. When the second pulse is applied at $t = T$, the ground-state wavepacket absorbs the photon momentum and becomes transformed into an excited-state wavepacket. The excited-state wavepacket becomes transformed into a ground-state wavepacket through the stimulated emission of a photon, thereby becoming stationary. The two wavepackets interfere in the vicinity $t = 2T$, resulting in a photon echo. In this description, the size of the wavepacket x_w is the thermal de Broglie wavelength λ_{dB}, and therefore the dephasing and rephasing times, which are given by $\tau_D = \lambda_{dB}/v_{rec}$, are the same as in the classical description. This description of the echo technique has been very influential since it can be considered as an atom interferometer. The model finds widespread applicability since the signal from an ensemble of atoms can be obtained by averaging over the velocity distribution.

We now review the organization of the rest of this dissertation. In Chapter 2, we present a survey of literature that discusses the development of ECDLs, discuss limitations that have been overcome by our IF design, and show the versatility resulting from our adaptations. We also outline the concept of the Allan deviation (ADEV),

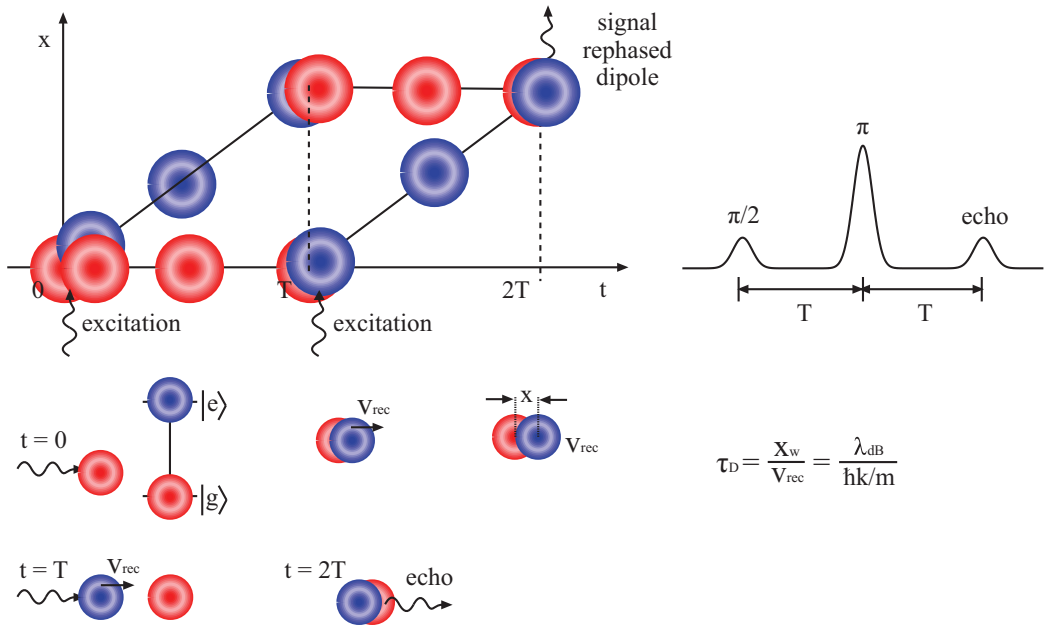

Figure 1.4: Wavepacket description of the photon echo experiment showing the center of mass separation between ground-state and excited-state wavepackets as a function of time. The experimental pulse sequence is also shown.

and discuss how it is implemented in the context of our results. The details of the laser head and auto-lock controller are presented in Chapter 3. This is followed by a description of the experimental set-up required to characterize the IF lasers that rely on both iodine and Rb spectroscopy. The results of laser characterization and applications to metrology are presented in Chapter 4. We transition to the theoretical description of the photon echo technique in Chapter 5, and compare different techniques for measuring atomic lifetimes. In Chapter 6, we discuss the experimental details associated with the echo measurement. The results and technical limitations of the lifetime measurement are presented in Chapter 7. We summarize the results of this work and prospects for improvements in Chapter 8. The optical tweezers experiment and my contributions to the experiments in PHYS 4061 and PHYS 4062 are summarized in Appendix A. Appendix B lists the papers and conference abstracts related to this dissertation.

2 Laser characterization: background

2.1 Comparison of laser designs

In this chapter, we begin with an overview of the development of ECDLs and outline the versatility that is achieved through our IF design. There has been widespread interest in developing narrow-linewidth laser sources with excellent long-term stability for applications in precision spectroscopy [32], atomic frequency standards [33], atom trapping [34] and atom interferometry [35], and precision metrology related to industrial and space applications [36, 37, 38]. Typically, these laser sources are realized by frequency stabilizing laser diodes, distributed feedback (DFB), and distributed Bragg reflector (DBR) lasers to external cavities of varying designs such as compact Littrow cavities [39, 32], Littman-Metcalf resonators [40, 41], Fabry-Perot etalons [42, 43], the internal cavity of the laser diode [44], monolithic resonators [45], and optical fibers [46]. Since the relative frequency stability of these laser systems can surpass commonly-available radio frequency standards such as rubidium vapour cell clocks [47], there is also considerable interest in distributing stable optical frequency

standards across research laboratories [48].

We show that adaptations of a widely used diode-laser design can provide excellent long-term frequency stability for applications such as gravimetry and LIDAR-based remote sensing. In particular, we have adapted an ECDL design based on IF feedback, developed a digital auto-locking controller that can stabilize the laser frequency without human intervention, and studied the improvements in stability that can be realized by reducing current noise and by vacuum-sealing the cavity. Well known designs have used gratings, etalons, and beam splitters to provide optical feedback to the laser diode [12, 9, 10, 49, 50, 51, 52, 53]. Representative studies focused on improving the short-term stability are described in references [51, 54, 55]. In the widely used Littrow design, scanning the laser frequency with a piezo-mounted grating changes the optical feedback as well as the length of the external cavity. This disadvantage can be overcome by positioning the grating at a carefully-chosen pivot point [51], whereas the overall stability of the Littrow cavity can be improved using a monolithic design, hermetic sealing, back-filling with inert gases, and improving vibration isolation [53]. The work in reference [51] showed the mode hop-free tuning range of a modified Littrow design in the 780-nm band that had reduced sensitivity to acoustic noise. The mode hop-free tuning range of these systems can be significantly extended by synchronous scanning of the current and the grating using a feed-forward circuit. In comparison, IF-stabilized diode lasers have the advantage that the filter used for

wavelength selection is separate from the piezo-mounted mirror which changes the length of the laser cavity. This design also reduces distortions of the spatial beam profile. These two effects make it potentially easier to achieve mode hop-free tuning over the free spectral range of the cavity.

Previous work [9, 10] showed that the IF design exhibited a narrow linewidth (tens of kHz) and a tuning range of several nanometers achieved by changing the incidence angle of the filter. In our work, we demonstrate the operation of IF lasers at both 633 nm and 780 nm using the same vacuum-compatible laser head design and an auto-lock controller. The desired operating wavelength is achieved by changing the optical elements and laser diode. In ECDL designs that have been commercialized, the stability of the laser is achieved by temperature and current control of the laser diode, and temperature stabilization of the enclosure containing the laser head. However, long-term ambient temperature and pressure drifts necessitate a correction signal with a large range, thus limiting the time over which the laser frequency can remain actively stabilized (locked). Our design has addressed this limitation by allowing the laser cavity to be pumped out [1, 2, 3, 4]. To bring the laser cavity back into alignment after pump-out, we use a vacuum-compatible feed-through to realign the angle of the IF from outside the cavity to compensate for the change in the refractive index.

Our results indicate that the suppression of pressure-induced frequency drifts re-

sults in a nearly ten-fold reduction of the correction signal amplitude, thereby increasing the lock duration and improving long-term stability. We show that both a reduction in the current noise and a reduction in the pressure inside the laser cavity result in a reduced overall ADEV and an increase in the averaging time at which the floor of the ADEV occurs, thereby indicating improved long-term stability. The auto-locking feature facilitates locking and tuning with respect to atomic, molecular, and solid-state references. The advantages of auto-locking coupled with the long-term stability allow the laser system to be integrated with an industrial gravimeter to achieve accurate measurements of gravitational acceleration at the level of a few ppb. Furthermore, we show that the laser can be frequency stabilized with respect to a temperature tunable transmission peak from a fiber-Bragg grating (FBG). Since a pattern-matching algorithm can be used for auto-locking, this demonstration allows the laser system to serve as the basis for a differential absorption (DIAL)-type LIDAR transmitter that can be operated at both on-line and off-line lock points.

We conclude this section with a comparison of lasers that have achieved excellent short-term stability, as shown in Table 2.1. It is notable that our home-built laser system stands out because it has achieved good long-term stability, which is crucial for all the applications described in this work, such as gravity measurements, diode laser-based LIDAR transmission, and atomic lifetime measurements.

Table 2.1: Comparison of the ADEV floor and the averaging time of ECDLs.

Group	**ADEV**	**Averaging time (τ)**
Kunze [54]	10^{-10}	10 μs $< \tau <$ 20 ms
Fukuda [55]	6.2×10^{-11}	5 s
Turner [56]	5×10^{-12}	1 s
Our group [2]	2×10^{-12}	300 s

2.2 Discussion of the ADEV and its implementation

One of our goals is to develop reliable methods to characterize the frequency and amplitude stability of the IF-based ECDLs. In a typical laser characterization experiment, the laser frequency is sampled at a suitable rate, defined by the speed of the data acquisition system. The inverse of the sampling rate defines the time τ between successive data points. A universal measure of the laser frequency stability is to report the standard deviation of the data points. This procedure will be particularly successful if the laser frequency excursions are dependent only on white frequency noise. In this case, the standard deviation of the mean will scale as $\tau_m^{-1/2}$, where τ_m is the measurement time. However, a variety of noise sources can couple into the experiment. Such common noise sources include white (flicker) phase noise, which scales as τ^{-1}, flicker frequency noise, which scales as τ^0, and random-walk frequency

noise, which scales as $\tau^{1/2}$. Therefore, in the general case, the standard deviation is not regarded as a good representation, since it does not converge for most noise sources. As a result, the ADEV is widely used for laser stability analysis, and this quantity is the square-root of the Allan variance. We note that even the ADEV does not converge for all noise types, and thus more specialized forms of the ADEV may need to be introduced, as discussed in references [57, 11] and references therein.

A common application for which the ADEV is used is the characterization of the frequency stability of oscillators and clocks. Here, the Allan variance is defined as one half of the time average of the squares of the differences between successive readings of the frequency deviation acquired over the sampling period τ_0, and it therefore depends on the measurement time $\tau = n\tau_0$, where n is the number of acquisitions. A low Allan variance indicates that a particular clock or oscillator has a good stability. It is typically graphed in log-log format, and fits to the linear portions of the graph can provide insight into the various noise sources present in the system.

In a clock application, the measurement consists of a sequence of clock phases (voltages), from which the clock frequency needs to be extracted. To further explain this concept, we consider the measurement sequence shown in Fig. 2.1(a). In order to quantify the phase variations $x(t)$ (expressed as a time delay) over a chosen time interval, τ, a frequency-departure graph can be constructed, as shown in Fig. 2.1(b), where $y_i(t)$ represents a fractional frequency departure given by:

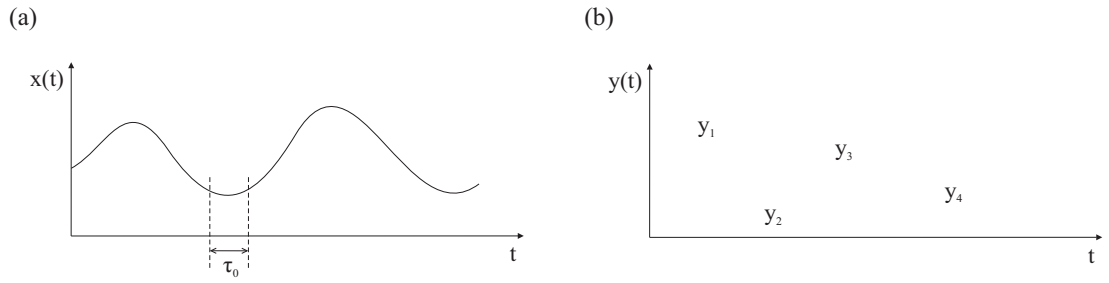

Figure 2.1: (a) A sequence of clock phase measurements as a function of time. (b) Frequency-departure graph constructed from part (a).

$$y_i = \frac{x_{i+1} - x_i}{\tau_0}. \tag{2.1}$$

To determine the instability in the $y_i(t)$ values, the ADEV can be computed as:

$$\sigma_y(\tau_0) = \sqrt{\sum_{i=1}^{N-1} \frac{1}{2(N-1)} (y_{i+1} - y_i)^2}, \tag{2.2}$$

which represents a measure of the change in frequency over the sampling time τ_0.

A similar treatment can be developed for describing frequency variations of a test oscillator $\nu_1(t)$ with respect to a reference oscillator with frequency ν_0. Here, the y_i values, which represent fractional frequencies, are defined as

$$y_i(\tau) = \frac{\nu_1(t_0 + i\tau_0) - \nu_0}{\nu_0}, \tag{2.3}$$

where t_0 represents the time occurrence of the first point and τ_0 is the sampling time. Typical comparison protocols require the reference oscillator to be about 10^4

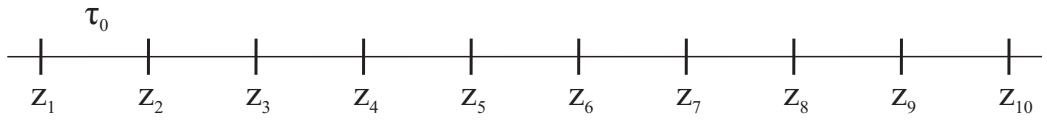

Figure 2.2: A sequence of successive measurements separated by time τ_0.

times more stable than the test oscillator. The ADEV can once again be defined as in Eq. (2.2). In this thesis, all ADEV measurements involving beat note analyses involve computations of the ADEV from a list of measured frequencies. Calculations of the ADEV have also been used in other sections of the thesis. Examples include lock stability analysis (where the data set consists of a sequence of voltages that represent laser frequency excursions from the lock point), laser and RF intensity stability analysis (where the measurements are again a sequence of voltages representing RF power), and lifetime stability analysis (where the data set is a sequence of successive lifetime measurements). In all these cases, we compute the overlapping ADEV, as described by the following protocol.

To illustrate how the implementation works, we consider a set of data points z_i spaced by τ_0, as shown in Fig 2.2. The program computes the ADEV as a function of the measurement time τ. As an example, for $\tau = 2\tau_0$, we define a new list of non-overlapping averages, consisting of pairs of sequential points of the form $z'(2\tau_0) = \frac{z_1+z_2}{2}, \frac{z_3+z_4}{2}$, etc. For $\tau = 3\tau_0$, such a list would consist of averages of three sequential points. Assume that this list is specified as $z(2\tau_0) = z'_1, z'_2$, etc. From the new list of non-overlapping averages, the ADEV, $\sigma_{z'}(2)$, is determined as:

$$\sigma_{z'}(2\tau_0) = \sqrt{\frac{1}{2(4)}\left[(z'_2 - z'_1)^2 + (z'_3 - z'_2)^2 + (z'_4 - z'_3)^2 + (z'_5 - z'_4)^2\right]}. \tag{2.4}$$

The above expression takes the squares of differences between successive sets of points in the z' list. In contrast, the so-called overlapping ADEV $\sigma^O_{z'}(2)$ is also calculated based on Eq. (2.3) using a list of overlapping averages of the form $z''(2\tau_0)$ $= z''_1, z''_2, \ldots = \frac{z_2+z_3}{2}, \frac{z_4+z_5}{2}, \ldots$. The overlapping ADEV improves the statistical uncertainty, since it makes better use of the data to obtain a greater point density, and it is given by the following formula:

$$\sigma^O_{z'}(2) = \sqrt{\frac{1}{2(8)}\left[(z'_2 - z'_1)^2 + (z'_3 - z'_2)^2 + \cdots + (z''_2 - z''_1)^2 + (z''_3 - z''_2)^2 + \ldots\right]}. \tag{2.5}$$

Finally, the computed ADEVs are then expressed as fractional quantities, depending on scale factors and calibrations. This protocol has been applied in all the ADEV calculations presented in this thesis.

3 Laser characterization: experimental details

3.1 Description of laser cavity

In this chapter, we first discuss the operational principles of the laser head and details of the auto-lock controller. This is followed by a description of the experimental set-up required to characterize the lasers. Fig. 3.1(a) shows a schematic of the laser head. The collimated output of the laser diode passes through a variable beam splitter, which transmits a small fraction of the laser power through the IF with a 0.3-nm FWHM passband. The frequency band selected by the IF is optically fed back into the diode by a 'cat's eye' retroreflector consisting of a piezo-mounted mirror placed at the focal length of a lens [9, 10]. The external cavity length, measured from the laser diode to the retro-reflecting mirror, is 10 cm. The output of the laser cavity (50-100 mW) is the vertically-polarized reflection from the variable beam splitter. All the optical elements of the laser cavity are mounted on a compact, temperature-stabilized aluminum base-plate (controlled to ± 1 mK). The base-plate and the diode can be easily interchanged to allow the laser to operate within a selected wavelength

range. A variable aperture mounted near the laser diode is used to reject unwanted spatial modes and filter the feedback light [2, 3, 4]. The angle of the IF can be adjusted from outside the laser cavity using a vacuum feed-through connected to an assembly with a gear ratio of either 18:1 (cavity type A) or 100:1 (cavity type B). Unlike cavity type A, cavity type B is also designed with screw holes that have escape channels for trapped gases. An electrical vacuum feed-through also enables the laser set-points (current, temperature, piezo voltage) to be controlled from outside the laser cavity, and a built-in pressure sensor allows the pressure inside the cavity to be monitored. The base-plate is covered with a stainless-steel or aluminum enclosure with an O-ring for vacuum sealing. The enclosure also has a welded pump-out port for evacuating the cavity and an O-ring-sealed view-port for the laser output, as shown in Fig. 3.1(b).

3.2 Description of the auto-lock controller

The auto-lock controller consists of a low-cost, single-board computer (SBC) with analog-to-digital (A/D) and digital-to-analog (D/A) capability that acts as a specialized lock-in amplifier. It is also responsible for unattended start-up of the laser and laser mode monitoring functions. In order to tune the laser to the desired spectral location (frequency) from a cold start condition, the controller performs pattern matching between Doppler-free peaks obtained by scanning the laser frequency and reference peaks stored in the processor's memory. The incoming spectral signals are

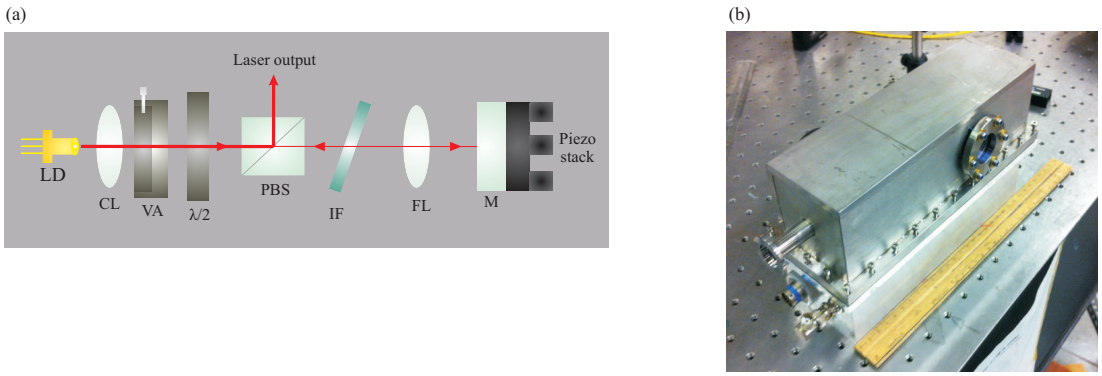

Figure 3.1: (a) Schematic of IF laser design. The optical elements are: LD - laser diode, CL - collimating lens, VA - variable aperture, $\lambda/2$ - half wave-plate, PBS - polarizing beam splitter, IF - interference filter, FL - focusing lens, M - mirror. (b) Photograph showing pump-out port, O-ring seals of window and enclosure, and electrical feed-throughs in the base.

compared with the reference waveforms using a sliding correlation algorithm, which determines the control voltages required for adjusting the laser frequency to the desired lock point. The system has a scan amplitude of less than 1 MHz when locked and it can re-lock for frequency drifts up to 10 GHz without human intervention. The controller is also equipped with an auto-calibration module, which allows a variety of laser operating parameter combinations to be systematically explored in order to determine optimal settings required to avoid operating the laser diode in a multi-mode condition or near a mode hop. The controller builds and stores a library of settings for a particular laser diode and periodically recalibrates the determined parameters

to adjust for ageing of the laser diode to ensure stable operation.

The SBC is equipped with two analog-to-digital conversion (ADC) input pipelines, a high-speed input stage, and a background-monitoring stage. The high-speed input stage samples one photodiode signal and a copy of the piezo signal (for definitive referencing and synchronization) simultaneously at a 100-kHz sampling rate with 16-bit resolution. The background monitoring stage operates at 120 Hz sampling rate and is used for recording operating conditions of the laser such as current, temperature, and pressure. The SBC is also equipped with two digital-to-analog converter (DAC) output stages. The first stage operates at 48 kHz and 16-bit resolution and is used to synthesize triangular and sinusoidal waveforms for lookup scans and lock-in operation. The second DAC stage is used to generate slow-varying control signals and set-points for the laser controller. The output for the piezo is fed into a high-voltage amplifier to enable a large ($\sim$10 GHz) scan range.

An analog preamplifier brings the input analog signals within the analog input range of the ADC. After the signals are preamplified and digitized, the on-board software performs the appropriate processing functions (laser start-up, linear scan, or continuous lock-in operation). The output parameters are fed out to the DACs and the corrections are immediately applied to the laser current and piezo. The SBC is equipped with 128 MB of RAM and runs at a 500-MHz clock rate. These parameters allow for complex digital signal processing operations to be performed

quickly, such as sliding correlation on large (N = 1024) samples and long-term finite impulse response filtering. The SBC is also equipped with on-board non-volatile (Flash) storage that is used to log operating data for subsequent review. The SBC controller can be operated locally, via a 4.3″ touch screen mounted on the case or remotely via a TCP/IP connection using Ethernet through a LabVIEW interface.

3.3 Set-up for laser characterization

To study atomic and molecular spectra, the laser systems were also integrated with a compact set-up for saturated absorption spectroscopy [58]. Our laser characterization set-up shown in Fig. 3.2 also involves a vibration isolation platform with a resonant frequency of ∼1 Hz. Two identical diode-laser systems are mounted on this platform and locked to neighbouring resonances in iodine or rubidium vapour to produce beat notes ranging from 10 to 90 MHz. The short-term laser linewidth is inferred from a Fourier transform of the beat note acquired in 50 ms using a spectrum analyser with a resolution of 1 Hz and scan range of 9 kHz – 26.5 GHz. The long-term frequency stability is inferred from the ADEV of both the beat note and the lock signal.

The lock signal data is obtained by stabilizing the laser frequency with respect to a single hyperfine resonance in a compact saturated absorption spectroscopy set-up in which the pump beam is retro-reflected through the vapour cell to generate a

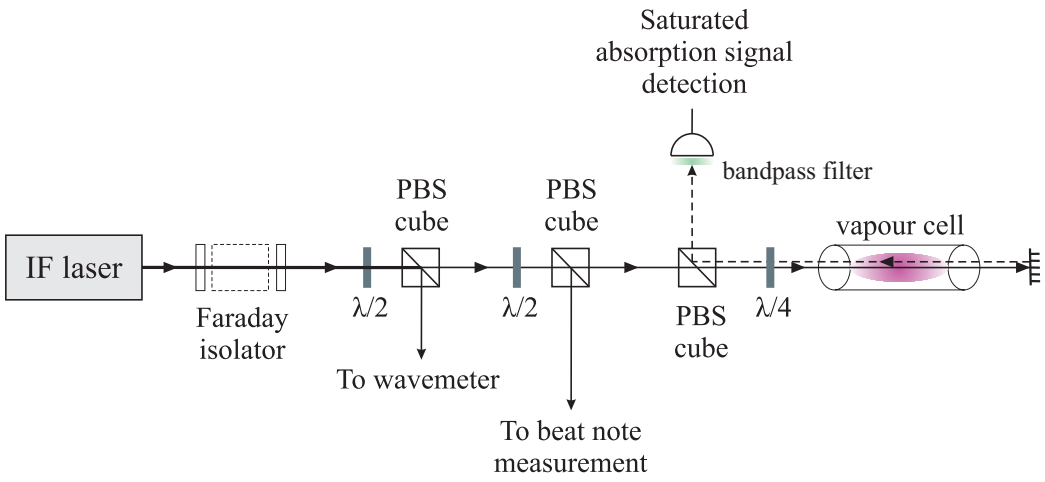

Figure 3.2: Set-up for laser diagnostics, which was mounted on a vibration isolation platform. The saturation absorption spectrometer involves a compact dual-pass configuration.

weaker counter-propagating probe beam [58]. The beat note is recorded on a Si-PIN photodiode with a rise time of 1 ns, whereas the lock signal data is recorded with a 10-ns rise time photodiode. A wavemeter with a resolution of 50 MHz is used to coarse tune the laser frequency. The calibration of the frequency offsets and drifts is obtained from measured hyperfine splittings such as those in reference [59] and from wavemeter readings. For lock signal analysis, a data card with a sampling rate of 48,000 samples/s is used, whereas for the beat note analysis we use a data card with a sampling rate of 1 GS/s. A separate `C++` program is used to determine the frequency of the beat note based on counting the zero crossings.

For the iodine data, the frequency stabilization is accomplished using the third

derivative of the saturated absorption signal since the resonance widths are relatively narrow ($\sim$1 MHz) and superposed on a large Doppler background. In rubidium, stabilizing the laser frequency using pattern matching was successful since the shapes of the resonances are reliably known without repeating molecular series. Alternatively, the laser frequency can be stabilized using first derivative feedback. The aforementioned technique is also used to lock the laser frequency to a FBG transmission peak. The time constant of the feedback loop is $\sim$1 second for the iodine-stabilized laser systems and $\sim$50 ms for the rubidium and FBG systems. Both the error signal that is fed back to the laser cavity and the correction signal that represents the drift of the accumulated error signal over the lock duration are monitored by the controller.

For the data associated with the vacuum-sealed lasers, the laser cavity is evacuated using a roughing pump and a 2-m long bellows hose. Prior to recording lock data, the vacuum enclosure of the laser is valved off and the bellows disconnected. The pressure of the sealed laser cavity is monitored using a Pirani gauge. At each pressure setting, the optical feedback is adjusted from outside the cavity by tuning the IF angle.

4 Laser characterization: results and discussion

In this chapter, we discuss the results of IF laser characterization involving iodine and Rb spectroscopy that include the improved range of the auto-lock controller, the effect of current noise, the improvements due to vacuum sealing, and the effects of these parameters on the laser linewidth. We then present results relevant to precision metrology that include accurate measurements of gravitational acceleration and applications for LIDAR transmission. These results are also presented in reference [2].

4.1 IF laser characterization

Fig. 4.1(a) shows the Doppler-broadened resonance in a 10-cm long iodine vapour cell. The observed hyperfine resonances can be clearly discriminated using a first derivative error signal, as shown in Fig. 4.1(b). Since the resonances are relatively narrow, the tightest locks were achieved using third derivative spectroscopy, as shown in Fig. 4.1(c). Another advantage of this method is that it removes the Doppler

background. Fig. 4.1(d) shows representative hyperfine spectra in ^{85}Rb which are relatively broad ($\sim$10 MHz) due to power broadening.

Fig. 4.2(a) shows the lock signal and correction signal for a 780-nm laser system (design type A) that is frequency stabilized at atmospheric pressure using first derivative spectroscopy and a current controller with a characteristic power spectral density of 200 nA/$\sqrt{Hz}$ (manufacturer specifications). The figure shows that the lock signal is centered about the lock point with excursions of $\sim$1 MHz. In contrast, the correction signal shows a drift of several tens of megahertz. Fig. 4.2(b) shows the same data with the laser cavity evacuated to a pressure of 1.6 Torr. We note that the lock signal excursions increase by a factor of $\sim$2. This effect was attributed to the slow escape of trapped gases inside the laser cavity, and was reduced in the design of laser cavity type B. Most importantly, the overall range of the correction signal has been reduced by nearly a factor of 7. Similar reduced ranges for the correction signal were observed using third derivative spectroscopy in iodine and pattern matching algorithms in Rb [3]. Additionally, the correction signals at atmospheric pressure are strongly correlated with pressure variations, whereas the corresponding correction signals at 1.6 Torr are uncorrelated. The features of the correction signals for the pressure-sealed lasers indicate an obvious advantage, namely an extended lock duration and long-term stability. This aspect is unambiguously shown in studies of the ADEV that follow. However, since the ADEV is significantly affected by both laser current noise

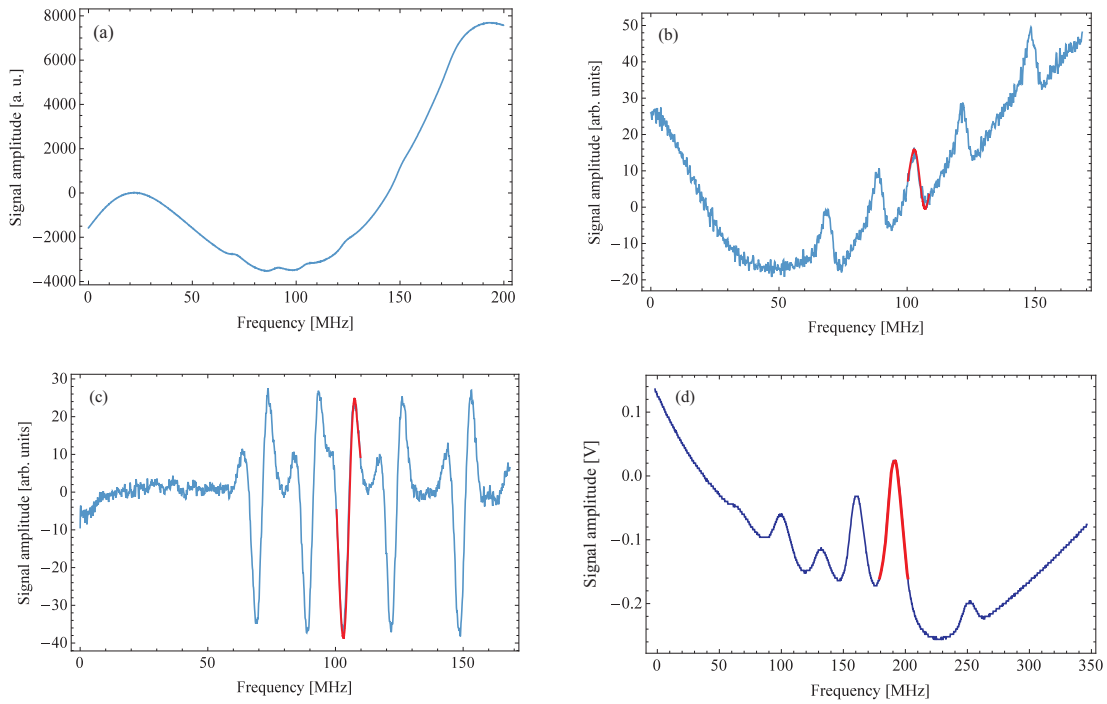

Figure 4.1: Representative saturated absorption spectra showing typical lock points highlighted in red. (a) P(33)6-3 Doppler-broadened resonance in iodine vapour. (b) First derivative of the P(33)6-3 Doppler-broadened resonance. The FWHM inferred from the fit is (5.1 ± 0.1) MHz. (c) Third derivative of the P(33)6-3 spectrum. The FWHM inferred from the fit is (2.9 ± 0.1) MHz. (d) Hyperfine spectrum of the $F = 3 \rightarrow F' = 2, 3, 4$ transition in ^{85}Rb vapour. The FWHM inferred from the fit to the $F = 3 \rightarrow F' = 3, 4$ cross-over peak is (12.9 ± 0.2) MHz.

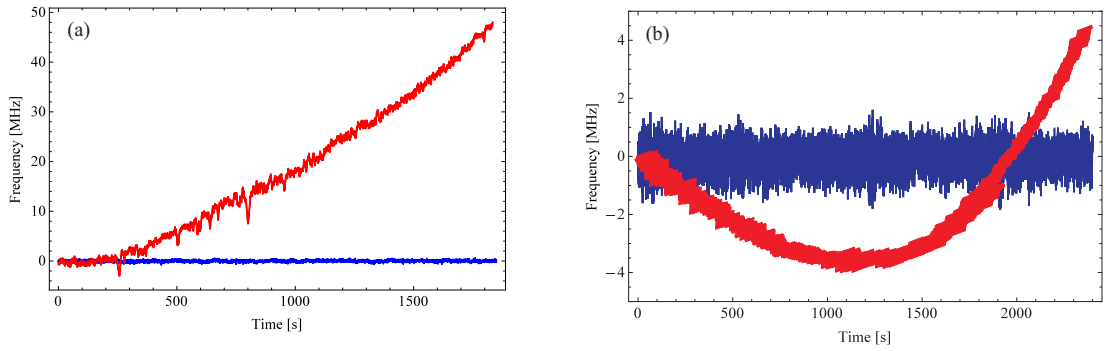

Figure 4.2: (a) Lock signal (blue) and correction (red) signal recorded with the laser cavity at atmospheric pressure. (b) Lock signal (blue) and correction (red) signal recorded with the laser cavity evacuated to 1.6 Torr.

and cavity pressure, we first present studies of the effects of current noise.

Fig. 4.3(a) shows the ADEV of the beat note at atmospheric pressure for a 780-nm cavity of design type A. A fit to the curve suggests that the data is dominated by white frequency noise at short times, and the floor reaches a value of 2.5×10^{-11} at $\tau = 40$ s. Fig. 4.3(b) shows the corresponding ADEV curve for the lock signal. Here, the floor reaches a value of 2×10^{-11} at $\tau = 80$ s. Figs. 4.3(c) and (d) show the ADEVs of the beat note and lock signal for a cavity of design type A using a current controller with a much smaller power spectral density (<100 pA/$\sqrt{Hz}$ from the manufacturer specifications), which is based on the design in reference [60]. For both pairs of Figs. 4.3(a), (b) and (c), (d), the time constant of the feedback loop was 50 ms. The same feed-forward circuit was used to provide low-frequency corrections to the piezo and high-frequency corrections to the current. The relative amplitudes of

these corrections was adjusted to optimize the quality of the lock. Fig. 4.3(c) shows that the ADEV of the beat note is reduced by nearly an order of magnitude, and that the floor value is 2×10^{-12} at an extended averaging time of $\tau = 300$ s. Similarly, in Fig. 4.3(d), the ADEV of the lock signal has a floor of 1.5×10^{-12} for $\tau = 300$ s. Based on these data sets, it is evident that the reduction in current noise strongly impacts the ADEV and improves the long-term stability, thereby extending the lock duration. Under these conditions, the floor of the ADEV of the laser intensity, which is also influenced by current noise, is 5×10^{-6} at $\tau = 10$ s, as shown later in greater detail in Chapter 7. We have also displayed polynomial fits to the data in Figs. 4.3(a) and (c).

Current noise also influences the laser linewidth, as shown by the data in Figs. 4.4(a) and (b). In Fig. 4.4(a), the Fourier transform of the beat note of two similar 780-nm lasers gives an individual laser linewidth of $\sim$1 MHz. The linewidth is reduced to $\sim$200 kHz with the lower noise current controller, as shown in Fig. 4.4(b). The laser linewidth is best modelled by a Voigt profile [44] with a Gaussian component representing the effect of current noise and a Lorentzian component representing the cavity linewidth. In reference [9] the record length of the spectrum analyser within the scan range permits these components to be resolved. Since our record length does not have sufficient point density, we perform fits to both Gaussian and Lorentzian functions. In both data sets, we find that the laser linewidth data is better

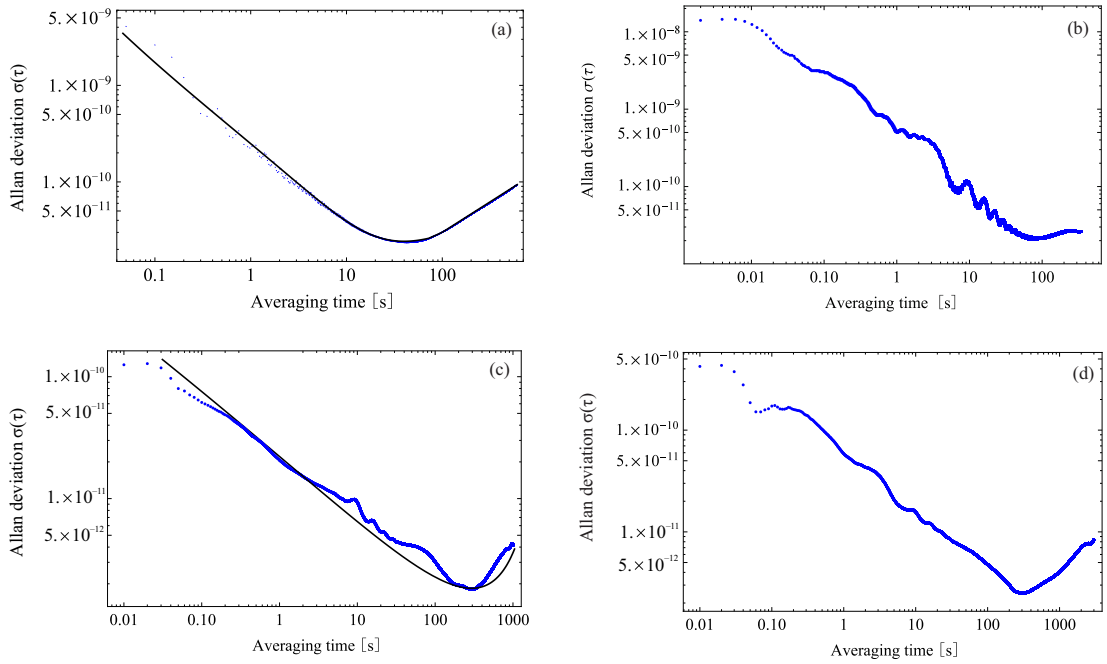

Figure 4.3: (a) ADEV of beat note obtained with two 780-nm lasers of design type A recorded using a current controller with a power spectral density of 200 nA/$\sqrt{Hz}$. The fit function, based on the Allan variance, is $(2.1 \times 10^{-10}\tau^{-1})^2 + (8.2 \times 10^{-11}\tau^{-1/2})^2 + (1.6 \times 10^{-11}\tau^{0})^2 + (1.5 \times 10^{-12}\tau^{1/2})^2 + (1.4 \times 10^{-13}\tau)^2$. (b) ADEV of lock signal of a single laser recorded with a current controller with a power spectral density of 200 nA/$\sqrt{Hz}$. The ripples in the ADEV curve are attributed to the resonant frequency of the vibration isolation platform. (c) ADEV of the beat note obtained with two 780-nm lasers of design type A recorded using a current controller with a power spectral density of 100 pA/$\sqrt{Hz}$. The fit function, based on the Allan variance is $(5.8 \times 10^{-13}\tau^{-1})^2 + (1.3 \times 10^{-11}\tau^{-1/2})^2 + (1.1 \times 10^{-12}\tau^{0})^2 + (1.6 \times 10^{-15}\tau^{1/2})^2 + (1.2 \times 10^{-14}\tau)^2$. (d) ADEV of lock signal of a single laser recorded with a current controller with a power spectral density of 100 pA/$\sqrt{Hz}$. For plots (a) and (c), the fit functions are computed based on the Allan variances rather than the ADEVs, since the resulting coefficients of the deviation add in quadrature.

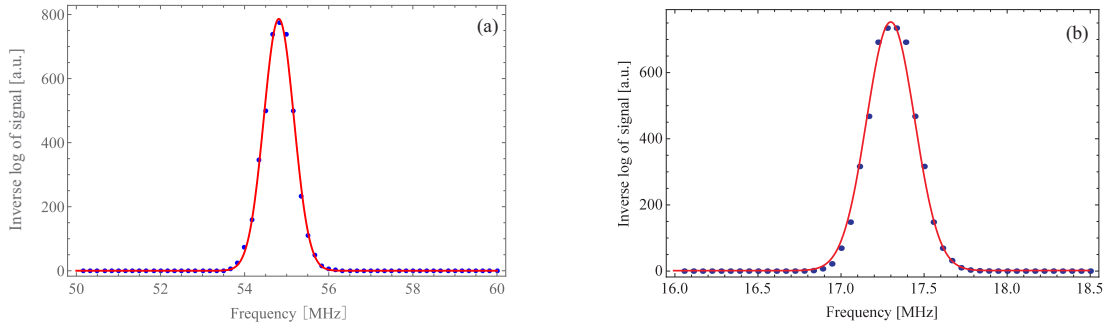

Figure 4.4: (a) Short-term beat note of two type-A 780-nm laser cavities recorded with a spectrum analyzer and a current controller with a power spectral density of 200 nA/$\sqrt{Hz}$. The Fourier transform of the beat note is displayed on a linear scale by taking the inverse logarithm. A Gaussian fit gives a FWHM of (1.136 $\pm$ 0.005) MHz. (b) A similar linewidth measurement as in part (a), obtained using a current controller with a power spectral density of 100 pA/$\sqrt{Hz}$. Here, a Gaussian fit gives a FWHM of (221 $\pm$ 1) kHz.

represented by a Gaussian fit than a Lorentzian function, suggesting that current noise dominates the effect of the intrinsic cavity linewidth. Although both lineshape functions model the central portion of the curve, the Lorentzian fit misses points in the wings. Accordingly, we find that the fit error for the Gaussian is consistently better than that of the Lorentzian.

In general, the beat note ADEV is considered to be a more representative measure of laser performance. In comparison, the lock signal ADEV can potentially be influenced by drifts in the lock point due to other external factors such as magnetic

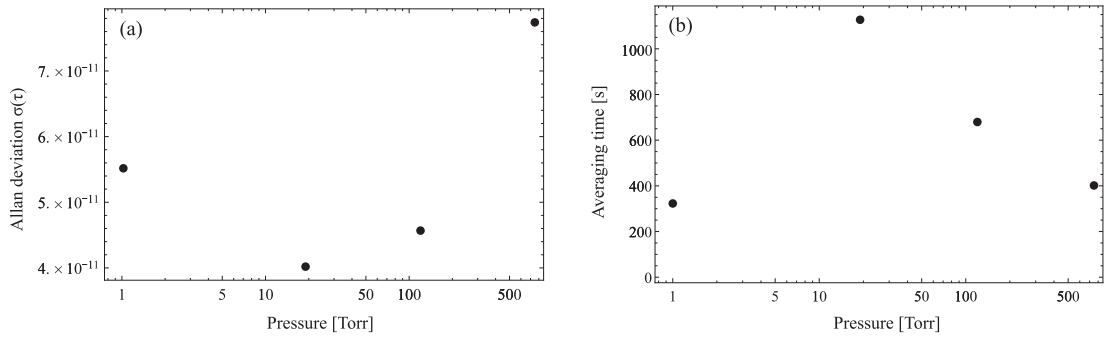

Figure 4.5: (a) Floor of ADEV curves of lock signal as a function of cavity pressure recorded with a 780-nm laser cavity of design type B. The typical scatter in the ADEV is ±10%. (b) Averaging time τ corresponding to the floor of the ADEV curves in part (a) as a function of the pressure inside the laser cavity. The typical scatter in the averaging time is ±10%.

fields and feedback loop parameters. However, based on the data in Fig. 4.3, it is evident that both measures are qualitatively similar. Since our lock studies extend to only about one hour – in which perturbations of the lock point are insignificant – we present only ADEVs of the lock signal to show the effects of pressure variations. Relying on the ADEV of the lock signal rather than the ADEV of the beat note also avoids the need to maintain two cavities at identical pressures.

We now examine the effect of pressure variations on the ADEV curves carried out with a 780-nm laser cavity of design type B using a current controller with a power spectral density of 200 nA/$\sqrt{Hz}$. For this study, we acquire ADEV curves over a single 12-hour run to best track relative changes. Based on Fig. 4.5(a), it is evident

that the floor of the ADEV values of the lock signal is reduced by about a factor of 2 at a pressure of 20 Torr compared to its atmospheric value. However, the ADEV increases slightly from 20 Torr to 1 Torr. Although cavity type B had pressure-release holes, both cavity types A and B can be affected by the slow escape of trapped gasses. We therefore attribute the increase below 20 Torr to outgassing of various sealants, epoxies, and residual gasses inside the laser cavity. The data in Fig. 4.5(b) shows that pressure reduction extends the value of the averaging time of the ADEV curve by approximately a factor of 3. It is therefore evident that both cavity pressure and current noise can have significant effects on the long-term stability. We find that the averaging time reduces when the pressure is decreased from 20 Torr to 1 Torr, which is consistent with the trends observed in part (a). Although pressure variations have a lesser impact on the floor of the ADEV curves than current noise, the extension of the averaging time at reduced pressures is just as pronounced as the effect of reducing the current noise. Therefore this data illustrates the benefit of using vacuum-sealed cavities for diode-laser systems.

4.2 Applications to metrology

In this section, we show that the long-term stability and auto-locking features of the laser system can be used for precise measurements of gravitational acceleration by integrating the laser system with an industrial gravimeter. Gravimeters are sensitive

to variations in the value of the acceleration due to gravity $\boldsymbol{g}$ on the Earth's surface. They can be designed to measure the absolute value of $\boldsymbol{g}$ or relative changes due to temporal effects such as tides and positional variations due to changes in density. Therefore, gravimeters play a ubiquitous role in the exploration of natural resources by detecting characteristic density profiles associated with minerals, petroleum, and natural gas. In particular, these devices provide a non-invasive technique for exploration in wide-area (air, sea, or submersible) mineral assays and borehole mapping for verifying properties of rocks, determination of bulk density detection of cavities, and tidal forecasts. They are also used for seismic monitoring of environmentally sensitive areas that are designated for resource extraction.

The most accurate portable absolute gravimeter is based on a falling corner cube Mach-Zehnder optical interferometer (Scintrex FG5X) [36], in which one arm containing a retro-reflecting corner cube falls in gravity inside a vacuum chamber. Measurements of $\boldsymbol{g}$ accurate to $\sim$2 ppb have been realized by recording the chirped accumulation of fringes over a drop height of $\sim$0.3 m. The accuracy depends on the frequency stability of an iodine-stabilized 633-nm He-Ne laser used for interferometry. This laser has a power output of $\sim$100 μW, a linewidth of $\sim$10 kHz, and an ADEV of $\sim 10^{-11}$ that is traceable to the performance specifications of primary frequency standards. In this section, we compare measurements of $\boldsymbol{g}$ under laboratory conditions using an auto-locked 633-nm diode-laser system and an iodine-stabilized He-Ne

laser.

For the gravimetric measurement, light from the laser source is split into two paths – a reference beam along the horizontal, and a measurement beam along the vertical, which is incident on the corner cube retro-reflector. After the corner cube falls in gravity, it is gently brought to rest and reset. The change in path difference between the two arms of the interferometer produces a chirped heterodyne beat note resulting in a signal with zero-crossings which are timed and counted. The value of $\boldsymbol{g}$ is determined from a fit to the resulting displacement-time graph. The precision depends on the drop height, and scales as the square of the drop time. The fit includes corrections for systematic effects such as the Earth's gravitational gradient and laser modulation frequency. Models for tidal variations are also used to correct temporal changes in $\boldsymbol{g}$ so that a baseline of gravity values obtained over a few hours can be used to compare the two laser systems. In this work, the value of $\boldsymbol{g}$ was obtained by performing 100 drops of the corner cube over a period of 5 minutes, and repeating this sequence every half an hour for several hours.

Fig. 4.6 shows measurements of $\boldsymbol{g}$ using the auto-locked diode-laser system stabilized with respect to the P(33)6-3 branch in iodine vapour at 633 nm using a current controller with a power spectral density of 200 nA/$\sqrt{Hz}$. Each individual point represents an average of 100 drops of the corner cube, as defined by the Scintrex measurement protocol. The zero baseline represents the values established by the

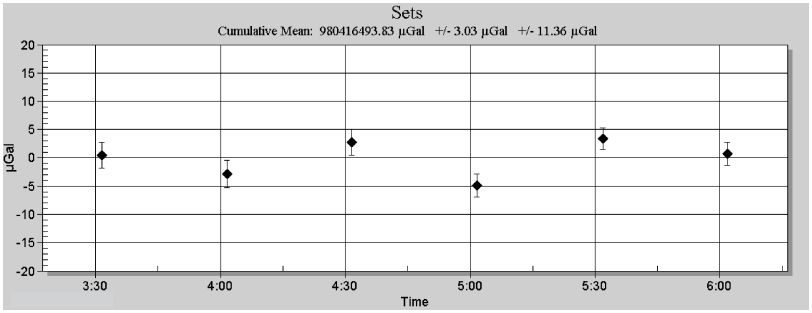

Figure 4.6: Measurements of $\boldsymbol{g}$ obtained with an auto-locked diode laser at 633 nm integrated with the Scintrex FG5X gravimeter. Each point represents an average of 100 drops of the corner-cube reflector. This sequence was repeated at intervals of 30 minutes for a time period of 3 hours. The zero represents the baseline established by an iodine-stabilized He-Ne laser.

iodine-stabilized He-Ne laser. The typical standard deviation for a single set of 100 measurements is 18 ppb which corresponds to 18 μGal (where 1 Gal = 1 cm/s^2) and the root-mean-square value of the fit residuals of the displacement-time graphs is 3 nm. The overall uncertainty for the entire data set (statistical uncertainty of 3 μGal and a systematic uncertainty of 11 μGal) shows that the two lasers produce measurements in agreement with each other. The signal-to-noise ratio was limited by the input optical power of the detector, which was optimized for the 100-μW output of the He-Ne laser. As a result, we can expect further improvements since the auto-locked diode-laser system is capable of power outputs of $\sim$100 mW.

We now describe an application of the laser system relevant to LIDAR trans-

mitters. LIDAR sources are widely used for atmospheric pollution monitoring and there has been considerable interest in developing diode laser-based LIDAR sources [61, 62]. The ability of LIDAR to detect water vapour has also enabled these systems to be adapted for planetary exploration such as the investigation of the hydrological cycle on Mars as part of the NASA Phoenix mission [63]. The auto-locking feature of the diode lasers described in this work coupled with a pattern-matching algorithm allows the laser frequency to be locked to a spectral line and to be tuned with a programmable offset with respect to the peak. In this section, we utilize these features to demonstrate a key step toward the realization of a differential absorption LIDAR (DIAL) transmitter. The standard measurement technique for DIAL-type LIDAR [64, 65, 62] involves the absorption and scattering of pulsed laser light propagating through the atmosphere. Light is emitted into the atmosphere, and the light that is scattered back is detected and recorded as a function of propagation time. The density of a desired aerosol can be determined by comparing the intensity of laser backscatter to a reference signal at an off-line wavelength that is not absorbed. A pulsed laser system that can operate at both wavelengths can be realized by integrating the auto-locked diode laser with a semiconductor tapered amplifier waveguide [5] for power amplification and an acousto-optic switch to realize a pulsing module with repetition rates of up to 1 MHz [66]. Unlike traditional DIAL-type LIDAR transmitters that rely on a pulsed YAG or diode laser and a separate laser-based measurement

of the off-line signal, we anticipate using a single auto-locked master oscillator that can be locked and tuned to multiple frequencies with respect to atomic or molecular spectral lines as well as their corresponding off-line points. Here, we show that a solid-state temperature-tunable spectral marker (transmission spectrum of FBG) can be calibrated against known hyperfine splittings of atomic lines so that the frequency of a LIDAR transmitter can potentially be extended to a region in which convenient frequency markers are unavailable.

Fig. 4.7(a) shows the transmission peak from an FBG in the 780-nm band, which has a FWHM of 70 MHz. The portion of the fiber containing the FBG ($\sim$1 cm in length) was encased in a thermally-conductive paste and temperature tuned and stabilized with a Peltier cooler so that the transmission peak could be calibrated against rubidium hyperfine lines. Fig. 4.7(b) shows the tunability of the FBG peak as a function of temperature. This data was recorded with a Ti:Sapphire laser since it had a larger mode hop-free scan range than the ECDL. The slope of (-2.90 $\pm$ 0.13) GHz/degree and the range of the temperature controller imply that the lock point can be tuned over a frequency range of approximately 300 GHz. In this set-up, the resolution of the temperature tuning of the FBG peak allows the lock point to be changed in steps of 3 MHz, which is significantly smaller than the typical pulse bandwidth of a LIDAR transmitter (10 MHz). Fig. 4.7(c) shows the ADEV of the laser frequency locked to the FBG transmission peak. The floor value of the ADEV

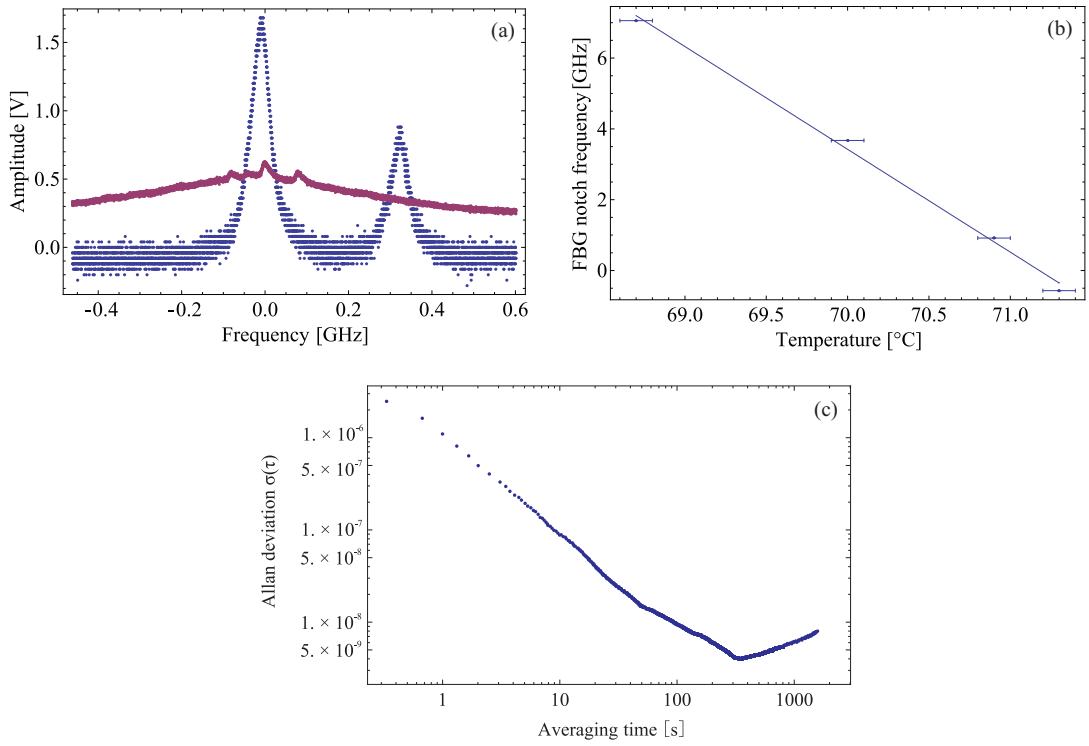

Figure 4.7: (a) Calibration of the FBG peak using rubidium resonances. The highest peak in the blue curve, which represents the FBG transmission spectrum was used for calibration. The secondary peak is related to strain and polarization-dependent effects. The red curve represents a saturated absorption spectrum in ^{87}Rb. The FWHM of the FBG transmission peak was inferred to be (70 $\pm$ 1) MHz. (b) Tunability of the FBG transmission peak as a function of temperature performed using a Ti:Sapphire laser. (c) ADEV of lock signal recorded with a 780-nm diode laser cavity of type A that was frequency stabilized to the FBG peak.

(4×10^{-9}) corresponds to a frequency excursion of 1.4 MHz in 350 s. Since the LIDAR can be operated at repetition rates of 1 MHz, it implies that the frequency drifts can remain small compared to the pulse bandwidth until approximately a billion pulses are applied, which constitutes a comfortable measurement window. The ADEV is significantly worse than the data obtained with the lasers locked to atomic resonances (Fig. 4.3) since the frequency stability of the FBG system is limited by the resolution of the temperature controller. As a consequence, further improvements can be expected with a higher-resolution controller. We note that we have relied on the ADEV of the lock signal in Fig. 4.7(c) rather than the ADEV of the beat note to infer system performance. This procedure seems to be justified, since the ADEV of the lock stability and of the beat note showed similar trends in Fig. 4.3. Nevertheless, the $1/\tau$ dependence of the data from 0.3 s to 50 s – which is not expected for a frequency-locked oscillator – could suggest that additional beat note measurements would be required to conclusively establish the observed trends.

While we do not describe the design of the LIDAR receiver and its integration with the transmitter, it is possible that the versatility of this design will allow the nature of the excitation pulses to be tailored to the distribution of trace gases and pollutants that can be detected. For example, it is possible to envision a heterodyne detection system in which a cw local oscillator derived from the master laser can be used to generate a beat note from the back-scattered signals. Since the repetition

rate is easily controlled, it should be possible to operate at a low repetition rate and detect the zones from which the return signals arise. The repetition rate can then be adjusted to increase the signal-to-noise ratio. It is also possible to chirp successive pulses and alter the frequency at which the return signals are detected. Further, the pulses can also be generated in bursts with an adjustable duty factor. All these features, combined with the ability to generate on-line and off-line lock points in a spectral range where wavelength references are not readily available suggest that this system could have significant advantages.

5 Photon echo: theory

We begin this chapter with a comparison of atomic lifetime measurements, and discuss the principles and advantages of the photon echo technique. This is followed by an overview of the optical Bloch vector model, which allows the time-dependent polarization and electric field to be calculated.

5.1 Overview of lifetime measurements

Atomic lifetime measurements are used to confirm theoretical predictions for atomic level structure such as dipole matrix elements, polarizabilities, and binding energies. In recent years, increases in computational power have allowed accurate, relativistic, many-body perturbation-theory calculations of not only lower levels of hydrogen-like atoms, but also properties of upper levels of heavier atoms. The calculations are widely used for interpretation of spectroscopic signatures in a variety of applications, ranging from astrophysics to industry in the area of photonics and laser spectroscopy [67, 68]. The best lifetime measurement to date (based on photoassoci-

ation) has achieved a statistical uncertainty of 0.007% and a systematic uncertainty of 0.03% [69], whereas the characteristic accuracy of other commonly-used techniques [22, 24, 25, 70] and theoretical calculations [67, 68] is at the level of 0.2%. These experiments involve measurements of the natural linewidth (on the order of a few megahertz in alkali atoms) using absorption spectroscopy [22] or studies of radiative lifetime in samples such as laser-cooled atoms [25, 22] and atomic beams [24]. The most prominent systematic effect in absorption measurements is the laser linewidth, making it necessary to develop lasers with kilohertz linewidths [22]. For measurements of radiative lifetimes, it is necessary to operate at low densities to avoid the effects of radiation trapping, thereby making it essential to develop photon-counting techniques that can result in longer data acquisition times [24, 25, 70]. Both types of measurements have additional complexities associated with sample preparation such as state-selection of atoms, non-magnetic set-ups for atom trapping, and highly collimated atomic beams that need to be spatially imaged so that the distance over which excited atoms fluoresce can be converted to time from the knowledge of the speed distribution [24]. Other motivations for accurate lifetime measurements [71, 72] and their comparison with theory [73, 74] are related to tests of the standard model involving parity nonconservation. Table 5.1 shows a comparison of leading atomic lifetime measurements. Such comparisons can be further validated by performing measurements using experimental techniques with different systematic effects [75, 76, 77, 78].

Table 5.1: Comparison of lifetime measurements achieved by leading techniques. The last two entries represent the most accurate theoretical calculations.

Reference	**Technique**	**Rb lifetime measurements**	**Accuracy**
[22]	Linewidth of laser-cooled atoms (Na)	N/A	0.25%
[24]	Supersonic atomic beams (Li, Na, K, Rb)	$5^2P_{1/2}$: 27.70(4) ns $5^2P_{3/2}$: 26.24(4) ns	0.14%–0.25%
[25]	Photon counting in atom trap (Fr and Rb)	$5^2P_{1/2}$: 27.64(4) ns $5^2P_{3/2}$: 26.20(9) ns	0.15%–0.37%
[72]	Photon counting in atomic beam (Cs)	N/A	0.2%–0.3%
[69]	Cold atom photoassociation (Li)	N/A	0.03%
[70]	Photoassociation spectroscopy in ^{87}Rb	$5^2P_{1/2}$: 27.75(8) ns $5^2P_{3/2}$: 26.25(8) ns	0.3%
[67]	Relativistic perturbation theory in Rb	$5^2P_{1/2}$: 26.82 ns $5^2P_{3/2}$: 26.44 ns	N/A
[68]	Relativistic perturbation theory in ^{87}Rb	$5^2P_{1/2}$: 27.41 ns $5^2P_{3/2}$: 26.02 ns	N/A

Another well-established technique that has been extensively exploited to measure relaxation effects in solids [79, 80, 81], collisional relaxation in gases [82, 83], and molecular lifetimes [84] is based on optical photon echoes [27, 28, 83]. A photon echo experiment can eliminate many of the aforementioned specialized requirements for atomic lifetime measurements. Such an experiment requires the excitation of a two-level atomic system by two travelling-wave pulses that are temporally separated by $t = T$. The first pulse prepares a coherent superposition of ground and excited states, which produces coherent radiation along the direction of the excitation pulse. In a classical description, the radiation terminates due to Doppler de-phasing when the individual atoms of a dilute gas travel a distance larger than the wavelength of light. The duration of this transient signal, known as FID, is on the order of $\lambda/u = 1$ ns in a room-temperature gas of Rb atoms, where u is the most probable speed and λ is the wavelength of light. However, if the excited state has not decayed, a second excitation pulse can rephase the superposition state at a time $t = 2T$, resulting in a burst of radiation known as a photon echo [29]. The radiation associated with the FID and the photon echo is analogous to coherent emission from a phased array of dipole oscillators. The main limitation on the time scale of the experiment is the radiative lifetime of the excited state. Therefore, the exponential decay of the echo intensity (energy radiated by the system) as a function of T can be used to infer the radiative lifetime τ_1, as illustrated in Fig. 5.1.

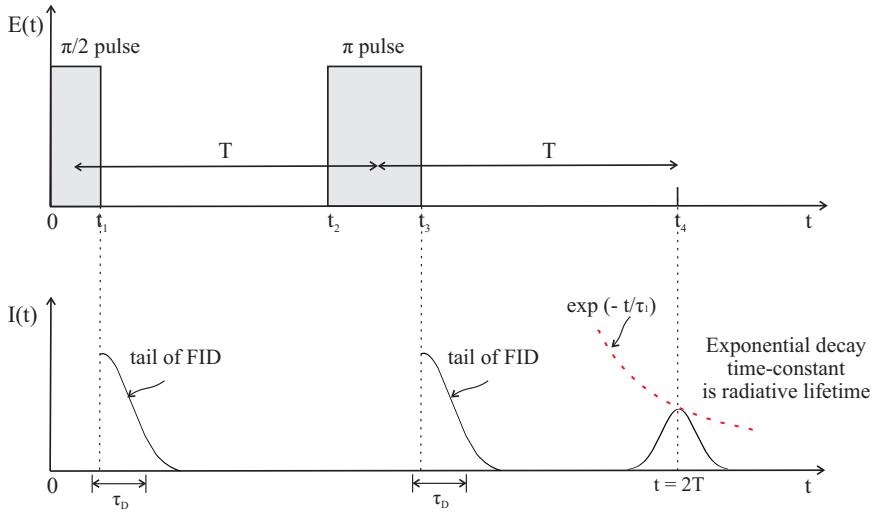

Figure 5.1: Top figure shows an idealized representation of two square $\pi/2$ and π excitation pulses with their centers separated by T. The bottom figure shows the FID due to each pulse and an echo signal at $t = 2T$. The second pulse can be applied even a long time after the FID to rephase the atoms in the excited state, as long as this state has not decayed. The exponential decay time constant τ_1 of the echo intensity is measured as a function of T.

A striking aspect of the photon echo technique is that the coherent emission is directional, with a signal strength that can be many orders of magnitude larger than the signals used in lifetime measurements that rely on monitoring isotropic spontaneous emission. Other advantages are that it does not impose stringent requirements on the laser linewidth. Since the time scale of the measurement is less than 500 ns, it is sufficient to ensure that the excitation pulses are phase coherent over this time period. Consequently, the experiment can be carried out with megahertz-linewidth lasers in contrast to kilohertz-linewidth lasers used in other work [22]. A narrow laser linewidth becomes unnecessary because the pulse bandwidth – which is significantly larger than the laser linewidth – determines the fraction of excited atoms under the Doppler profile. Although typical laser phase noise can be expected to average out, and therefore only weakly impact the decay time of the echo intensity, it is still necessary to quantify this effect. Most significantly, like other vapour-cell experiments [85], it has the potential for realizing data acquisition with a large repetition rate. Furthermore, the experiment is not sensitive to radiation trapping. This is because the sample density, which can affect the propagation of the echo pulse [28, 86], does not impact the total energy as a function of T that is used in the lifetime measurement. Moreover, the sensitivity relies on the ability to measure the energy radiated as a function of precisely-incremented delay times T, and not on details such as the onset times of the excitation pulses or the time occurrence of the echo signal. Despite

these advantages, this technique appears to have been largely overlooked for precision measurements of atomic lifetimes [28, 87].

The first measurement of the $5^2P_{3/2}$ excited state lifetime ($\sim$26 ns) in Rb vapour using the photon echo technique reported a "double-blind" lifetime value with an accuracy of 1% using 20-ns excitation pulses [87]. This preliminary measurement involved recording 300 points on the exponential decay, with each point being averaged 128 times at a repetition rate of 20 Hz, resulting in a measurement time of one hour. The characteristic precision of a single data set was $\sim$10%, and in the absence of systematic effects, 72 hours of data acquisition was required to produce the 1% accuracy. The agreement of this result with the best measurements in Rb [25, 24, 70] served as an impetus for this work. Here, we explore the sensitivity of the echo technique and its potential for realizing the most accurate measurement of any atomic lifetime. We use 12-ns excitation pulses to reduce the effects of spontaneous emission during excitation, and a data acquisition system that can operate the experiment at a repetition rate of up to 1 MHz to measure the $5^2P_{3/2}$ excited-state lifetime in ^{85}Rb. We report a transit time-corrected lifetime value of (26.10 $\pm$ 0.03) ns based on 4 hours of data acquisition over several weeks, which agrees at the level of 1σ with the best measurement in Rb [25], as indicated in Table 5.1, but it disagrees with the values reported in references [24, 70]. The statistical precision of 0.11% is based on an ADEV analysis of the data. We find that this measurement is dominated

by noise sources that occur on time scales longer than 50 ms. These noise sources produce variations in the lifetime values that limit a conclusive study of systematic effects. Nevertheless, we find that none of the experimental control parameters produce changes in the lifetime value larger than the statistical uncertainty. We attribute the source of the long-term variations to imperfect background subtraction of excitation pulse tails and present a simple model that supports these conclusions. The model also suggests a practical approach for reducing the long-term variations. Our studies of the fractional uncertainty in the lifetime suggest that the repetition rate achievable in this experiment can result in a statistical precision of 0.03%, which would allow a rigorous study of systematic effects at the same level.

5.2 Description of the Bloch vector model

An analytical treatment for calculating the echo intensity is given in reference [28]. This treatment ignores the effects of atomic recoil, and is based on the optical Bloch equation model for a two-level atom in a rotating frame, as described by the following torque equation:

$$\frac{d\boldsymbol{\rho}}{dt} = \boldsymbol{\Omega'} \times \boldsymbol{\rho}. \tag{5.1}$$

Here, the Bloch vector $\boldsymbol{\rho} = (u, v, w)$ has components u and v that represent the in-phase and in-quadrature components of the dipole moment, respectively; w is the

population difference between the ground and excited states, and the components of the generalized Rabi frequency are given by $(-\Omega, 0, \Delta)$ so that $\Omega' = \sqrt{\Omega^2 + \Delta^2}$, where the Rabi frequency is represented by Ω and the detuning is represented by $\Delta = \omega - \omega_0$. Here, ω is the driving frequency and ω_0 is the resonant frequency. This model does not include the effects of spontaneous emission and pulse propagation.

Fig. 5.2 shows a representation of the photon echo experiment using the Bloch vector model. The first excitation pulse exerts a torque on the Bloch vector for the system, which is initially pointing down along the w axis, corresponding to atoms in the ground state. After excitation, the radiation from the phased array of dipole moments decays due to the dephasing of individual Bloch vectors in the horizontal plane. The second excitation pulse of area π rephases the Bloch vectors, so that a macroscopic state vector is formed at $t = 2T$. It should be noted that the phase of the rephased dipole moment is opposite the phase of the initial dipole moment. The illustration in Fig. 5.2 also ignores spontaneous emission, which would cause the Bloch vectors to shorten as a function of time.

The time-dependent solutions to Eq. (5.1) can be obtained on the basis of successive rotational transformations which give

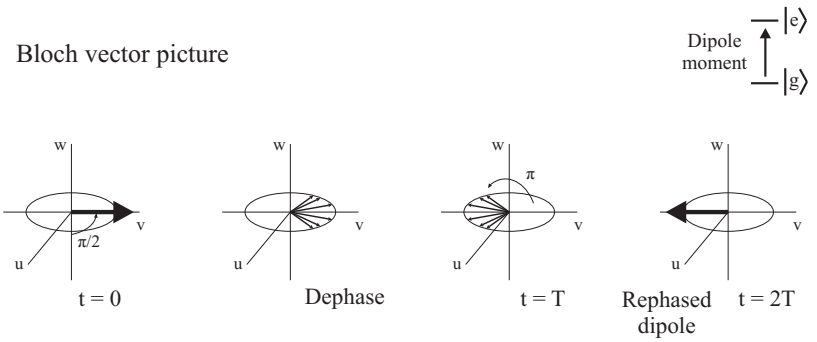

Figure 5.2: Representation of the photon echo experiment in the Bloch vector picture. At $t = 0$, the torque due to the driving electric field establishes a macroscopic Bloch vector, which corresponds to a 50:50 superposition of ground and excited states. Doppler dephasing produces a spread in the evolution of the individual Bloch vectors. A second excitation pulse applied at $t = T$ results in rephasing of individual Bloch vectors, and produces a macroscopic Bloch vector at $t = 2T$. The illustration ignores the effect of spontaneous emission, which would reduce the length of the rephased Bloch vector.

$$\begin{bmatrix} u(t) \\ v(t) \\ w(t) \end{bmatrix} = \begin{bmatrix} \dfrac{\Omega^2 + \Delta^2 \cos\Omega' t}{\Omega'^2} & \dfrac{-\Delta}{\Omega'} \sin\Omega' t & \dfrac{-\Delta\Omega}{\Omega'^2}(1 - \cos\Omega' t) \\ \dfrac{\Delta}{\Omega'} \sin\Omega' t & \cos\Omega' t & \dfrac{\Omega}{\Omega'} \sin\Omega' t \\ \dfrac{-\Delta\Omega}{\Omega'^2}(1 - \cos\Omega' t) & \dfrac{-\Omega}{\Omega'} \sin\Omega' t & \dfrac{\Delta^2 + \Omega^2 \cos\Omega' t}{\Omega'^2} \end{bmatrix} \begin{bmatrix} u_0 \\ v_0 \\ w_0 \end{bmatrix}. \qquad (5.2)$$

Here, u_0, v_0, w_0 represent the initial values of the Bloch vector and $\Omega = 2dE_0/\hbar$ is the Rabi frequency specified in terms of the electric field amplitude E_0 and the dipole moment d. The solutions represented by Eq. (5.2) impose no limit on the value of the Rabi frequency and can model the time-dependent Bloch vector components for a wide range of experimental conditions, including on-resonant and far-off resonant excitation. Eq. (5.2) can be simulated with the inclusion of spontaneous emission and the spatial profile of the excitation beam [87]. For Delta-function excitation pulses, the ratio of pulse areas $r = \theta_2/\theta_1$ (where θ_1 and θ_2 are the areas of the first and second pulse, respectively) required for the maximum echo intensity has a value of 2, corresponding to a $\pi/2$ – π pulse sequence [28]. Here, the pulse area is defined by $\theta = \int_0^{\tau_p} \Omega(t)dt$, where τ_p is the excitation pulse width. Simulations of Eq. (5.2) with either square pulses or Gaussian pulses show that r has a value of 1.89 and 1.70, respectively. For Gaussian pulse excitation, the value of r is further reduced to 1.44 if spontaneous emission is included through the introduction of phenomenological decay terms in Eq. (5.2). These results are in general agreement with the experimental value of 1.2 obtained with 20-ns excitation pulses [87].

For square-pulse excitation (Fig. 5.1) in the limit that $\Omega \gg \Delta$, Eq. (5.2) can also be used to obtain an analytical expression for the atomic polarization density of the photon echo [28], as given by

$$P(t_4) = -\xi d \sin(\omega + \Delta) t_4 \times \exp\left[-\frac{\pi}{4}\left(\frac{t_{43} - t_{21} - 1/\Omega}{T_2^*}\right)^2\right], \tag{5.3}$$

where ξ is the number density. If $1/\Omega \ll T$, this equation predicts that the duration of the echo signal envelope is dominated by the inhomogeneous (Doppler dephasing) time T_2^*. If the excitation pulse bandwidth only excites a fraction of the Doppler width, the value of T_2^* becomes the pulse width. To calculate the electric field, the polarization density in Eq. (5.3) can be used as the source term in the wave equation given by

$$\frac{\partial^2 E(x,t)}{\partial x^2} - \frac{1}{c^2}\frac{\partial^2 E(x,t)}{\partial t^2} = \mu_0 \frac{\partial^2 P(x,t)}{\partial t^2}. \tag{5.4}$$

In the presence of spontaneous emission, the echo intensity I (at $t = 2T$) can be obtained from the propagated electric field given by Eq. (5.4). If a phenomenological decay rate $1/\tau_1$ is included to account for spontaneous emission, the echo intensity can be modelled as

$$I = I_0 \exp\left[-\frac{2T}{\tau_1}\right], \tag{5.5}$$

where I_0 is the peak intensity. This model ignores the effects of other dephasing mechanisms, such as collisions and transit time. Reference [28] predicts small deviations in the echo time in the vicinity of $t = 2T$ for specific pulse areas. However, in the experiment, we integrate the echo intensity over the echo envelope and plot the resulting energy as a function of $2T$ to measure τ_1.

6 Photon echo: experimental details

The key requirements for this experiment include excitation pulses that are comparable or shorter than the atomic lifetime (∼26 ns), low background light so that the atomic coherences remain unperturbed during the measurement, rapid data acquisition to avoid long-term noise sources that can contribute to lifetime variations, and detection systems that can avoid saturation and still temporally resolve an echo signal that is approximately 1,000 to 100,000 times smaller in intensity than the excitation pulses. Additionally, the spatial profile of the excitation beam should be sufficiently large to minimize transit time corrections to the atomic lifetime, while still ensuring adequate atom-field coupling strengths for the excitation pulses to compensate for vapour absorption and spontaneous emission during excitation. The experiment exploits the benefits of a fiber-coupled master oscillator power amplifier (MOPA) laser system [5] coupled through a chain of AOMs to generate short pulses. The signal detection is accomplished by either a balanced heterodyne detector with an electronic gate or a photo-multiplier tube (PMT) gated by an AOM.

6.1 Optical set-up

The experimental set-up is shown in Fig. 6.1. We use an ECDL that is frequency stabilized to the $F = 3 \rightarrow F' = (3, 4)$ cross-over resonance, as well as to neighbouring resonances within the Doppler profile in ^{85}Rb using a saturated absorption spectrometer with a room-temperature Rb vapour cell that is 5 cm in length. Fig. 6.2 shows the energy-level diagram for ^{85}Rb. The 50-mW output of the ECDL is amplified to 200 mW by a TA and fiber-coupled so that it can seed a number of TAs simultaneously. References [88, 89] show that the spectral characteristics of the amplified light are well matched with those of the seed laser. The photon echo experiment relies on a TA with a 30-mW fiber-coupled input to produce an output of 1.7 W. After passing through a Faraday isolator and beam shaping lenses, this beam is spatially filtered using an optical fiber. The role of the fiber is to reduce the amplified spontaneous emission associated with the TA output, and to achieve a Gaussian spatial profile that can be diffracted with a high efficiency by AOMs. The fiber-coupled output of 400 mW is aligned through two successive AOMs operating at 250 MHz. The first ("upstream") AOM produces an up-shift of 250 MHz and operates in the Bragg regime with a gently-focused laser beam to achieve a diffraction efficiency of $\sim$70%. This AOM provides a gate pulse for the experiment (FWHM of 500 ns) to suppress background light from going into the experiment. The second ("downstream") AOM

is aligned to produce a down-shift of 250 MHz. The laser beam is focused to a spot size of ∼30 μm through this AOM to generate Gaussian pulses with a FWHM of ∼12 ns, as shown in Fig. 6.3. As a result, the diffraction efficiency is reduced to ∼35% which ensures that the excitation beam has a peak power of 100 mW. The diffracted beam from the downstream AOM is thus tuned back to the original lock point, which is within the Doppler profile of the $F = 3 \rightarrow F' = 2, 3, 4$ transitions. Both the upstream and the downstream AOMs are pulsed to generate the two-pulse excitation sequence. The excitation beam has an elliptical spatial profile with $1/e^2$ half-widths of ∼1.5×1.0 mm^2 (with an estimated uncertainty of 10%). From the peak intensity and the average beam radius, we estimate that the maximum pulse area for a 12-ns second excitation pulse is ∼15π. The ratio of the areas for the excitation pulses range from 1.3 to 1.5. The first-order diffracted beam of the downstream AOM is sent through a 10-cm long Rb cell. Since the excitation pulses are collinear, the echo is emitted along the same direction. The cell is surrounded by heating tape and insulated so that its temperature can be increased and stably maintained to ±1°C. We generally operate at a temperature of ∼40°C, at which the Rb vapour pressure is ∼3 $\times 10^{-6}$ Torr. The insulated cell is placed inside a solenoid that allows the magnetic field along the direction of excitation to be varied by ±20 Gauss. It was also possible to vary the polarization of the excitation beam from linear to circular with the use of wave-plates.

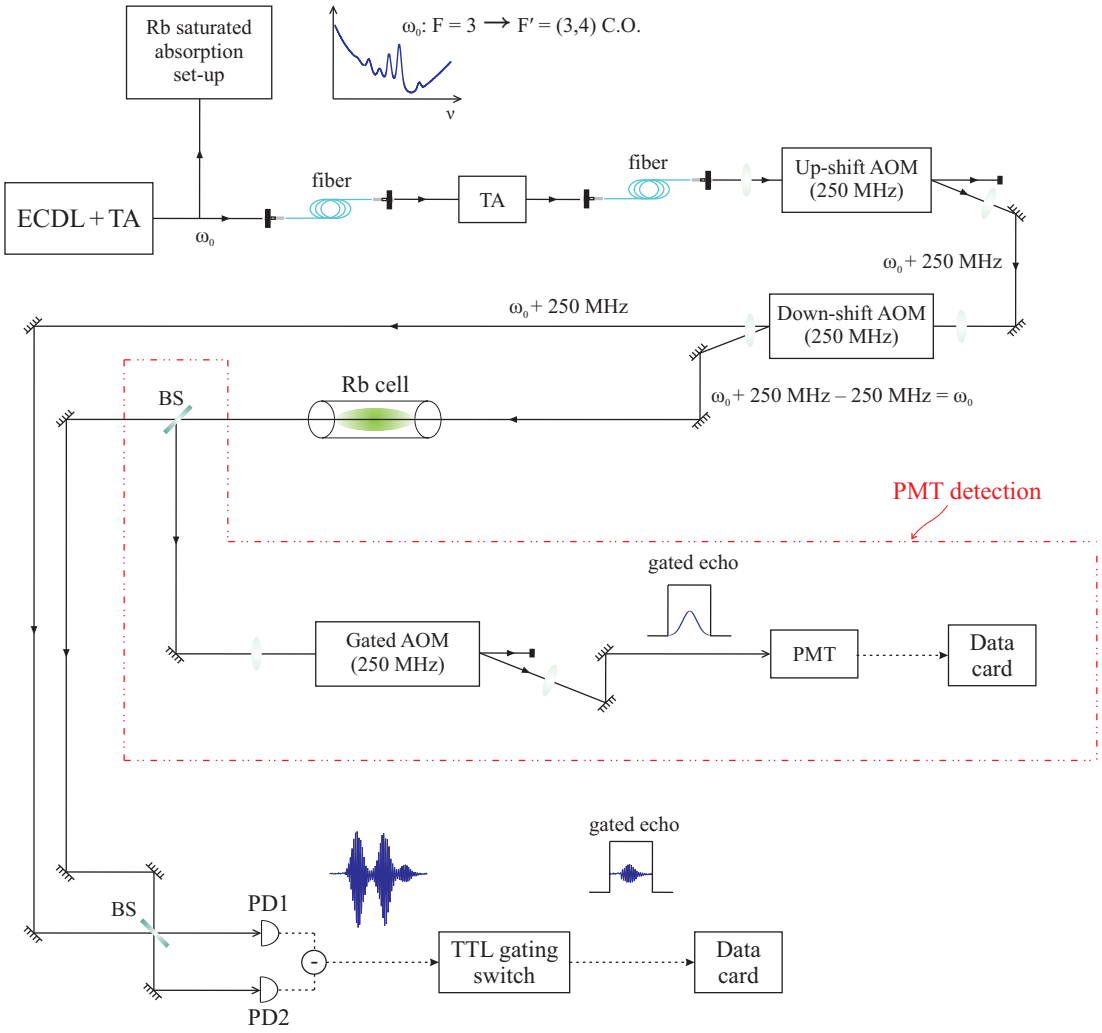

Figure 6.1: Experimental layout showing the seed laser, TA, AOM chain, and heterodyne detector. ω_0 designates a cross-over (C.O.) resonance. The dashed lines show the experimental layout involving PMT detection.

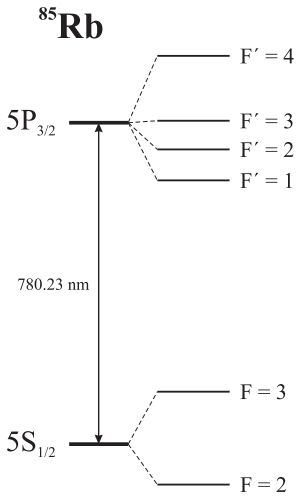

Figure 6.2: Energy-level diagram for ^{85}Rb. The photon echo experiment relies on exciting the $F = 3 \rightarrow F' = 2, 3, 4$ transitions within the Doppler profile.

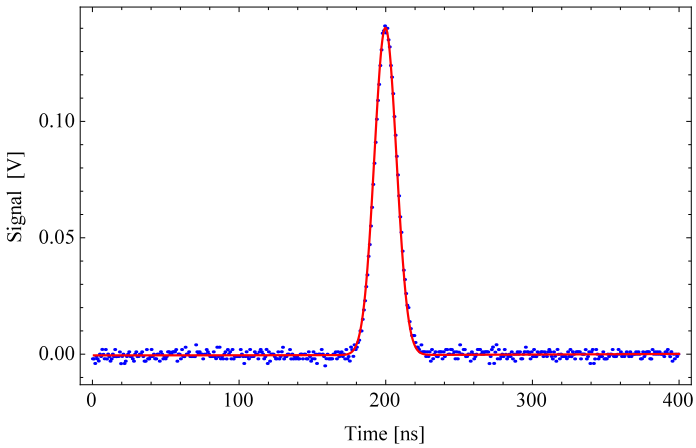

Figure 6.3: Excitation pulse FWHM of (11.64 ± 0.04) ns.

For the heterodyne detection set-up shown in Fig. 6.1, the undiffracted beam from the downstream AOM serves as a local oscillator (LO), which is aligned parallel to the excitation beam (diffracted beam from downstream AOM) outside of the Rb cell. Since the LO frequency is up-shifted with respect to the excitation beam, any background light that scatters into the cell from this beam can be resonant with the Doppler-broadened transition. The electric field of the photon echo signal is detected by overlapping with the LO to generate a 250-MHz beat note, which is recorded by a pair of balanced PIN photodiodes (1-ns rise time) in an optical heterodyne set-up. The output of the heterodyne detector is sent into a 25-dB RF amplifier and gated by a transistor-transistor logic (TTL) switch so that only the echo signal is sent to the data card. In the alternate detection scheme, the echo intensity is recorded on a PMT with a rise time of 1 ns. An additional 250-MHz AOM is used to gate the echo signal so that the PMT is not exposed to the excitation pulses, as shown in the dashed region of Fig. 6.1.

In order to observe the echo signal, we ensured that the LO frequency was up-shifted by 250 MHz with respect to the diffracted beam so that any background light from the LO was far off-resonance with the energy levels of the $F = 3 \rightarrow F' = 2, 3, 4$ transitions, thereby avoiding spontaneous emission within the vapour cell. The frequencies of the LO and diffracted beams were independently verified using absorption spectroscopy. As an additional precaution, the LO was routed outside

of the Rb cell. To obtain the best wavefront matching and the largest beat note, and to minimize the effect of vibrations that can cause the beat note amplitude to average out to zero, it was necessary to ensure that the path lengths for the LO and diffracted beams were similar and contiguously aligned with the same number of optical elements. We also ensured that the signal beam and the LO reflected off the same number of surfaces so that the same spatial parity was maintained for both pairs of heterodyne beams incident on the photodiodes in Fig. 6.1. Another consideration was to achieve the beat note alignment with suitably-expanded beams in order to increase the number of atoms contributing to the signal and the transit time. Estimates suggest that all these modifications improved the signal size by a factor of $\sim$30, thereby allowing the echo to be observed with an adequate signal-to-noise ratio.

A number of iterations and improvements of the experimental set-up were also required in order to obtain the best configuration for the echo signal shown in Fig. 6.1. An initial excitation scheme involved sculpting each excitation pulse produced by the upstream AOM with a corresponding pair of slightly narrower, nested excitation pulses driving the downstream AOM. This technique aimed to significantly reduce the width of the excitation pulses. However, the long time scale associated with the turn-on and turn-off of the upstream AOM pulses resulted in incomplete turn-off of light between the excitation pulses. As a result, this method had to be abandoned and

the upstream AOM was gated by a longer pulse encompassing both excitation pulses produced by the downstream AOM and the echo. This configuration was effective in reducing the background light passing through the vapour cell, both before and after the excitation pulses.

Another modification of the optical alignment involved operating the downstream AOM in the Bragg regime, so that high efficiencies in the first-order diffracted beam could be achieved. Under these conditions, the focused spot size was of order 100 μm, generating Gaussian pulses with $1/e^2$ widths of $\sim$20 ns. This set-up was particularly well suited for aligning the heterodyne beat note since both the LO and diffracted beams had good spatial profiles. A disadvantage of this configuration was the challenge it posed for the detection of the echo signal at the tail end of the second excitation pulse, due to the background light from the increased pulse width. As a result, we operated the downstream AOM in the Raman-Nath regime with tightly-focused beams to produce pulse widths of 8 ns. Here, the Raman-Nath regime is loosely defined to refer to an experimental configuration in which the diffraction angle is smaller than the divergence angle. However, this configuration severely distorted the spatial profile of the LO (by creating a hole at its center). Since the divergence angle of the focused beam was larger than the diffraction angle, a beat note was present even when the excitation pulses were turned off. Therefore, the last iteration of the alignment involved operating the downstream AOM in an intermediate regime

to generate pulse widths of ∼12 ns. The echo data presented in this work was taken under these conditions, as well as in the Bragg regime.

6.2 RF network

The two AOMs are operated by a phase-locked voltage-controlled 250-MHz oscillator slaved to a 10-MHz Rb clock with an ADEV of 5×10^{-13} at 5,000 seconds [47]. The 10-MHz signal also slaves the time base of the delay generator that controls the gating pulse of the upstream AOM and the two excitation pulses of the downstream AOM. Under these conditions, the leading edges of the pulses can be set to a precision of 1 ps. The AOMs are controlled by an RF network consisting of TTL switches with an extinction ratio of 80 dB, power splitters, mixers, and RF isolators, as shown in Fig. 6.4. The temporal sequence of key pulses from the RF network is shown in Fig. 6.5.

To improve the intensity stability of the RF pulses, we introduced a simple feedback loop [90] into the RF network shown in Fig. 6.4. The 250-MHz phase-locked oscillator output is mixed down with itself in a reference arm and low-pass filtered to generate a DC signal. This DC signal is integrated and added to a stable reference voltage, which is then low-pass filtered and used to regulate the amplitude of a mixer that controls the RF intensity in both the reference arm and the experiment. A schematic of this feedback loop and the adder circuit containing the integrator are

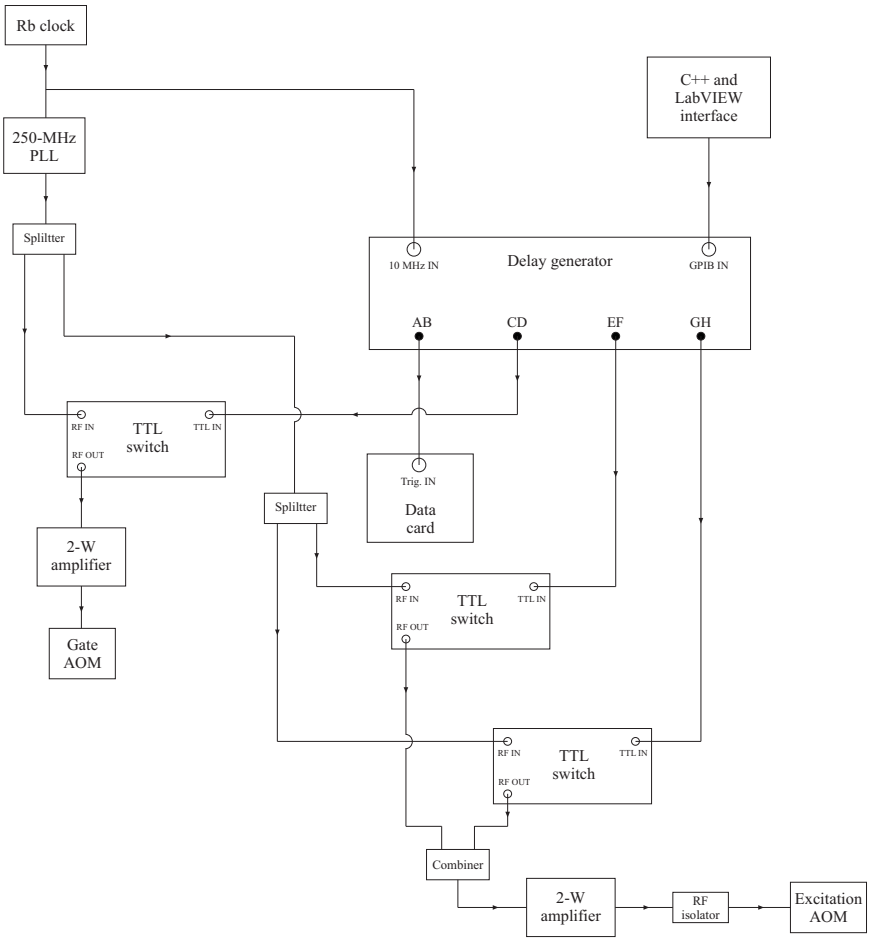

Figure 6.4: A 250-MHz oscillator (PLL) is phase locked to a 10-MHz signal from a Rb clock. The Rb clock also slaves the time base of a delay generator. The RF from the 250-MHz oscillator drives the TTL switches that control the upstream and downstream AOMs. These switches are controlled by the CD, EF, and GH pulses from the delay generator. A second delay generator (not shown) that is triggered by the delay generator in the figure is used to produce the gate pulse to isolate the echo signal from the excitation pulses. The AB output of the delay generator triggers the data card that acquires the echo signal. The pulsed outputs of the TTL switches are amplified and sent to the AOMs.

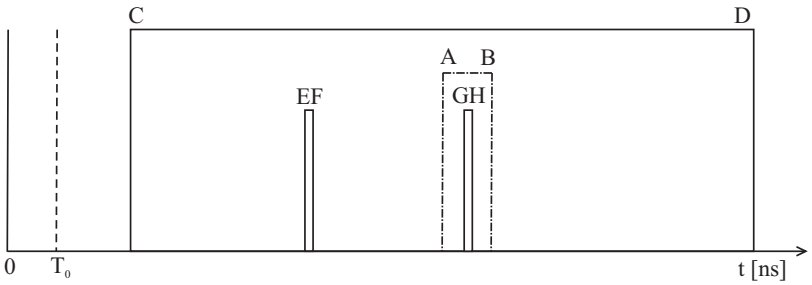

Figure 6.5: Temporal sequence of important control pulses. T_0 represents the onset of internal triggering of the delay generator. CD is the control pulse for the upstream AOM. EF and GH are the control pulses for the downstream AOM. AB is the gate pulse that triggers the data card approximately 100 ns before the occurrence of the echo pulse.

shown in Fig. 6.6.

Fig. 6.7(a) shows the ADEV of the RF intensity associated with the 250-MHz phase-locked oscillator without the feedback loop. To obtain these measurements, the RF oscillator was mixed with itself to produce a DC voltage that was monitored. The ADEV plot shows a floor of $\sim 2 \times 10^{-6}$ at an averaging time of 20 s. The ADEV plot of the amplified RF is slightly noisier, with an ADEV floor value of $\sim 3 \times 10^{-6}$ at an averaging time of 15 s. When the feedback loop is engaged, the ADEV plot in Fig. 6.7(c) shows a floor value of 2.5×10^{-6} at a significantly extended averaging time of just over 100 s, which is longer than the typical time required to record a single exponential decay of the photon echo intensity. Therefore, this feedback loop was retained when the lifetime data was recorded.

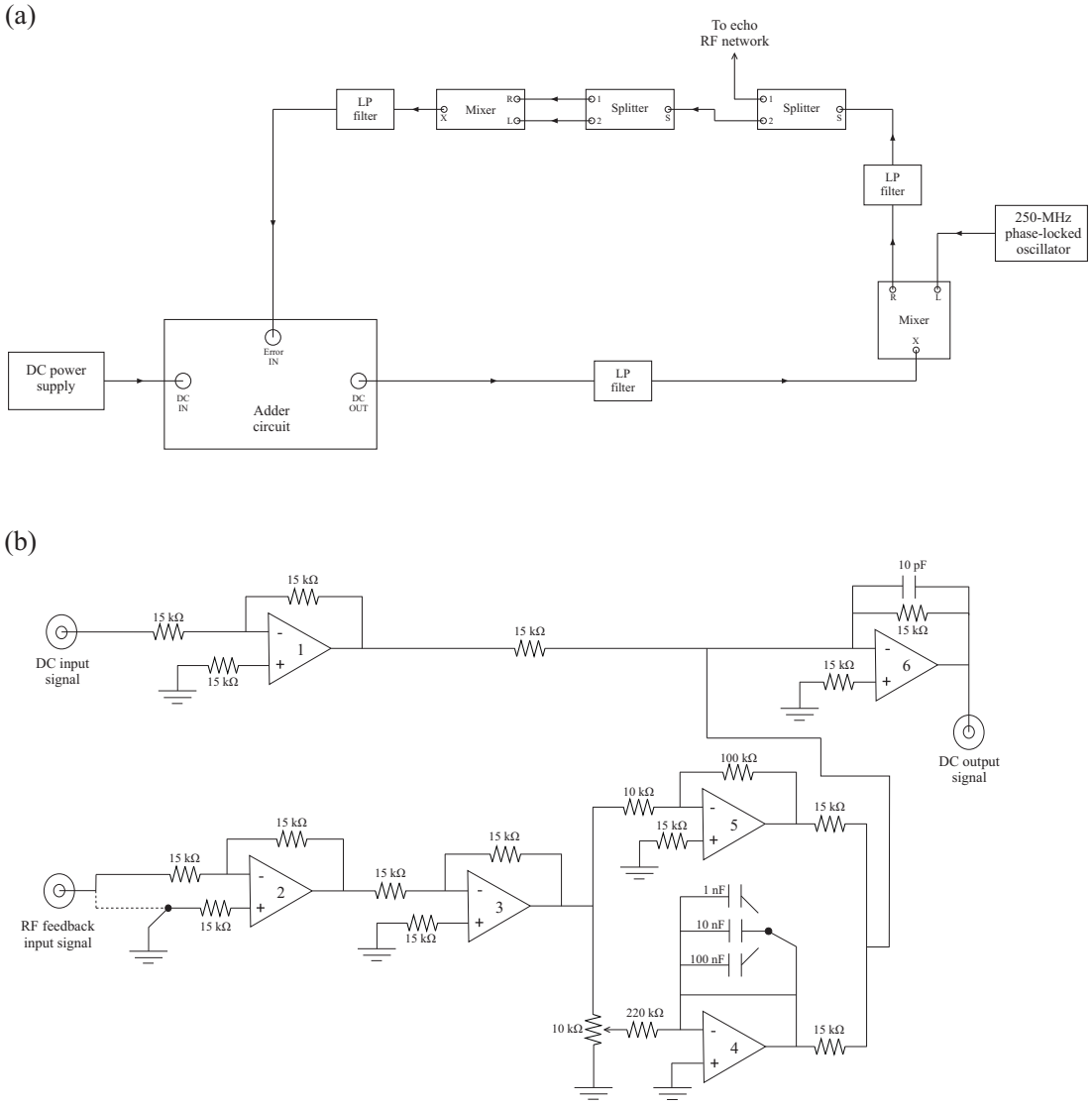

Figure 6.6: (a) Feedback loop used to stabilize the RF intensity of the network shown in Fig. 6.4. (b) Details of the adder circuit with an integrator that is part of the feedback loop.

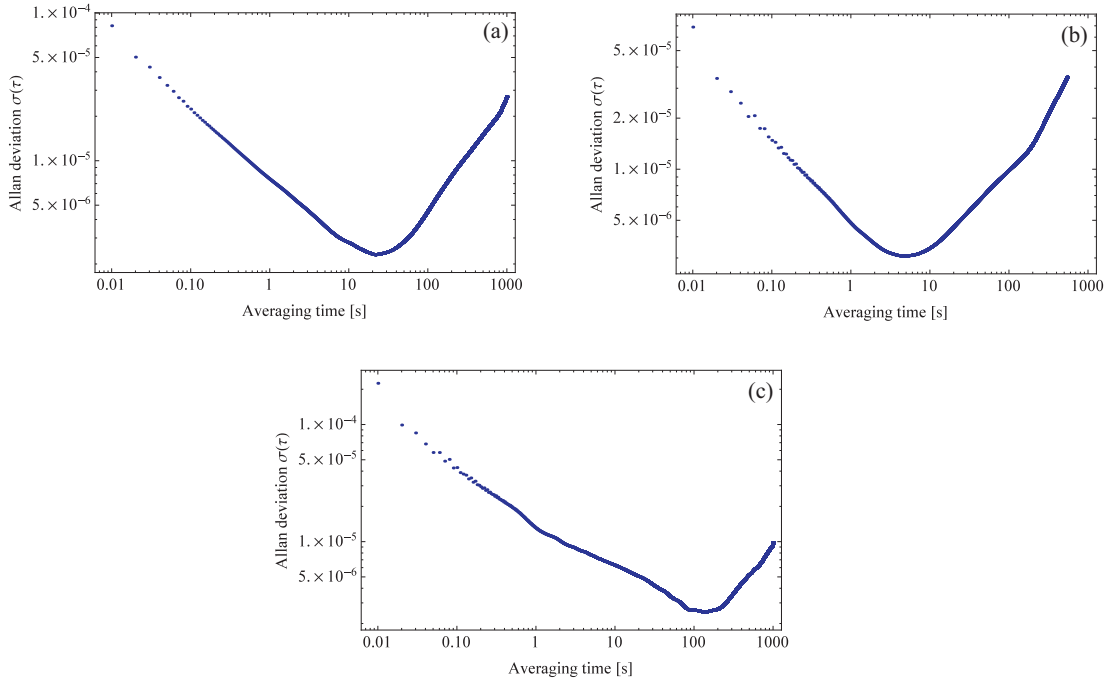

Figure 6.7: (a) ADEV of RF from 250-MHz PLL before amplifiers (no feedback circuit). (b) ADEV of RF from 250-MHz PLL after amplifiers (no feedback circuit). (c) ADEV of RF from 250-MHz PLL with feedback circuit (after amplifiers).

The excitation pulses are generated by varying the amplitude and width settings of the pulse generator to optimize the echo amplitude. The protocol to measure the echo signal involves temporally overlapping two identical excitation pulses, identifying the minimum value of T (defined as the time separation between the leading edges of the RF excitation pulses) at which the echo signal can be recorded without interference from the tail of the second pulse, and then adjusting the excitation pulse amplitude and widths to maximize the signal without consideration of pulse areas. Subsequently, the time delay T between the leading edges of the excitation pulses are randomly selected between the minimum value and the maximum value at which the signal size is comparable to the background.

6.3 Data acquisition

The echo signal is detected by a data card with an acquisition rate of 1 GS/s. The card is triggered by the pulse generator 100 ns before the onset of the echo whereupon it acquires 256 points (256 ns) before re-arming for the next trigger. The card can be configured to operate at repetition rates up to 1 MHz. The time base of the data card is also slaved to the Rb clock. A `C++` program is designed to average sequential acquisitions and can be run via an input variable from a LabVIEW interface specifying the number of averages and an output variable array for the averaged signal. The quad core xeon processor and high throughput PCIe interface to the card allow for

continuous real time averaging. For each fixed value of the delay time T between the excitation pulses that is set by a LabVIEW interface, this `C++` program is called to acquire and average repetitions ranging in number from 1 to 1 million.

Fig. 6.8(a) shows the heterodyne signal (averaged 50,000 times) recorded by the balanced detector in the form of a 250-MHz beat note. A similarly-averaged background is obtained by turning off the first excitation pulse, as shown in Fig. 6.8(b). These averaged output files from the `C++` program are saved to disk by LabVIEW. A Mathematica program reads all the averaged files within that output folder and populates arrays for the excitation and background pulses, respectively. To generate the echo intensity, the Mathematica program subtracts the background from the signal trace, as shown in Fig. 6.8(c). This trace shows a residual amplitude for the second pulse, since the background subtraction is imperfect. The Mathematica program then squares and integrates the background-subtracted signal over a window centered around the 50-ns envelope of the echo signal, as shown in Fig. 6.8(d). The peak intensity of the echo signal is used in Chapter 7 to identify the optimal conditions for data acquisition. The integrated signal, which is proportional to the energy emitted by the sample, is used in the lifetime measurements presented in Chapter 7.

Under optimal operating conditions, a decay of the echo signal is recorded by varying the pulse separation T in randomized increments of 1 ns over 300 discrete values, and acquiring 50,000 repetitions for each of these points. The decay time

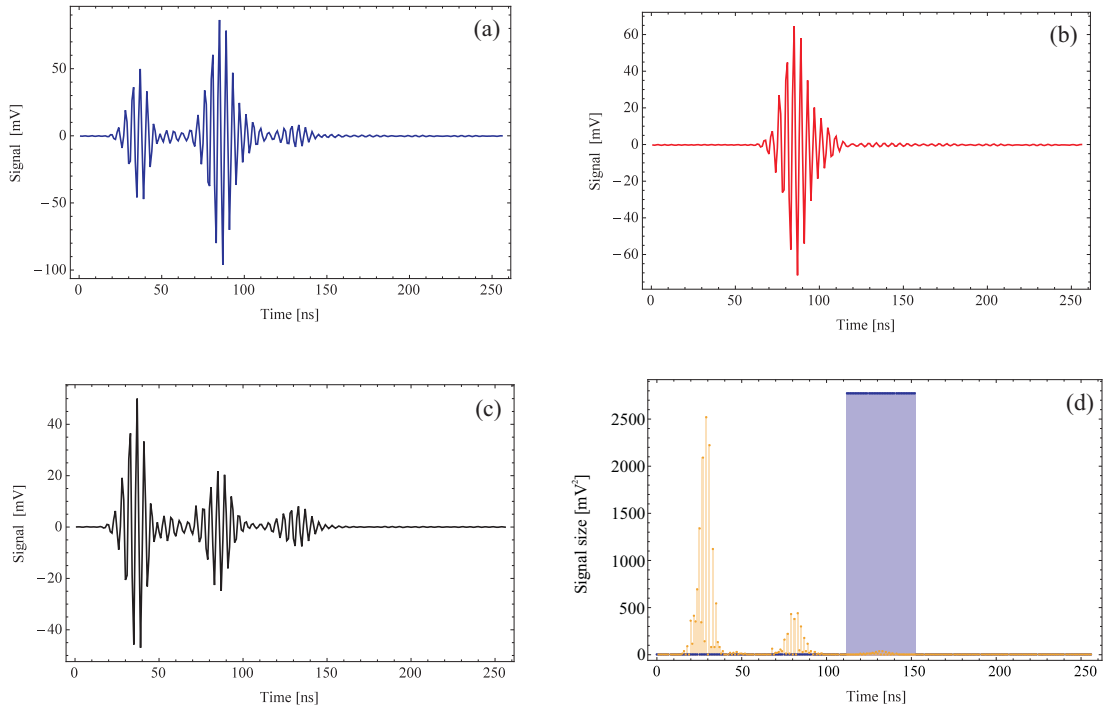

Figure 6.8: (a) Averaged heterodyne signal containing the two excitation pulses and echo recorded at $T = 46$ ns. (b) Background trace consisting of only the second excitation pulse. (c) Background-subtracted signal obtained by subtracting the traces shown in parts (a) and (b). (d) Square of the background-subtracted echo signal showing the integration window of the Mathematica program.

constant is obtained on the basis of an exponential fit to the echo signal. For such a 300-point data set, each signal and background trace is acquired in 50 ms, and the pulse generator delays are configured via a GPIB interface in 60 ms between each acquisition. This results in an acquisition time of 220 ms per data point, and a total time of 66 seconds for the entire data set.

7 Photon echo: results and discussion

7.1 Characterization of the echo intensity

We now discuss the results of the atomic lifetime measurement, along with studies of the signal strength and supporting data relating to investigations of technical limitations [21]. Fig. 7.1 shows the envelope of the echo recorded with heterodyne detection [part (a)] and PMT detection [part (b)]. The heterodyne signal has been squared so that both traces have dimensions of intensity. The acquisition rate of the data card (1-ns sampling time) ensures that both traces have the same number of points over the echo envelope. Here, the heterodyne signal consists of a 250-MHz beat note. Since the sampling rate is 1 GHz, the Nyquist frequency of 500 MHz is twice the signal frequency (and the same as the frequency of the squared heterodyne signal), and so the measured value represents the signal accurately. In contrast, the analog signal from the PMT can be fit to a Gaussian envelope to extract the radiated energy and the width of the Doppler-broadened profile excited by the pulse bandwidth, as described in Chapter 5. The $1/e^2$ fit value of 18.6 ns is consistent with the

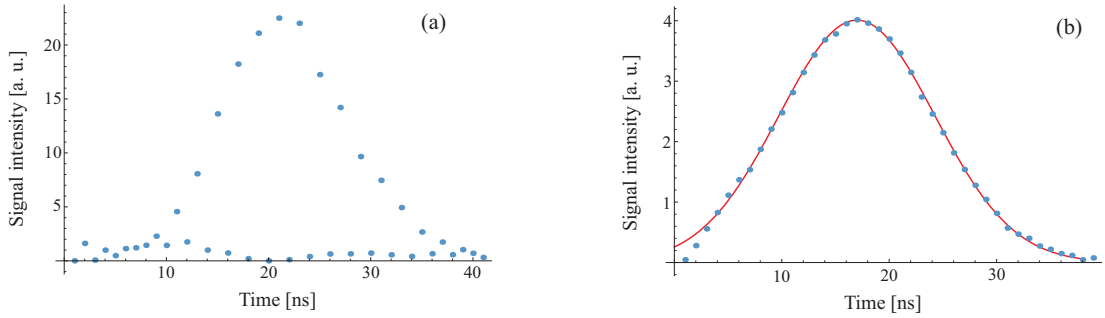

Figure 7.1: Envelope of echo signal in heterodyne detection (a) and PMT detection (b). The Gaussian fit in part (b) gives a $1/e$ width of (18.6 ± 0.1) ns. We note that the two traces were obtained with different excitation pulse widths and cannot be directly compared.

width of the signal predicted by the square of Eq. (5.3).

Prior to obtaining the lifetime measurements, the echo intensity was investigated as a function of the excitation pulse parameters, the overall cw power in the excitation beam, and the cell temperature. Fig. 7.2 shows the peak echo intensity obtained from the echo envelope, as shown in Fig. 6.8(d). This data was recorded at an optimized cell temperature of $\sim$40°C. The echo intensity was also optimized by regulating the optical power in the excitation beam to a cw value of $\sim$100 mW. In Figs. 7.2(a) and (b), the peak echo intensity is plotted as a function of the excitation pulse intensities. For each of these plots, the echo intensity was first optimized, after which one of the pulse intensities was varied, while the other was fixed at the optimal setting. The peak intensity of each excitation pulse was determined by blocking the LO and fitting to

the shape of the pulse envelope recorded by the photodiode. Likewise, in Figs. 7.2(c) and (d), the peak echo intensity is plotted as a function of the excitation pulse widths. Once again, the echo intensity was first optimized, after which one of the pulse widths was varied, while the other was fixed at the optimal setting. The pulse widths were determined by blocking the LO and fitting to the pulse envelope. These plots show that the peak echo intensity is obtained for nearly the same excitation pulse intensity for both pulses. With both pulses set to maximize the echo, it was possible to reduce the intensity of each pulse by adding attenuators to the RF network. This results in a decrease in the echo intensity, as observed in Figs. 7.2(a) and (b). To increase the pulse intensity to obtain the maximum echo intensity, it was necessary to increase the pulse width. The decrease in the echo intensity beyond the maximum in both Figs. 7.2(a) and (b) is therefore attributed to the reduced bandwidth of excitation. The pulse width dependence is explicitly studied in Figs. 7.2(c) and (d). Here, the peak echo intensity was obtained for the shortest (12 ns) excitation pulses, and decreased when the pulse widths became larger. This trend is also consistent with the expected decrease in signal strength due to the reduced bandwidth of excitation. We note that there is a significant reduction in the slopes of the trends in Figs. 7.2(c) and (d) for pulse widths of $\sim$18 ns. We attribute this effect to interference between pulse tails, as discussed later in this chapter.

Fig. 7.3 shows the peak echo intensity as a function of the cw optical power of

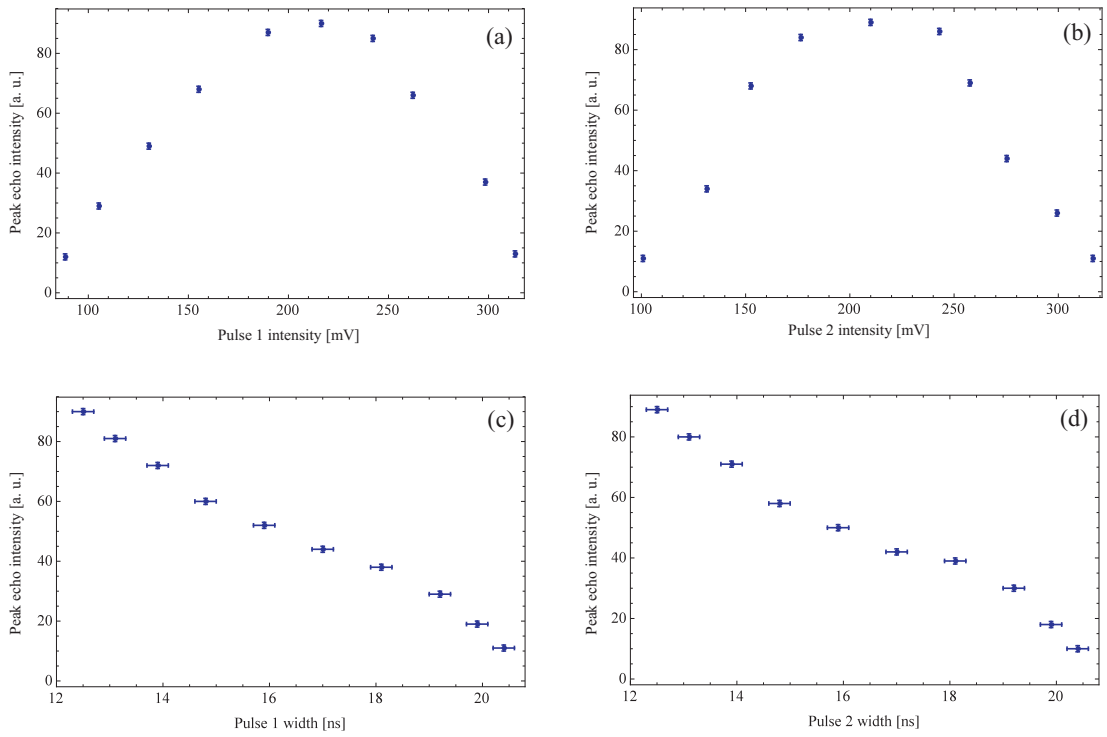

Figure 7.2: Peak echo intensity as a function of pulse intensity and pulse width. (a) Peak echo intensity vs. pulse 1 intensity. (b) Peak echo intensity vs. pulse 2 intensity. (c) Peak echo intensity vs. pulse 1 width. (d) Peak echo intensity vs. pulse 2 width.

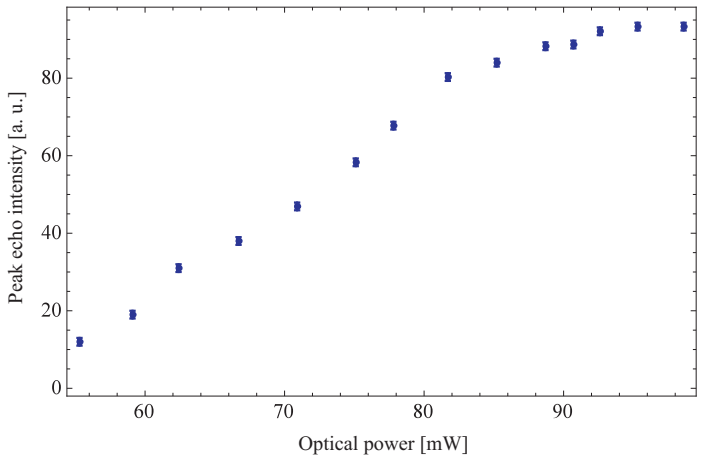

Figure 7.3: Peak echo intensity as a function of cw optical power of the excitation beam.

the excitation beam. Here, the excitation pulse widths and intensities are set to their optimal values, as shown previously in Fig. 7.2, and the cell temperature is maintained at 40°C. As noted in Chapter 6, the maximum power of 100 mW and the optimum pulse widths of 12 ns result in excitation pulse areas of $\sim 15\pi$. According to the area theorem [86, 26], excitation pulses with certain optimized areas can be expected to propagate through the cell without attenuation for a given optical depth. However, our studies show that the echo intensity exhibits a single well-defined maximum for a particular optical depth, suggesting that pulse absorption has a dominant effect on the echo intensity. As a result, we attribute the plateau in Fig. 7.3 at a power of ~100 mW to the effect of saturating the optically-thick atomic sample.

Fig. 7.4 shows the peak echo intensity recorded by varying the cell temperature.

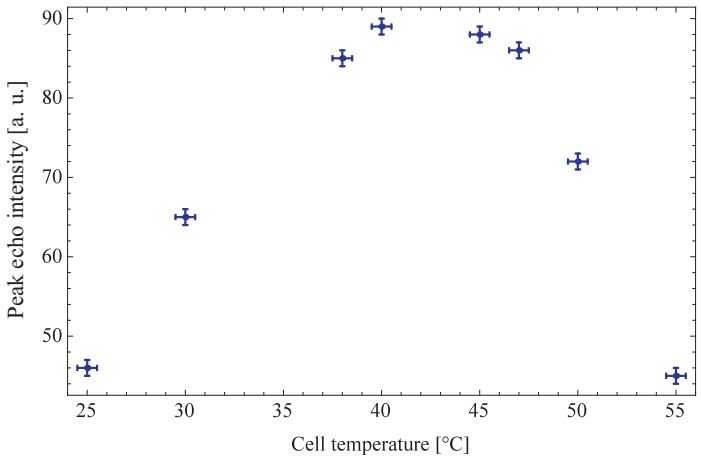

Figure 7.4: Peak echo intensity as a function of cell temperature.

Here, the pulse widths and intensities have been optimized for an input cw excitation beam power of ∼100 mW. The data shows that the increase in the echo intensity is proportional to the increase in density due to the cell temperature until pulse attenuation becomes dominant at a temperature of ∼40°C. This effect is strongly correlated with an increase in the optical depth. We now present lifetime measurements that were obtained under the optimized conditions identified through the investigations described in this section.

7.2 Lifetime measurements

Fig. 7.5(a) and (b) show the echo decay on a log and linear scale, along with linear and exponential fits, respectively. This data set, which consists of 300 points, each averaged 50,000 times, was obtained with heterodyne detection on a time scale

of $\sim$1 minute. The averaged signal shown in Fig. 6.8(d) was integrated over the echo envelope to obtain the echo intensity shown in Fig. 7.5. The integrated area under the echo envelope is proportional to the radiated energy, which is plotted as a function of $2T$. The exponential and linear fits extending over $\sim$4 lifetimes give consistent values for τ_1 within error bars. The measurement precision of 0.3% is adequate for obtaining accuracies comparable to the measurements in Table 5.1. For these conditions, the peak value of the echo signal corresponds to a power of 80 μW, based on the calibration of the heterodyne detector. The residuals in Fig. 7.5(c) and (d) show no trend, thereby suggesting that there are no significant systematic effects on the measurement time scale. In comparison, we find that the signal-to-noise ratio of exponential decays recorded with the PMT is considerably smaller due to the lower dynamic range compared to the heterodyne measurement. Other complicating factors associated with PMT detection include worse background subtraction compared to the heterodyne technique – an effect that arises because the PMT's response is affected by the preceding excitation pulses. As a result, we rely only on the heterodyne technique for the rest of the measurements discussed in this dissertation.

Fig. 7.6(a) shows a sequence of 217 lifetime measurements recorded over the course of several weeks over four runs using the same data acquisition protocol as in Fig. 7.5. Each point corresponds to an exponential decay recorded in 66 seconds, resulting in a total acquisition time of 4 hours. These data sets were selected because the

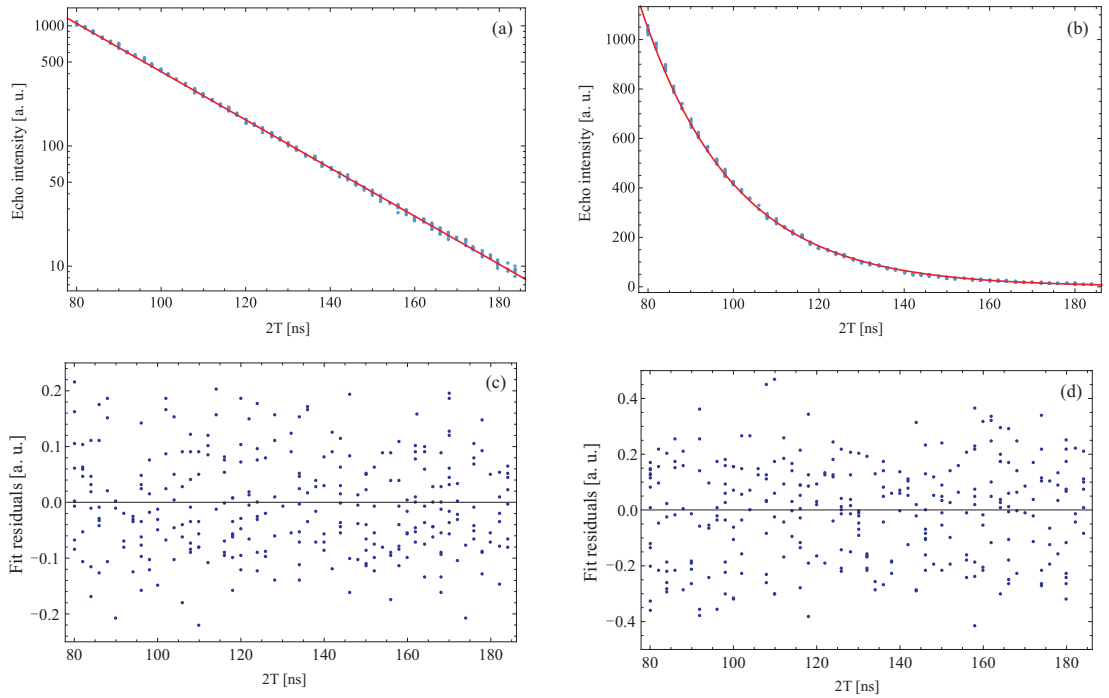

Figure 7.5: (a) Decay of the echo signal recorded with heterodyne detection displayed on a log scale. Here, the lifetime inferred from the slope of the linear fit on the basis of Eq. (5.5) is $\tau_1 = (26.12 \pm 0.08)$ ns, and the intercept is (1064 ± 1) a. u. (b) Same data as in part (a) displayed on a linear scale. Here, the parameters of the exponential fit function described by Eq. (5.5) are obtained from a fit of the form $Ae^{-t/\tau_1} + B$, where A = (1240 ± 10) a. u., $\tau_1 = (26.13 \pm 0.08)$ ns, and B = (12.2 ± 0.1) a. u. We note that the time origin for plots (a) and (b) is not $2T = 0$. (c) Corresponding residuals of the linear fit in part (a). (d) Corresponding residuals of the exponential fit in part (b).

variations in the lifetime value were smaller than the size of the error bars. Inspection of these data sets also indicated that the corresponding exponential decay curves showed no evidence for oscillations. Additionally, these measurements were carried out in a "double-blind" manner, in which the value of the lifetime was not only hidden, but also multiplied by a scale factor that was revealed only after the data was processed. Fig. 7.6(b) shows a histogram of the measurements from part (a) based on the parameters of the exponential fits. The mean value of these measurements is 26.09 ns, and the standard deviation of 0.09 ns corresponds to a statistical uncertainty of 0.3%. We note that the error bars of the exponential fits in Fig. 7.6(a) are comparable to this value.

We obtain a rigorous estimate of the uncertainty by computing the variances of the four individual runs in Fig. 7.6(a). For each run, the statistical uncertainty is taken to be the last point on the corresponding ADEV curve, as discussed further in the context of Fig. 7.7. The average values of the four runs shown in Fig. 7.6(a) and their corresponding statistical uncertainties based on the last point of the ADEV curves are (26.075 $\pm$ 0.003) ns, (26.101 $\pm$ 0.008) ns, (26.14 $\pm$ 0.01) ns, and (26.10 $\pm$ 0.03) ns, respectively, which result in an overall average of $\tau = 26.10$ ns. We calculate the standard variance of the four runs with respect to the overall average value to be 0.0007 ns^2. The average of the statistical variances of the four runs is 0.0003 ns^2. We then obtain a standard deviation of 0.03 ns from the square-root of the total variance,

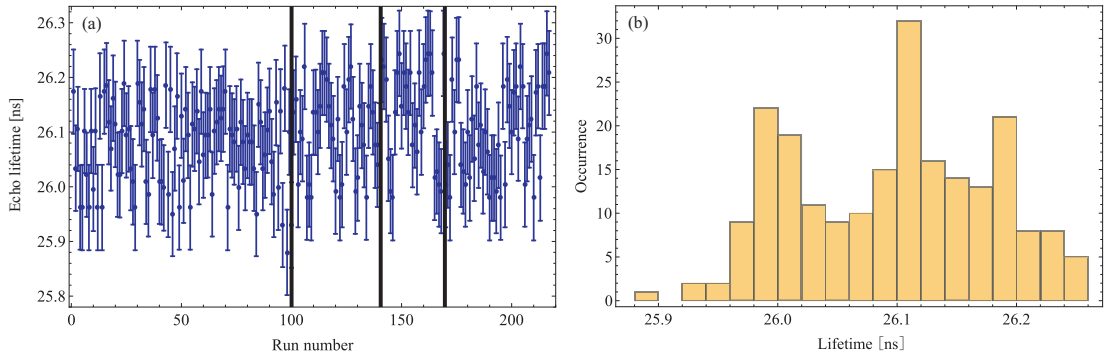

Figure 7.6: (a) Sequence of 217 lifetime measurements recorded in 4 hours, with τ_1 inferred from exponential fits. The vertical lines indicate the demarcation between four data runs in which data points were taken in an uninterrupted sequence. The typical size of the fit error bars is 0.3%. (b) A histogram of the data presented in part (a). The standard deviation of 0.35% is comparable to the fit error.

which represents the statistical error in the measurement. The final result of $\tau_1 = (26.10 \pm 0.03)$ ns (statistical uncertainty of 0.11%) is the best estimate of the lifetime value of our results, which omits the effects of variations and technical limitations. We also find that none of the experimental parameters that affect the signal – such as number density, pulse areas, magnetic fields, and polarization – produce variations in the lifetime values that are larger than this best estimate. Furthermore, our estimate of the statistical uncertainty is more conservative than the value given by the standard deviation of the mean of the 217 data points.

Fig. 7.7 shows the ADEV of the longest uninterrupted data run (the first 100 points) included in Fig. 7.6(a). This data has a floor value of 1.3×10^{-4} at a mea-

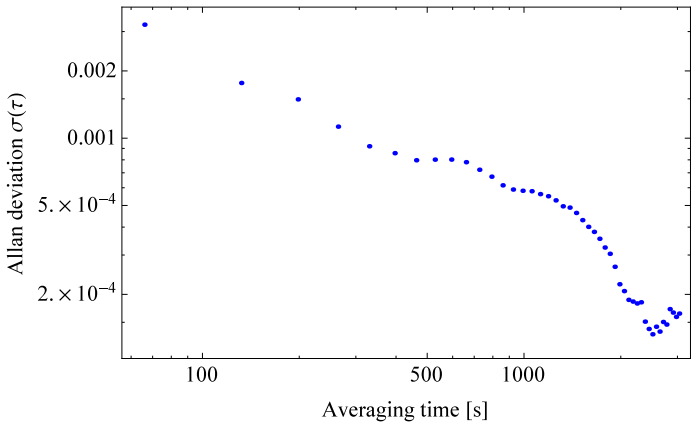

Figure 7.7: ADEV of the longest data run of 100 points from the data set in Fig. 7.6. The floor value is 1.3×10^{-4} at $\tau_{floor} \sim$ 2,500 s, and the last point is 1.6×10^{-4}.

surement time $\tau_{floor} \sim$ 4,000 s, and the last point is 1.6×10^{-4}. The ADEV floor value (0.013%) represents the best statistical uncertainty that can be achieved by the current configuration of the experiment. It is also evident that the approach to the ADEV floor value does not scale down as rapidly as $\tau^{-1/2}$ (where τ is the measurement time). At longer measurement times, the long-term variations begin to impact the stability of the measurement. The ADEV floor value also suggests that technical limitations need only be decreased by a factor of two to reduce the statistical precision below that of the best lifetime measurement (0.007%) [69]. This suggests the viability of the photon echo technique for obtaining the best lifetime measurements if the technical limitations that produce long-term variations can be understood and addressed.

The estimated collisional rate of 10 $s^{-1}atom^{-1}$ in the vapour cell shows that the

dominant systematic effect that can be anticipated is transit time broadening. We use the measured transit time broadening parameter of 4.1 μs/mm for ground-state coherences in a similar vapour cell experiment [91] to estimate the corrected value of the lifetime τ_{corr}. This broadening parameter is consistent with the model used in references [87, 92, 93]. The transit time $\tau_{transit}$ for the average beam diameter used in this work is estimated to be 5.1 μs $\pm$10%, with the uncertainty arising from our beam size measurements. Following reference [93] in the limit that $T << \tau_{transit}$, we obtain $1/\tau_1 = 1/\tau_{corr} + T/\tau_{transit}^2$. For an average value of $2T = 130$ ns, we obtain $\tau_{corr} = (26.10 \pm 0.03)$ ns, which represents a negligible correction [21]. This value for the $5^2P_{3/2}$ lifetime agrees at the level of 1σ with the most precise measurement for this transition (26.20 $\pm$ 0.09) ns [25], as indicated in Table 5.1, but it disagrees with the values reported in references [24, 70]. Furthermore, all these measurements disagree with the best theoretical calculations for this Rb transition [67, 68]. A more rigorous estimate of the transit time correction can be obtained by measuring the lifetime over a range of beam diameters.

Another factor that can potentially influence the lifetime measurement is laser phase noise, which produces a decoherence on a time scale τ_{phase}, so that $1/\tau_1 = 1/\tau_{corr} + T/\tau_{transit}^2 + 1/\tau_{phase}$. Although the short-term linewidth of seed lasers used in our work of $\sim$200 kHz on a time scale of 50 ms (coherence time of 5 μs) [2, 21] are small, it can only be estimated on the basis of a direct measurement. We now

explain the technical limitations that preclude studies of systematic effects.

7.3 Lifetime variations and checks

We now explain the technical limitations that preclude studies of systematic effects. Fig. 7.8 shows an example of a single data run of 100 consecutive lifetime measurements with no change in experimental conditions. It is evident that the lifetime values show significant variations that are larger than the size of the error bars and deviate by $\sim$0.5 ns from the measured value of 26.09 ns. Since these variations always resulted in lifetimes below the accepted value – an effect that could be caused by decoherence due to background light – we investigated a number of potential causes for this effect. First, we operated the downstream AOM in the Bragg regime so that the divergence angle of the focused laser beam is smaller than the diffraction angle, thereby reducing the amount of background light passing through the vapour cell. Under these conditions, the $1/e$ full width of the excitation pulses was 20 ns. However, this change in alignment did not reduce the lifetime variations. We also measured the background light with a power meter in both configurations of the downstream AOM over several hours and determined that the maximum power level was 5 μW. Since these photons are associated with the LO, which is 250 MHz up-shifted with respect to the excitation beam, we also varied the lock points of the ECDL across the Doppler profile. However, using different lock points did not change

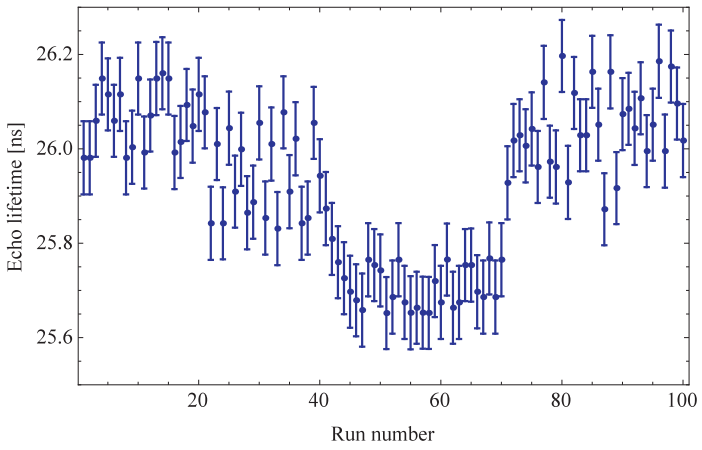

Figure 7.8: Data set showing 100 sequential measurements of the lifetime that exhibits a variation of ∼0.5 ns. This measurement was obtained on a time scale of ∼2 hours.

the 5-μW background level. The largest excitation probability due to the background photons over the duration of the experiment was 1.2 $\times 10^{-5}$, suggesting that the lifetime variations were not related to background light or to changes in alignment and detuning. Studies with a Fabry-Perot cavity with a resolution of 60 MHz ruled out any multi-mode behaviour of the laser. Any dependence on the heterodyne detection scheme – such as the effects of mirror vibrations – was ruled out by the observation of similar lifetime variations using a PMT to measure the echo intensity. Although estimates of the changes in the index of refraction of the AOM crystal due to thermal effects were negligible, we also carried out measurements with a thermally-stabilized AOM, and found that the lifetime variations persisted.

In addition, we verified that the lifetime variations shown in Fig. 7.8 were uncor-

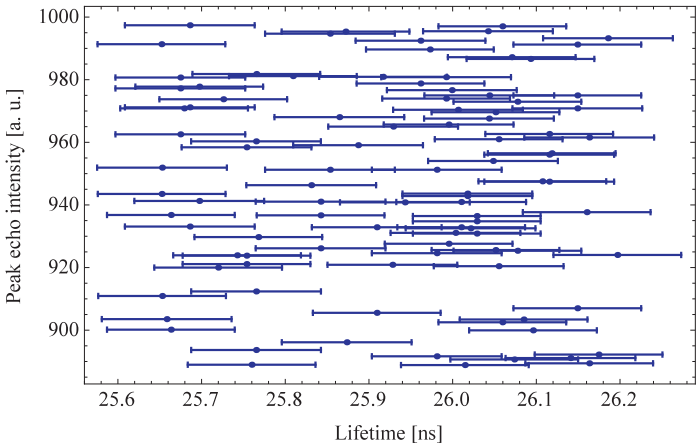

Figure 7.9: Peak echo intensity as a function of the lifetime for the data in Fig. 7.8.

related with the corresponding peak echo intensities of the exponential decays, as shown in Fig. 7.9.

We also investigated whether laser intensity variations could affect the lifetime variations. Fig. 7.10(a) shows the ADEV of the intensity of the ECDL shown in Fig. 6.1. The ADEV floor is $\sim 5 \times 10^{-6}$ at an averaging time of $\sim$10 s, which is consistent with the results in Chapter 4. Similarly, the ADEV floor value of $\sim 1.5 \times 10^{-5}$ in Fig. 7.10(b) for the TA occurs at the same averaging time as the ADEV plot shown in part (a) of the figure. These results are qualitatively consistent with references [88, 89], and suggest that the TA output has the same spectral characteristics as the ECDL, although it exhibits a higher level of intensity noise. The periodic ripples in both Figs. 7.10(a) and (b) are attributed to the effect of room lights. However, this effect is less pronounced in Fig. 7.10(a) since the photodiode was better shielded than

in part (b). Fig. 7.10(c) and (d) represent the same TA intensity stability data as in part (b), but recorded with lower and higher sampling rates, respectively. The sampling rates were varied to investigate intensity noise on the time scale of acquiring a single point on the exponential decay (50 ms), as well as the time required to record an entire decay curve (66 s). Based on these data sets, we infer that laser intensity noise is not responsible for the observed lifetime variations.

We further investigated the role of RF intensity stability on the lifetime variations. We established that the 250-MHz phase-locked oscillator shown in Fig. 6.4 did not produce intensity variations on the time scale of $\sim$10 s, and that this time scale could be significantly extended by a feedback loop, as shown in Fig. 6.7. We also operated the experiment with a commercially-available phase-locked signal generator tuned to 250 MHz, which was slaved to a Rb clock. Fig. 7.11 shows ADEV of the RF intensity from the commercial generator with and without amplification. It is evident from these graphs that the ADEV floor, which occurs at an averaging time of $\sim$10 s without the feedback loop, is in fact slightly worse than that of the oscillator used in Fig. 6.7. We also conclude that both oscillators did not affect the lifetime variations.

7.4 Theoretical model for understanding lifetime variations

Since our experimental investigations showed that the lifetime variations were not related to decoherence, we focused on the effect of imperfect background subtraction

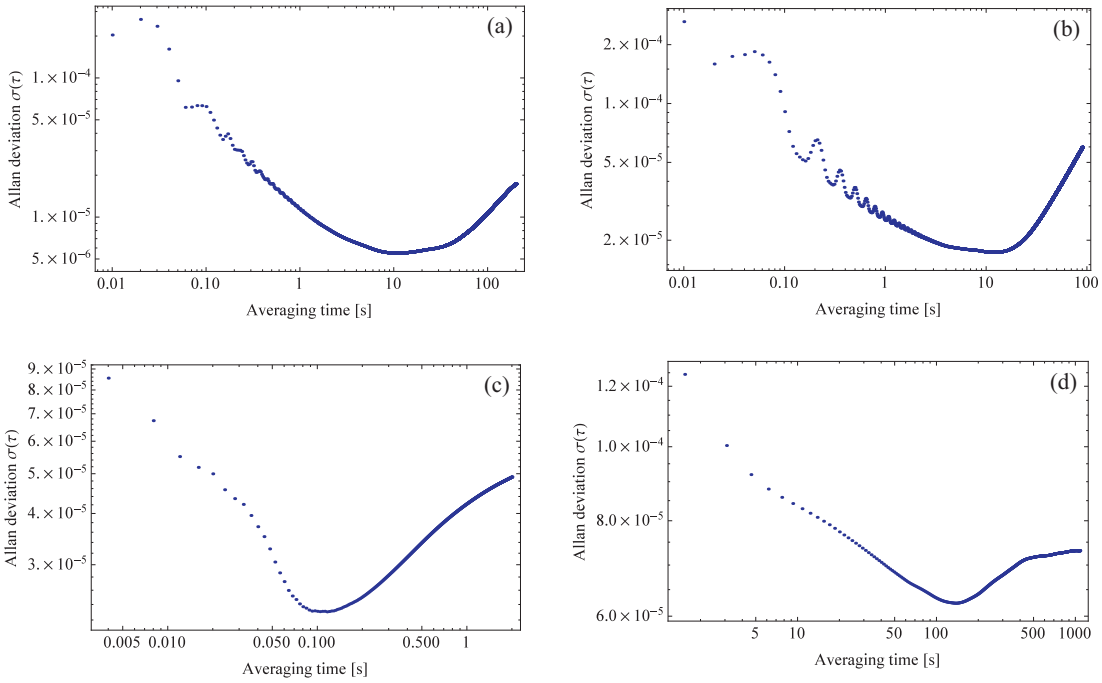

Figure 7.10: (a) ADEV of the intensity stability of the ECDL in Fig. 6.1, recorded at a sampling rate of 100 Hz. (b) ADEV of intensity stability of the downstream TA output in Fig. 6.1, recorded at a sampling rate of 100 Hz. (c) ADEV of the intensity stability of the same TA as in part (b) recorded on a short time scale, at a sampling rate of 1 kHz. (d) ADEV of the intensity stability of the same TA output as in part (b) recorded on a long time scale, at a sampling rate of 1 Hz. All these plots were recorded on different days. They serve as representative examples and should not be used to infer correlations.

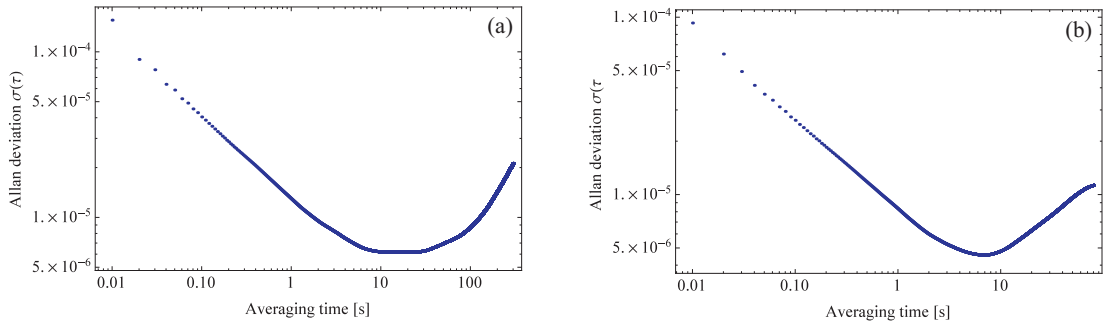

Figure 7.11: (a) ADEV of the RF intensity of a 250-MHz signal generated by a commercially-available signal generator, with a tuning range of several gigahertz. (b) ADEV of the same RF signal as in part (a) after amplification.

of the excitation pulse tails and their interference with the atomic response. This background is dependent on the value of the pulse separation T, as well as slowly varying optical phase variations due to beam pointing. Additionally, an interference effect is produced by the slow phase variation associated with the residual RF pulse and the ring-down of the AOM cavity following the application of short pulses, which results in a modulated optical background. We now present a simple model of this effect, which is highly relevant to short-pulse, time-domain spectroscopy using optical switches such as AOMs.

7.4.1 Heterodyne detection

For the heterodyne configuration, we model the total electric field at time t as a superposition of the electric fields of the two excitation pulses and the electric field

of the echo pulse, given by:

$$E_{tot}(t) = E_1(t) + E_2(t) + E_e(t). \tag{7.1}$$

Each pulse is defined by

$$E_i(t) = A_i(t)\cos(\omega t + \phi_i(t)), \tag{7.2}$$

where the $E_i(t)$ are the electric fields of the first excitation pulse, the second excitation pulse, and the echo, with $i = 1$, $i = 2$, and $i = e$, respectively. Each pulse is described by its amplitude $A_i(t)$ which reaches a maximum at $A_1(0)$, $A_2(T)$, and $A_e(2T)$. The phase $\phi_i(t)$ represents all contributions due to mirror vibrations, laser phase noise, and AOM phase drifts that might occur during the data acquisition time. Both $A_i(t)$ and $\phi_i(t)$ are assumed to be slowly varying functions over the time scale of the period of one RF cycle (4 ns).

At the time of the echo $t = 2T$, the total electric field is therefore

$$E_{tot}(2T) = E_1(2T) + E_2(2T) + E_e(2T). \tag{7.3}$$

Since the background signal is obtained by turning off the first excitation pulse, it is described by the electric field of the second excitation pulse $E_2(2T)$. As a result of the background-subtraction procedure, the electric field is given by

$$\begin{aligned} E_{bkg-sub}(2T) &= E_1(2T) + E_e(2T) \\ &= A_1(2T)\cos(\omega t + \phi_1(2T)) + A_e(2T)\cos(\omega t + \phi_e(2T))\,\mathrm{e}^{-T/\tau_1}, \end{aligned} \tag{7.4}$$

where the phenomenological decay rate $1/\tau_1$ is written explicitly as the decay of the amplitude following e^{-T/τ_1}. Because the data is processed by squaring the signal, the corresponding background-subtracted intensity is:

$$\begin{aligned} I(2T) =& A_1^2(2T)\cos^2(\omega t + \phi_1(2T)) + A_e^2(2T)\cos^2(\omega t + \phi(T))\,\mathrm{e}^{-2T/\tau_1} \\ &+ 2A_1(2T)A_e(2T)\,\mathrm{e}^{-T/\tau_1}\cos(\omega t + \phi_1(2T)\cos(\omega t + \phi_e(2T)). \end{aligned} \tag{7.5}$$

The heterodyne signal is obtained from the time average of Eq. (7.5) over the period of one RF cycle. The time average of the first two terms in Eq. (7.5) gives $\frac{1}{2}A_1^2(2T)$ and $\frac{1}{2}A_e^2(2T)\,\mathrm{e}^{-2T/\tau_1}$, respectively. Using the trigonometric identity $2\cos A\,cosB = \cos(A+B) + \cos(A-B)$, the time average of the last term in Eq. (7.5) becomes:

$$A_1(2T)A_e(2T)\,\mathrm{e}^{-T/\tau_1} \times \int_{0\,ns}^{4\,ns} \big[\cos(2\omega t + \phi_1(2T) + \phi_e(2T)) + \cos(\phi(2T))\big]\,dt, \tag{7.6}$$

where $\phi(2T) = \phi_1(2T) - \phi_e(2T)$. The integral of the first term, which is modulated at twice the optical frequency, gives zero; the second term, which is constant over the 4-ns period, only varies on longer time scales. Eq. (7.6) then becomes:

$$A_1(2T)A_e(2T)\,\mathrm{e}^{-T/\tau_1}\cos(\phi(2T)). \tag{7.7}$$

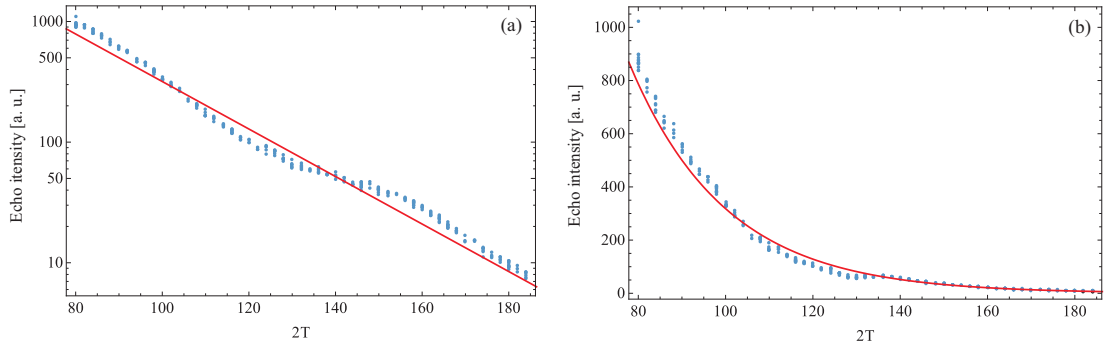

Figure 7.12: An example of the exponential decay of the echo signal plotted on a log scale (a) and on a linear scale (b). Here, the quality of the fits is severely impacted by the modulated background. The exponential fit gives $\tau_1 = (26.1 \pm 0.2)$ ns.

As a result, the intensity of the background-subtracted signal given in Eq. (7.5) becomes:

$$\bar{I}(2T) = \frac{1}{2}A_1^2(2T) + \frac{1}{2}A_e^2(2T)\,\mathrm{e}^{-2T/\tau_1} + A_1(2T)A_e(2T)\,\mathrm{e}^{-T/\tau_1}\cos(\phi(2T)). \qquad (7.8)$$

The result of Eq. (7.8) shows that the decay intensity of the echo signal as a function of time is modulated by a slowly varying background $\cos(\phi(2T))$ which decays as e^{-T/τ_1}, does not subtract out, and is the likely cause for the lifetime deviations.

We now show representative data that supports the conclusions of our theoretical model. Fig. 7.12 shows an example of an exponential decay obtained with heterodyne detection in which the effects of the modulated background can be seen to significantly affect the quality of the exponential fit.

Fig. 7.13 shows expanded plots of the DC pulses from the pulse generator, the RF drive pulses that control the AOMs, and an optical pulse used for excitation. The pulse tails and AOM cavity ring-down effects including a ∼20-MHz beat note at the tail of the optical pulse offer additional supporting evidence for the time-dependent and T-dependent modulated background predicted by the model.

7.4.2 PMT detection

A similar model for Eq. (7.3) for PMT detection shows that the background-subtracted signal is even more complicated. This is because intensity detection requires the squaring of the electric fields before background subtraction. To demonstrate this effect, we first find the intensity detected by the PMT by taking the square of Eq. (7.3):

$$I(2T) = [E_1(2T) + E_2(2T) + E_e(2T)]^2. \tag{7.9}$$

After background subtraction, the intensity becomes:

$$\begin{aligned} I_{bg-sub}(2T) = {} & E_2^2(2T) + E_e^2(2T) \\ & + 2E_1(2T)E_2(2T) + 2E_1(2T)E_e(2T) + 2E_2(2T)E_e(2T). \end{aligned} \tag{7.10}$$

Substituting Eq. (7.2) into Eq. (7.10) gives:

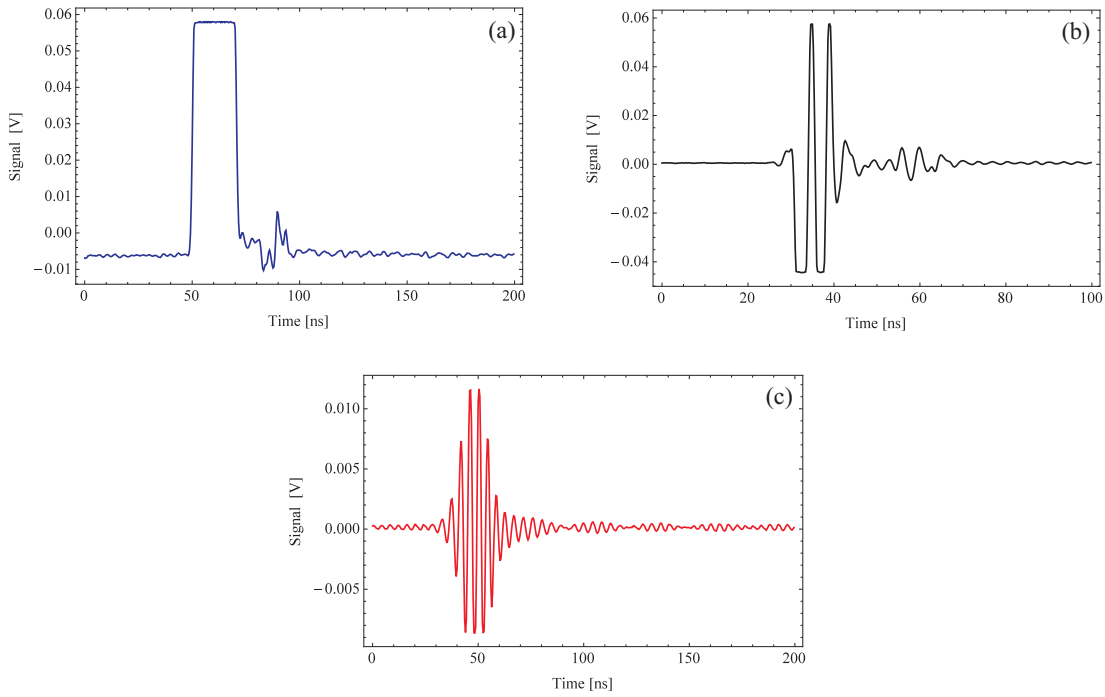

Figure 7.13: (a) DC pulse from delay generator showing distortions in the tail. (b) An example of a magnified RF pulse showing RF leakage in the tail. (c) Magnified optical pulse detected as a heterodyne beat note showing ring-down effects of the AOM cavity and beat frequency between the 250-MHz drive frequency and the cavity resonance frequency.

$$
\begin{aligned}
I_{bg-sub}(2T) = {} & A_2^2(2T)\cos^2(\omega t + \phi_2(2T)) + A_e^2(2T)\,\mathrm{e}^{-2T/\tau_1}\cos^2(\omega t + \phi_e(2T)) \\
& + 2E_1(2T)E_2(2T)\cos(\omega t + \phi_1(2T))\cos(\omega t + \phi_2(2T)) \\
& + 2E_1(2T)E_e(2T)\cos(\omega t + \phi_1(2T))\cos(\omega t + \phi_e(2T))\,\mathrm{e}^{-T/\tau_1} \\
& + 2E_2(2T)E_e(2T)\cos(\omega t + \phi_2(2T))\cos(\omega t + \phi_e(2T))\,\mathrm{e}^{-T/\tau_1}\,.
\end{aligned}
\tag{7.11}
$$

Averaging over the period of one RF cycle gives $\frac{1}{2}A_2^2(2T)$ and $\frac{1}{2}A_e^2(2T)\,\mathrm{e}^{-2T/\tau_1}$ for the first two terms in Eq. (7.11), respectively. Using once again the trigonometric identity $2\cos A\, cos B = \cos(A+B) + \cos(A-B)$, the respective time averages of the last terms give:

$$
\begin{aligned}
& A_1(2T)A_2(2T) \times \int_{0\,ns}^{4\,ns} \big[\cos(2\omega t + \phi_1(2T) + \phi_2(2T)) + \cos(\phi'(2T))\big]\,dt \\
& + A_1(2T)A_e(2T)\,\mathrm{e}^{-T/\tau_1} \times \int_{0\,ns}^{4\,ns} \big[\cos(2\omega t + \phi_1(2T) + \phi_e(2T)) + \cos(\phi(2T))\big]\,dt \\
& + A_2(2T)A_e(2T)\,\mathrm{e}^{-T/\tau_1} \times \int_{0\,ns}^{4\,ns} \big[\cos(2\omega t + \phi_2(2T) + \phi_e(2T)) + \cos(\phi''(2T))\big]\,dt.
\end{aligned}
\tag{7.12}
$$

where $\phi'(2T) = \phi_1(2T) - \phi_2(2T)$, $\phi(2T) = \phi_1(2T) - \phi_e(2T)$ (as defined previously in the heterodyne treatment), and $\phi''(2T) = \phi_2(2T) - \phi_e(2T)$. Following the same arguments for Eqs. (7.6) and (7.7) as in the heterodyne treatment, the second terms in each of the integrals of Eq. (7.12) are constant over the 4-ns integration period. As a result, Eq. (7.12) becomes:

$$
\begin{aligned}
&A_1(2T)A_2(2T)\cos(\phi'(2T)) \\
&+ A_1(2T)A_e(2T)\,\mathrm{e}^{-T/\tau_1}\cos(\phi(2T)) \\
&+ A_2(2T)A_e(2T)\,\mathrm{e}^{-T/\tau_1}\cos(\phi''(2T)).
\end{aligned}
\tag{7.13}
$$

It therefore follows that the intensity of the background-subtracted signal given in Eq. (7.10) becomes:

$$
\begin{aligned}
\bar{I}(2T) = \frac{1}{2}A_2^2(2T) + \frac{1}{2}A_e^2(2T)\,\mathrm{e}^{-2T/\tau_1} + A_1(2T)A_2(2T)\cos(\phi'(2T)) \\
+ A_1(2T)A_e(2T)\,\mathrm{e}^{-T/\tau_1}\cos(\phi(2T)) + A_2(2T)A_e(2T)\,\mathrm{e}^{-T/\tau_1}\cos(\phi''(2T)).
\end{aligned}
\tag{7.14}
$$

It is evident from Eq. (7.14) that PMT detection is far less effective for adequately subtracting the background than heterodyne detection, as indicated by the additional modulating terms. The results of this model are well supported by the experiment, since we consistently find that background subtraction works better for heterodyne detection. This aspect of the detection was further emphasized by studies of the background subtraction carried out without the presence of the Rb cell.

Other indirect evidence that supports this model is the behaviour of the background offset parameter of the exponential fits, which represents an average variation in the background over the entire exponential decay. This fit parameter shows correlation with the lifetime variations for PMT detection, but is weakly correlated for

heterodyne detection. We now show representative data sets in which the variations in the lifetime values were larger than the size of the error bars. Fig. 7.14(a) shows 100 sequential lifetime measurements acquired using heterodyne detection. Fig. 7.14(b) shows that the corresponding offset parameters B of the exponential fits [refer to Fig. 7.5] are uncorrelated with the lifetime values. Fig. 7.14(c) shows comparative sequential lifetime measurements as in part (a) acquired using PMT detection. For this data, the offset parameter shows significant correlation with the lifetime values, as shown in Fig. 7.14(d).

The effects described by the model are further emphasized by a plot of the fractional uncertainty of the lifetime recorded by varying the number of repetitions for each point on the exponential decay, and the number of points on the decay curve, as shown in Fig. 7.15(a) and (b), respectively. Here, the data was obtained with heterodyne detection because it provided greater sensitivity than PMT detection. In both these figures, the fractional uncertainty with respect to the lifetime value is determined from the fit error of a single exponential decay. In Fig. 7.15(a), the number of points on the exponential decay was fixed at 300, and the averaging time varied from 1 ms for 1,000 repetitions to 1,000 ms for 1,000,000 repetitions. The reduction in the fractional uncertainty on short times scales exhibits an inverse square-root dependence (fit line) until the optimum number of repetitions (50,000) is reached. The turning point at 50 ms indicates the contributions of long-term effects due to optical

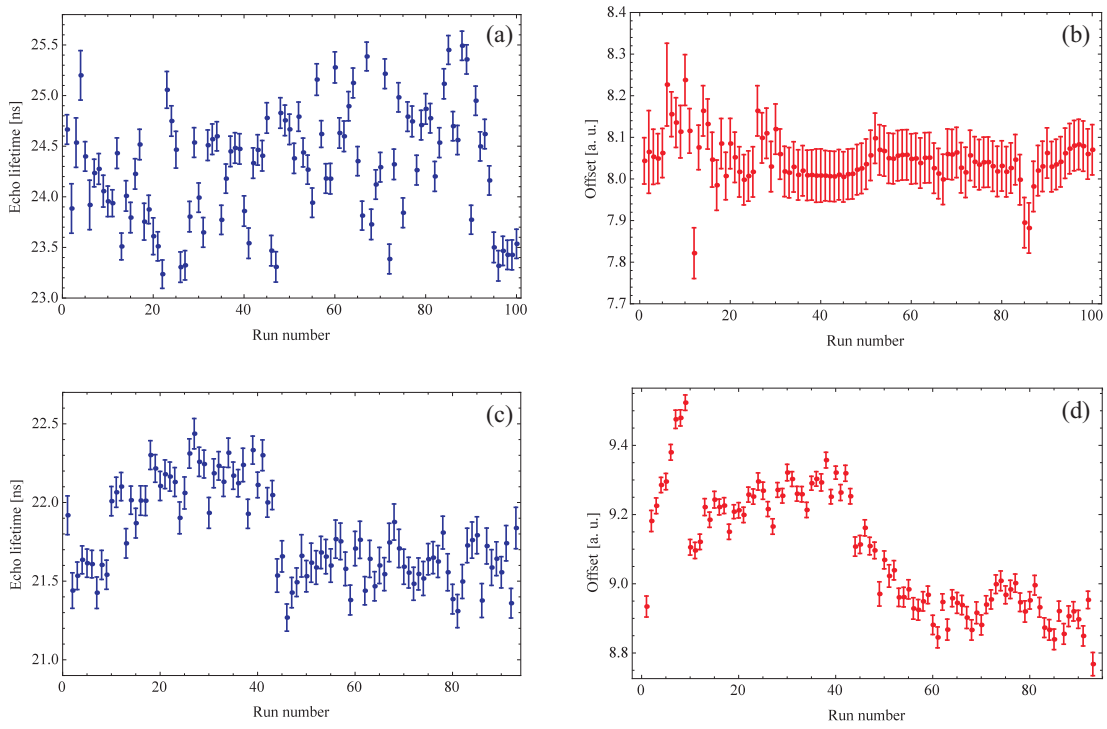

Figure 7.14: Examples of data sets in which the lifetime variations are larger than the size of the error bars. (a) 100 sequential lifetime measurements acquired with heterodyne detection. (b) Offset parameters of exponential fits corresponding to part (a) as a function of run number. (c) 100 sequential lifetime measurements acquired with PMT detection. (d) Correlations between offset parameters of exponential fits corresponding to part (c) as a function of run number.

and RF phase variations. The increase in the fractional uncertainty is dominated by the long time scale noise (up to 1 second) represented by the modulated phase term in Eq. (7.8). The fractional uncertainty in Fig. 7.15(b), which was recorded by incrementing the number of points on the decay curve from 100 to 1,000, shows that the optimum number of points corresponds to 300. Here, the number of repetitions for each point on the exponential decay was fixed at 50,000 so that the acquisition time varied from 22 s to 220 s. It is evident that the long-term phase variations continue to dominate on time scales extending to several minutes. The results from Fig. 7.15 for the best fractional uncertainty on the lifetime values from exponential fits (0.28%) are consistent with our best estimate for the statistical error of a single exponential fit (0.3%).

Our studies show that if the long-term phase variations are addressed, the inverse square-root dependence in Fig. 7.15(a) will result in a statistical precision of 0.03% for a single exponential decay with 1 million repetitions (corresponding to a total acquisition time of 636 s for 300 points on the exponential curve). Such conditions would allow rigorous investigations of possible systematic effects due to excitation pulse parameters, polarization, magnetic fields, and cell density.

Although the model we have presented is simple, it provides insight into how the lifetime variations can be avoided in a future experiment, as outlined in Fig. 7.16. Here, we envision a heterodyne beat note that can be generated in real time in a

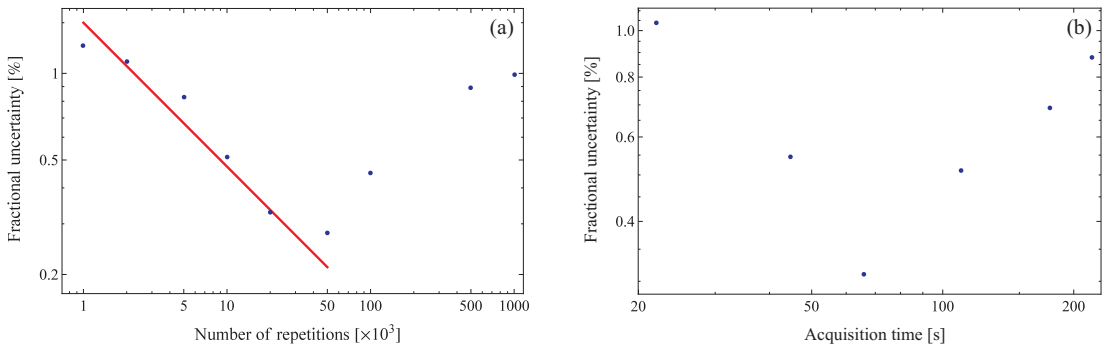

Figure 7.15: (a) Fractional uncertainty in the lifetime values from single exponential fits recorded with heterodyne detection as a function of the number of repetitions (averaging time) for each point on the exponential decay. The averaging time varied from 1 ms for 1,000 repetitions to 1,000 ms for 1,000,000 repetitions. The linear fit represents an inverse square-root dependence. (b) Fractional uncertainty in the lifetime values from single exponential fits recorded with heterodyne detection as a function of the number of points on each exponential decay. For all data points on this plot, the number of repetitions was fixed at 50,000. The acquisition time varied from 22 s for 100 points to 220 s for 1,000 points. Both data sets exhibit minima corresponding to the optimal operating conditions for the experiment, namely 50,000 acquisitions with 300 points on the exponential decay.

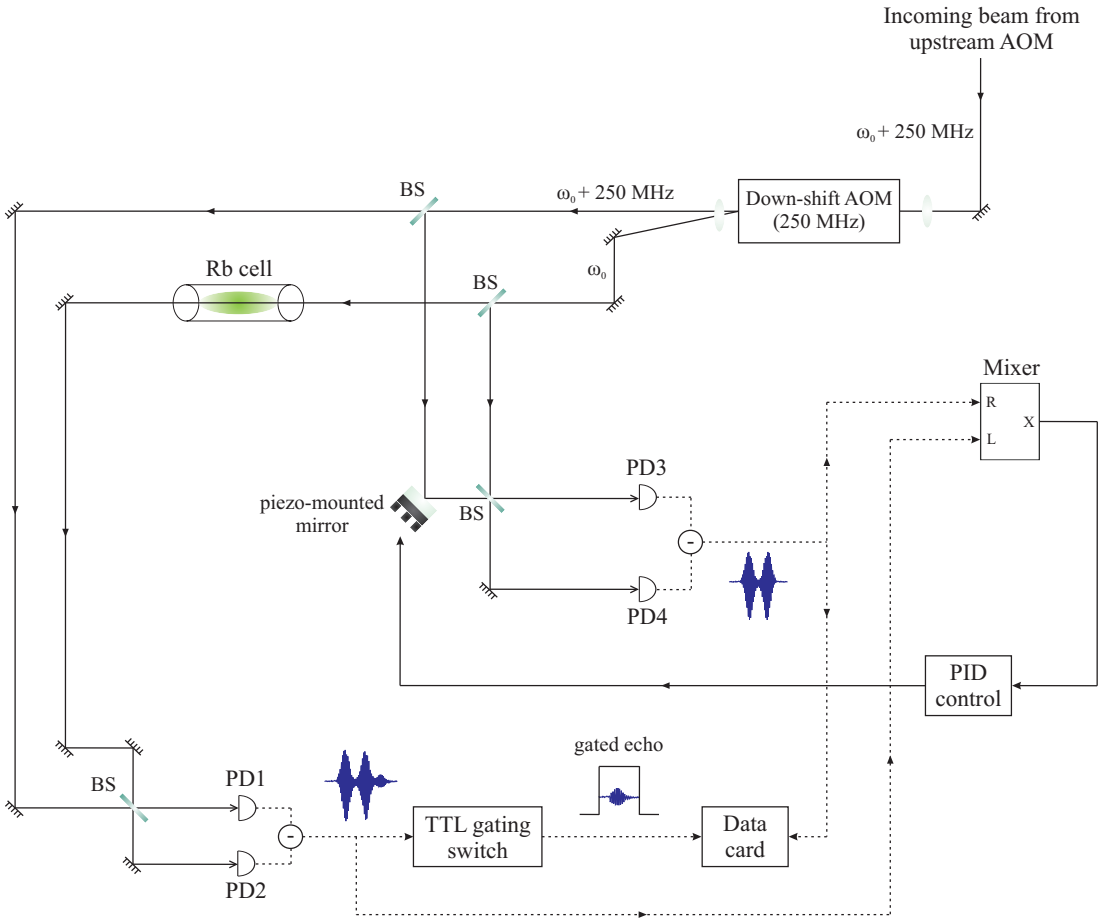

Figure 7.16: Proposed experimental set-up for correcting the long-term lifetime variations. The signal from a separate heterodyne alignment without the presence of a Rb cell would be mixed with the signal containing the echo and fed back to a piezo-mounted mirror to correct for mirror vibrations and long-term phase variations.

separate reference interferometer without the presence of a Rb cell. For each value of T, the time-averaged beat note in the reference interferometer can be subtracted from the time-averaged echo signal. The subtraction of these two signals would eliminate the first two terms in Eq. (7.1), so that only the echo term survives. To ensure that the subtraction works well for all T values and on long time scales, both interferometers must have the same relative phase. To achieve this outcome, we propose controlling the optical phase in the reference interferometer with a piezo-mounted mirror with a response time of $\sim$50 ms so that it is faster than the time scale of any anticipated phase variations. A correction signal obtained by mixing the two heterodyne beat notes and integrating the resulting DC signal can be fed back to the piezo to ensure the necessary long-term stability.

8 Conclusions and future work

The first part of this thesis presents simple adaptations of the well known IF-based ECDL design that include the development of an auto-locked controller that can tune and stabilize the laser frequency using various algorithms and a vacuum-sealed cavity that reduces the effects of pressure variations [2]. The long-term performance is characterized at both 633 nm and 780 nm using the ADEV of the beat note and of the lock signal. These studies suggest that reducing current noise and cavity pressure are both important for improving the long-term stability of the laser system. Further improvements at lower cavity pressures may be possible since performance limitations appear to be related to outgassing. We incorporate the laser with a state-of-the-art commercial gravimeter to demonstrate accurate measurements of gravity that are relevant for natural resource exploration. The auto-locking features of the laser are also potentially useful for realizing the basis of a LIDAR transmitter used in remote sensing to detect trace gases. The versatility of the system has enabled it to be integrated with tapered amplifier waveguides and acousto-optic switches for

high-power, pulsed applications. These include industrial magnetometry [6, 7], precise determinations of atomic lifetimes [94, 21], atom interferometry with cold atoms [1, 8], and diagnostic experiments involving trapped atoms [95].

The laser characterization results presented here enabled gravimeter trials with a laboratory prototype of the IF-based ECDL operating at 633 nm. The subsequent success of the 780-nm IF-based ECDL has opened the door for future gravimeter trials using portable engineering prototypes of these laser systems. Since the hyperfine spectra of the 780-nm laser system are readily identifiable by inspection, it is easy to verify (without relying on a wavemeter) that the auto-locking pattern-matching algorithm is frequency stabilizing the laser to the desired peak. As a result, transition frequencies obtained on the basis of femtosecond comb measurements can be readily used as inputs to the gravimeter. However, the 780-nm laser systems cannot be used in real-time beat note experiments with the He-Ne lasers that are already incorporated with the Scintrex gravimeters. For this reason, the industrial partner Scintrex Ltd. may prefer to utilize our 633-nm laser systems, despite significant challenges. Firstly, the availability of reliable low-cost laser diodes remains a concern. Secondly, spectra of repeating molecular series are nearly identical, thereby making it difficult for the auto-locking algorithm to lock to the transition from a cold start of the laser without reliance on a wavemeter. However, both 633-nm and 780-nm IF lasers are capable of producing much more power than the iodine-stabilized He-Ne lasers, and thereby

achieve better signal-to-noise ratios. As a result, we expect to continue trials of portable engineering prototype laser systems with Scintrex gravimeters.

The atomic lifetime measurement presented in this work highlights the advantages of the photon echo technique for achieving the most accurate determinations of such lifetimes. In this thesis, we have reported a transit-time corrected value of 26.10 ns with a statistical uncertainty of 0.03 ns (0.11%) in 4 hours of data acquisition for the ^{85}Rb $5^2P_{3/2}$ lifetime, acquired over several weeks. This determination is consistent with the value represented in reference [25], but it disagrees with the results of references [24, 70]. Furthermore, our best estimate of the statistical uncertainty of 0.013% from the ADEV floor value is only a factor of two larger than the statistical uncertainty of the best lifetime measurement [69], which is indicative of the potential of the photon echo technique. Our studies of the technical limitations supported by a simple model suggest that the long-term stability is related to eliminating the tails of optical excitation pulses. In Fig. 8.1 we present a possible scheme using a higher-frequency (800 MHz) AOM to achieve even shorter (5 ns) excitation pulses. Since the pulse bandwidth will be more than two times larger than in this work, we can also anticipate an increase in the signal strength. An additional AOM that is also shown in Fig. 8.1 will enable optically pumping atoms out of the $F = 2$ ground state in ^{85}Rb and further increase the signal strength by a factor of two. A notable challenge with this approach is that it is necessary to use suitable impedance-matched resonant

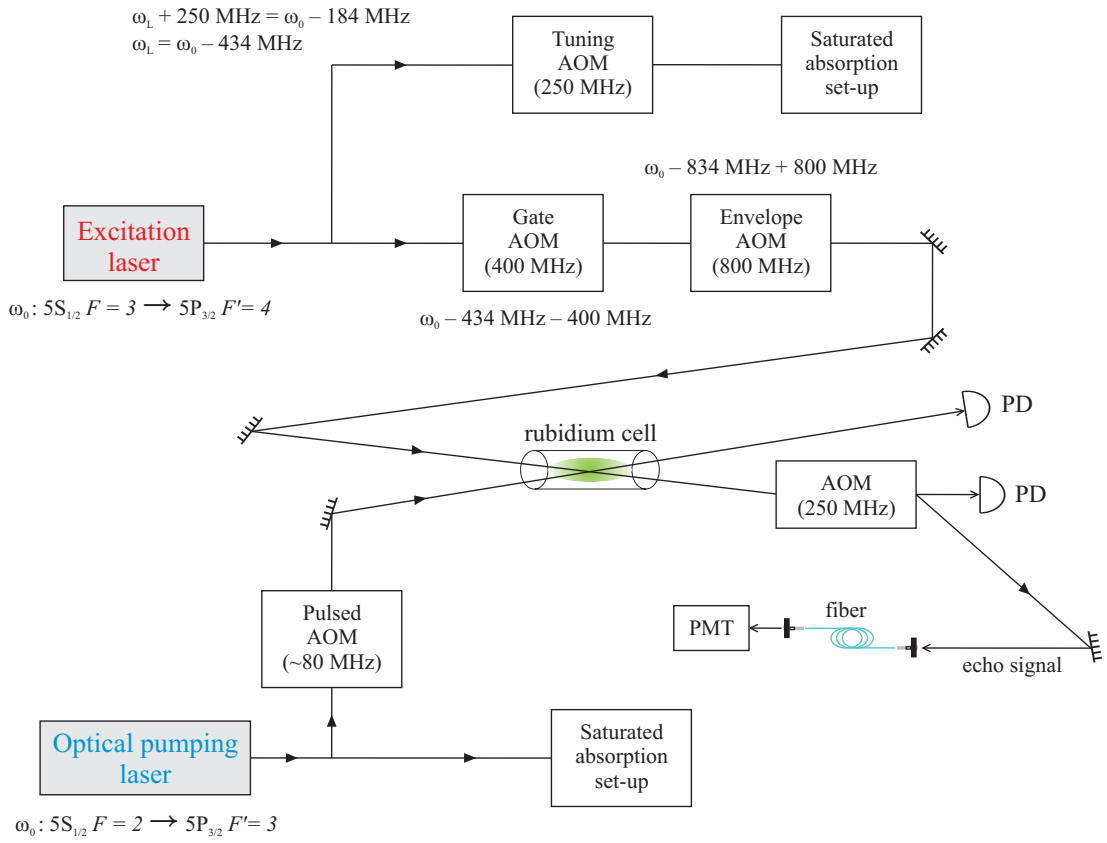

Figure 8.1: A possible scheme for a future echo experiment involving shorter excitation pulses generated by an 800-MHz AOM. We show both heterodyne and PMT detection schemes. The set-up also involves an optical-pumping AOM to empty out the $F = 2$ ground state prior to applying the excitation pulses.

cavities and RF switches with faster settling times to reduce the excitation pulse widths by the desired factor of two compared to the experimental work presented here. However, such improvements will not sufficiently eliminate the pulse tails, suggesting that the feedback loop we have outlined based on our model in Chapter 7 offers a more effective solution for reducing the observed lifetime variations. Our studies of the fractional uncertainty in the lifetime value show that the advantages of the high repetition rate can be fully exploited to achieve a statistical precision of 0.03% for a single exponential decay recorded over ∼10 minutes if the long-term variations are eliminated. Exploration of systematic effects at such a level would open the possibility of comparative measurements of the lifetimes of the Rb $5^2P_{3/2}$ and $5^2P_{1/2}$ levels for even more precise comparisons with theory that can serve as tests of the standard model. Since the echo technique is generally applicable to low-lying, closed transitions in atomic systems with large oscillator strengths, it could open the door for a new round of such lifetime measurements. Although the echo technique can achieve even lower fractional uncertainties for longer-lived lifetimes, its applicability to upper-level transitions is possibly limited due to competing coherent optical effects such as superradiance and superfluorescence [96] that also lead to rapid relaxation. However, for specific level schemes, multi-step incoherent excitation can at least limit the evolution of superradiant processes and create conditions for utilizing the echo technique.

A Applications of home-built ECDLs to laboratory courses

One of the motivations of designing the IF-based ECDLs is to support our two semester-long laboratory courses dedicated to laser spectroscopy and atom trapping. These courses constitute a powerful approach for teaching experimental physics in a manner that is both contemporary and capable of providing the background and skills relevant to a variety of research laboratories. The courses are designed to be accessible for all undergraduate streams in physics and applied physics, as well as incoming graduate students. In the introductory course, students carry out several experiments in atomic and laser physics. In a follow-up course, students trap atoms in a magneto-optical trap (MOT) and carry out preliminary investigations of the properties of laser-cooled atoms based on the expertise acquired in the first course. In this appendix, I discuss my contributions to developing and refining these experiments [15]. In particular, an optical tweezers experiment for trapping dielectric particles in solution and in free space has developed into a full-fledged research project, as

discussed in Chapter 1.

A.1 Description of experiments in the Laser Spectroscopy course

We now provide an overview of the experiments in the Laser Spectroscopy course along with concluding remarks about the relevance of these experiments to the Atom Trapping course. All experiments reviewed in this section provide a suitable background for experiments with atoms in a MOT.

Most of the laser spectroscopy experiments in the course are carried out in Rb vapour at room temperature using ECDLs. The energy level diagrams for the D_2-lines in ^{85}Rb and ^{87}Rb are shown in Fig. A.1(a). The Doppler-broadened absorption spectrum obtained by scanning the ECDL several GHz over the Rb resonances in a 5-cm long vapour cell at room temperature is shown in Fig. A.1(b). The Doppler widths of the individual transitions (for example, the $F = 3 \rightarrow F' = 2, 3, 4$ resonances in ^{85}Rb) can be obtained from background-subtracted fits. The calculated FWHM for an isolated two-level atomic system at a wavelength of 780 nm and a temperature of 300 K is 511.2 MHz. It is an interesting exercise to understand this discrepancy using known frequency splittings between individual transitions that contribute to the fitted line shape and the corresponding transition probabilities. The Doppler-

free saturated absorption spectrum corresponding to the aforementioned resonance is shown in Fig. A.1(c). A fit to the $F = 3 \rightarrow F' = 4$ resonance is shown in Fig. A.1(d).

A.1.1 Emission and absorption spectroscopy and the electro-optic phase modulator

Students are introduced to atomic structure and absorption and fluorescence spectroscopy in the first part of the experiment. The two measurement techniques are compared and contrasted. A schematic of the experimental set-up is shown in Fig. A.2. A weak probe beam is scanned across Rb resonances in a vapour cell and the absorption is detected by photodiode A. In this manner, the Doppler-broadened absorption spectra from the ground states of ^{85}Rb and ^{87}Rb can be measured. The spectra are fitted using Gaussian functions, as shown in Fig. A.1(b). The absorption of a weak probe beam in the presence of a strong counter propagating pump beam is detected by photodiode B showing Doppler-free resonances as shown in Fig. A.1(c). A Lorentzian fit to a single resonance line is shown in Fig. A.1(d).

In a separate experiment, an electro-optic phase modulator (EOM) is placed in the pump laser with the probe beams blocked [97, 98]. This commercially-available modulator is tuned to a resonance frequency of 2.915 GHz. This value was chosen corresponding to the difference between the $F = 3 \rightarrow F' = 4$ and $F = 2 \rightarrow F' = 3$ transitions in ^{85}Rb, shown in Fig. A.1(a).

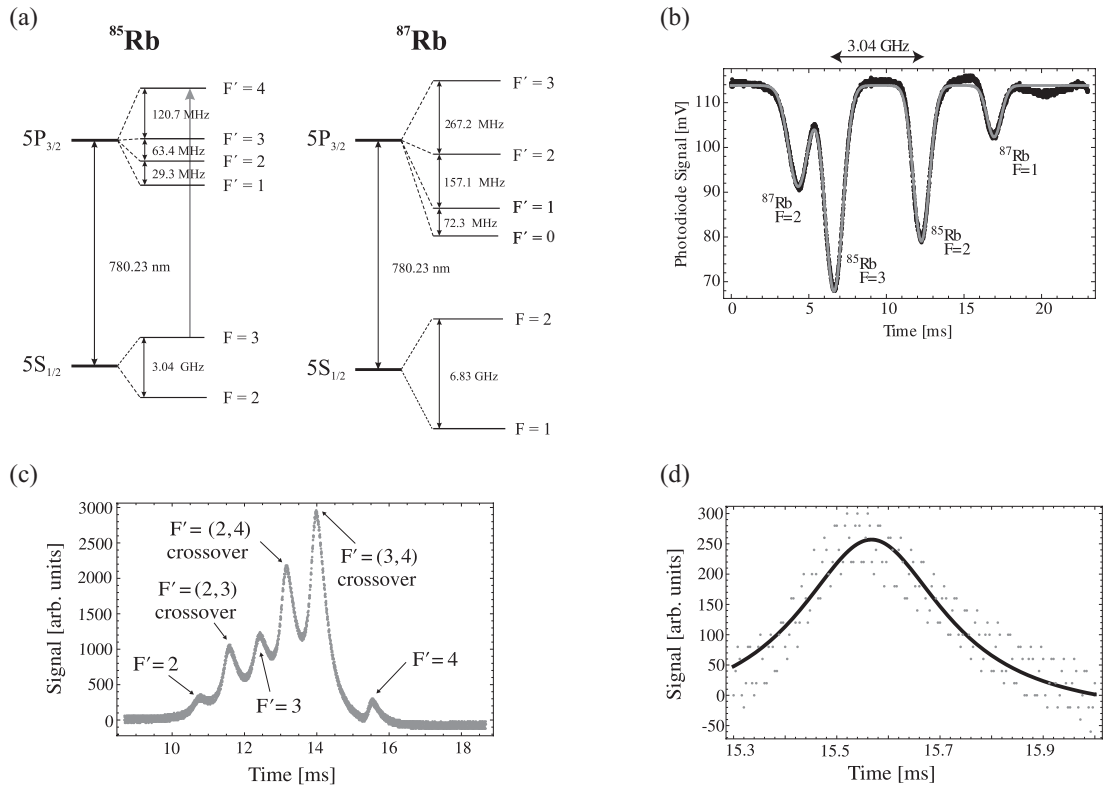

Figure A.1: (a) Energy level diagrams for ^{85}Rb and ^{87}Rb. The Rb reference cell contains the two naturally-occurring isotopes in the number ratio of 72:28. (b) Oscilloscope trace of Doppler-broadened absorption spectra in ^{85}Rb and ^{87}Rb observed by scanning the ECDL. The ground states corresponding to each peak are labelled. The frequency interval between the two ground states in ^{85}Rb is marked. The time axis can be converted to frequency units based on the known separation between energy levels. The FWHM extracted from a Gaussian fit of the $F = 3 \rightarrow F' = 2, 3, 4$ resonance is (735 ± 5) MHz. Based on Beer's law, $I = I_0 e^{-\alpha(\nu) l}$, where $\alpha(\nu)$ is the absorption coefficient, l is the length of the Rb cell, I_0 is the incident intensity, and I is the transmitted intensity.

Figure A.1: (cont'd caption) We find that the maximum absorption corresponds to an optical depth of $\alpha_0 l = 0.516 \pm 0.003$, where $\alpha_0 = \alpha(\nu_0)$ and ν_0 is the resonance frequency. (c) Oscilloscope trace of Doppler-free spectrum for the ^{85}Rb $F = 3 \rightarrow F' = 2, 3, 4$ transitions. The frequency interval between the $F' = 4$ peak and the adjacent crossover resonance is 60.4 MHz. (d) An expanded plot of the $F = 3 \rightarrow F' = 4$ resonance line. A FWHM of (12.7 ± 0.9) MHz is obtained from a Lorentzian fit. In general, this value should have contributions from natural broadening ($\sim$6 MHz), power broadening, and laser linewidth.

In the EOM experiment, the pump beam intensity is fixed and the fluorescence spectra from a detector at an angle of 90° [photodiode C in Fig. A.2] with respect to the laser beam is monitored. Spectra are recorded with the EOM turned on and off, as shown in Fig. A.3. New spectral features that are displaced by the operating frequency of the EOM are produced. These features can be used to infer the efficiency of the EOM. In addition, it is an interesting challenge to interpret the relative changes in amplitudes of other spectral lines [97].

This experiment can also be carried out using a home-built EOM with a resonance frequency of $\sim$ 20 MHz. The cost of the home-built EOM is approximately one sixth of the cost of the commercial EOM [98]. For experiments with low-frequency EOMs, it is necessary to measure Doppler-free absorption spectra (in the presence of pump

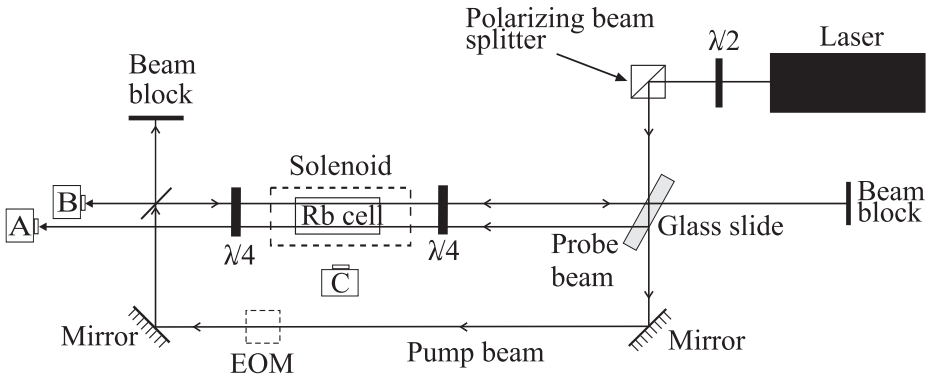

Figure A.2: Saturated absorption set-up used in emission and absorption spectroscopy, Zeeman shift, and laser frequency stabilization experiments. A quarter wave-plate represented by $\lambda/4$ is used to produce circularly-polarized laser beams. A half wave-plate, represented by $\lambda/2$, is used to control the ratio of power reflected and transmitted by the polarizing beam splitter. "A" and "B" represent photodiodes used for recording absorption spectra. The absorption of a weak probe beam that serves as a reference is recorded by photodiode A. The absorption of a weak probe beam in the presence of a strong counter-propagating pump beam is recorded by photodiode B. Electronic subtraction of the signals from these photodiodes gives a Doppler-free spectrum shown in Fig. A.1(c). Photodiode C is used to record right-angle fluorescence. Locations of the EOM used in the emission and absorption spectroscopy experiment and the solenoid used in the Zeeman shift experiment are shown by dashed lines. In experiments with the EOM, the two weak probe beams are blocked and only the pump beam remains on.

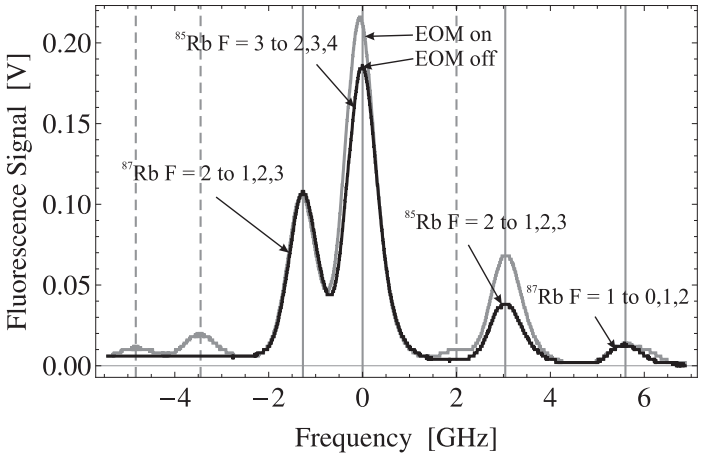

Figure A.3: Fluorescence spectra from a pump laser beam passing through an EOM and a Rb vapour cell. The laser is scanned over several GHz and a fluorescence signal is recorded by photodiode C in Fig. A.2. The black curve shows the fluorescence with the EOM off. The grey curve is obtained with the EOM on. The operating frequency of the EOM is 2.915 GHz which represents the energy difference between the $F = 3 \rightarrow F' = 4$ and $F = 2 \rightarrow F' = 3$ transitions in ^{85}Rb.

and probe lasers) to resolve the side-bands.

A comprehensive introduction to atomic level structure, Doppler-free spectra, and cross-over resonances is provided in the laboratory manual [99] so that students can interpret the results. A description of the lineshapes due to Doppler broadening and natural broadening is also provided. A brief description of electro-optic phase modulation and applications of EOMs is provided in connection with the last part of the experiment.

Knowledge of atomic level structure and frequency shifts of laser beams are crucial for experiments in atom trapping since these experiments require frequency stabilization and frequency tuning of a laser beam with respect to an atomic spectral line. Trapping ^{85}Rb atoms in a MOT requires a trapping laser to rapidly cycle atoms between the $F = 3$ and $F' = 4$ states and a second (repump) laser to optically pump the $F = 2$ ground state. The laser frequencies can be derived from the same ECDL using an EOM with an appropriate operating frequency.

A.1.2 Zeeman shift

In this experiment, the frequency shift of an atomic transition in Rb is studied as a function of magnetic field strength [42]. The saturated absorption set-up shown in Fig. A.2 is used to observe the Doppler-free Rb spectrum shown in Fig. A.1(c). A solenoid is placed around the Rb vapour cell [see Fig. A.2] to produce a nearly uniform magnetic field. The laser is scanned over the $F = 3 \rightarrow F' = 4$ atomic resonance as shown in Fig. A.1(a) and Fig. A.1(d). To measure the Zeeman shift of this spectral line, spectra are simultaneously recorded with reference to a separate Rb vapour cell under ambient conditions. This procedure is crucial for eliminating the effect of laser frequency drifts. The magnetic field has been sufficiently large (> 1 Gauss) to overwhelm the effect of the Earth's field, but not large enough (< 30 Gauss) to produce level mixing. It is also important to ensure that the circular polarization of

both pump and probe beams are set so that they drive the same transition.

An example of the measured Zeeman shift plotted as a function of magnetic field is shown in Fig. A.4. The slope is consistent with the expected Zeeman shift for the $F = 3, m_F = 3 \rightarrow F' = 4, m_{F'} = 4$ transition. This suggests that a system consisting of seven independent transitions between the $F = 3$ and $F' = 4$ levels can be modelled by a two-level system. We attribute this behaviour to two effects [42]. Firstly, for circular polarization, the transition probabilities increase for transitions with higher magnetic quantum numbers. For example, the transition probability for the $m_F = 3 \rightarrow m_{F'} = 4$ spectral line is 28 times larger than the transition probability for the $m_F = -3 \rightarrow m_{F'} = -2$ spectral line. Secondly, if the beam diameter is sufficiently large such that the transit time is comparable to the optical pumping time, optical pumping during the scan time of the pump laser can preferentially populate the $F = 3, m_F = 3$ ground state. It is instructive to record the Zeeman shifts of both Doppler-free and cross-over resonances with different polarization settings for the pump and probe and compare the measured shifts with theory.

It is notable that the narrow laser linewidth and Doppler-free spectroscopy allow the Zeeman shift to be characterized using a small wire-wound solenoid and a compact set-up. In contrast, the Zeeman shift is typically studied in upper-year laboratories using a discharge lamp source and a large water-cooled solenoid to generate magnetic fields of ~ 1 T.

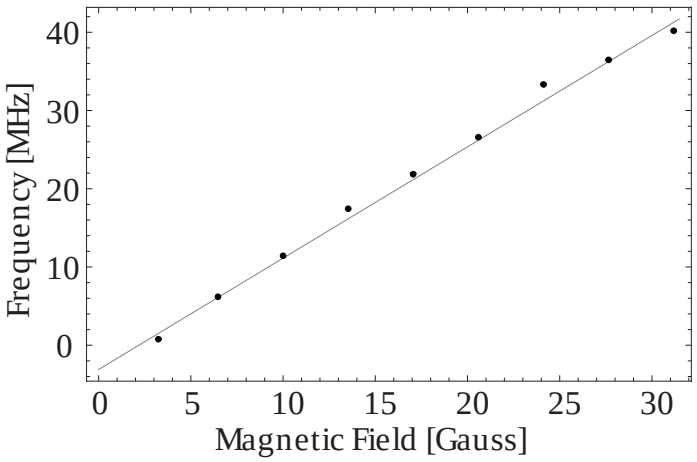

Figure A.4: The frequency shift of the $F = 3 \rightarrow F' = 4$ transition as a function of magnetic field. The frequency shift is obtained by recording the position of the spectral line in a Rb cell placed in a magnetic field relative to the position of the spectral line without a magnetic field. A value of (1.49 ± 0.08) MHz/G for the Zeeman shift is found from the slope of a straight line fit. The expected value for the Zeeman shift of the $m_F = 3 \rightarrow m_{F'} = 4$ sublevel transition is 1.4 MHz/G. The horizontal error bars are estimated to be $\pm 5\%$ and the vertical error bars are comparable to the size of the points.

In the final part of the experiment, the dependence of the width of a spectral line on laser intensity is studied. In this case, the width of the Doppler-free resonance is recorded as a function of the pump beam intensity, which is varied by using a $\lambda/2$ wave-plate and polarizing beam splitter at the entrance of the saturated absorption set-up. Alternatively, optical neutral density filters can be introduced into the pump beam. It is possible to infer the natural linewidth of the spectral line as well as the saturation intensity of the transition from this data if the vapour cell is magnetically shielded.

Background concepts related to the Zeeman shift, calculation of Landé g-factors and power broadening are described in the manual. In this way, students are introduced to the Zeeman shift, which is responsible for the restoring force in a MOT. Additionally, the frequency shifts of laser beams used in atom trapping can be controlled by Zeeman shifting spectral lines to which the lasers are locked [42].

A.1.3 Faraday isolator and Fabry-Pérot interferometry

Two separate experiments have been combined into this lab. In the first part, the function of polarizing elements such as linear polarizers and wave-plates are reviewed. Linearly- and circularly-polarized light are distinguished by measuring the transmission through a rotating polarizer attached to a compact motor. Since optical feedback can alter or damage laser diodes, the utility of using an optical isolator consisting of

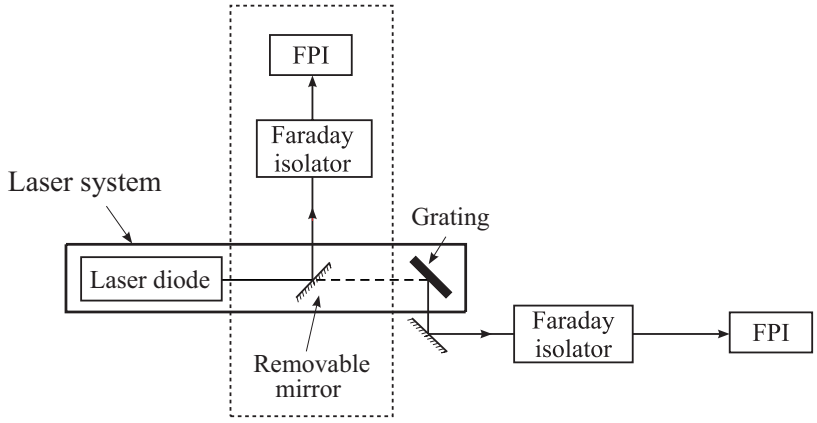

Figure A.5: Experimental set-up for measurement of the laser linewidth using a FPI. The grating in the ECDL cavity is bypassed by inserting a mirror attached to a removable mount so that the linewidth of the free-running laser diode can be determined. This configuration is shown by the dotted box. When the mirror is removed, the linewidth of the laser is much smaller ($\sim$ 1 MHz) due to the presence of grating feedback. Since the FPI resolution is $\sim$ 60 MHz, only the instrument-limited linewidth is measured in this case.

a polarizing cube and $\lambda/4$ wave-plate to reduce optical feedback is demonstrated. This arrangement reduces optical feedback only for a particular polarization. Subsequently, students align a home-built Faraday isolator [100], a device that eliminates optical feedback for all polarizations. The rotation angle and the isolation ratio of the isolator are measured in the experiment.

In the second part of the experiment, light from the ECDL (linewidth $\sim$ 1 MHz) is sent through a Fabry-Pérot interferometer (FPI) with a resolution of $\sim$ 60 MHz.

The ECDL grating that provides optical feedback is bypassed so that the linewidth of the laser becomes larger than the FPI resolution. The laser frequency is fixed and the transmission spectrum of the FPI is recorded by scanning the spacing between the cavity mirrors. The linewidth of the free-running laser diode can be estimated from the transmission spectrum of the FPI. The experiment is repeated after the reintroduction of the grating. In this case, the instrument-limited resolution rather than the laser linewidth is measured. A schematic of the experiment is shown in Fig. A.5 and representative FPI spectra are shown in Fig. A.6. The mode characteristics of the ECDL can also be investigated by varying the diode current and temperature.

The operating principles and design of a Faraday isolator and essential properties of the FPI are reviewed in the lab manual. The students are exposed to the properties and characteristics of narrow linewidth ECDLs that are used for atom trapping.

A.1.4 Laser frequency stabilization and the lock-in amplifier

This experiment focuses on the use of a lock-in amplifier for frequency stabilization of a diode laser. The saturated absorption set-up used in this experiment is shown in Fig. A.2. The schematic for the feedback loop required to lock the laser frequency to the peak of an atomic spectral line is shown in Fig. A.7.

In the first part of this experiment, students are guided through the essential components of a lock-in amplifier, shown in Fig. A.8. Exercises include studying the

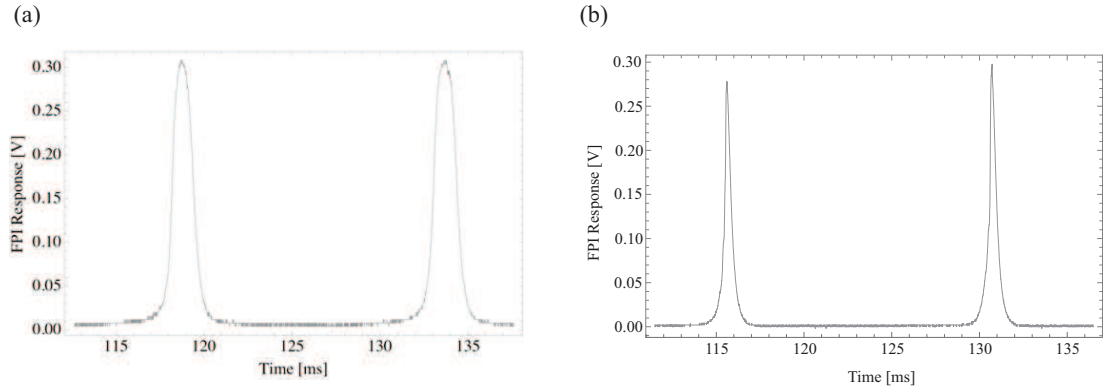

Figure A.6: Transmission peaks obtained by operating the diode laser at a fixed frequency and scanning the FPI. (a) FPI peaks without grating feedback. The measured FWHM is (133.3±5) MHz. (b) FPI peaks with grating feedback. The measured FWHM of (66.7 ± 3) MHz is comparable to the calculated resolution of the FPI. The value of the free-spectral range of the spherical mirror FPI (c/4L), calculated on the basis of the known cavity length of L = 7.5 cm, is ~ 1 GHz. Since the separation between adjacent transmission peaks is equal to the free-spectral range, it is possible to convert the time axis into frequency units.

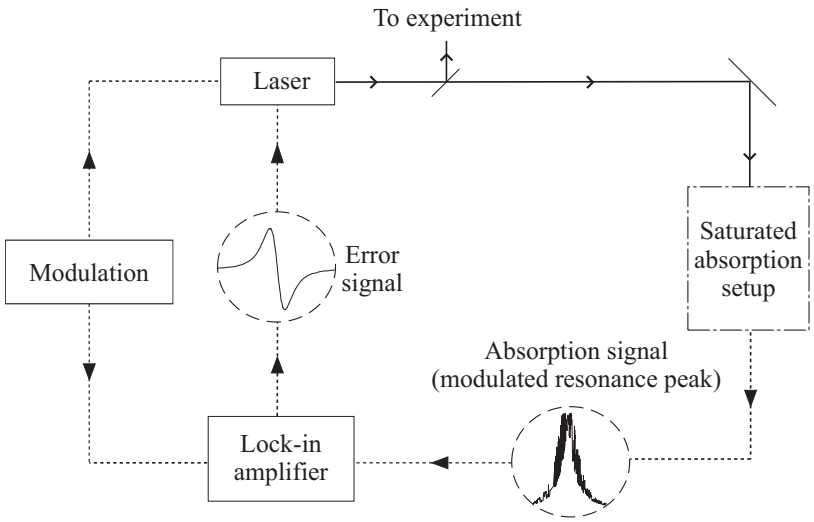

Figure A.7: Set-up for laser frequency stabilization using a lock-in amplifier. The modulation was provided by a function generator operating at ∼7 kHz. A scan controller is used to scan the laser frequency at a rate of ∼10 Hz. An example of the saturated absorption set-up is shown in Fig. A.2. A trace of the saturated absorption signal obtained by scanning the laser over a single Doppler-free transition is shown. For illustrative purposes, this trace was recorded with a large amplitude for frequency modulation. The output of the lock-in amplifier generates the corresponding dispersion shaped error signal. To lock the laser to the peak of this resonance line, the laser frequency is centred on the resonance peak, and the scan amplitude is gradually reduced (ideally to zero) before engaging the feedback loop.

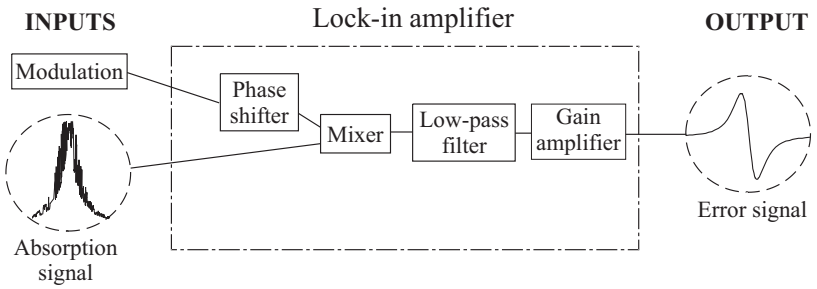

Figure A.8: Schematic diagram showing the essential components of a lock-in amplifier.

performance of a phase shifter and radio frequency (RF) mixer. The phase shifter consists of an analog circuit with a variable resistor that allows the phase shift imposed on an RF waveform to be varied and calibrated. Two RF inputs, consisting of the output of the phase shifter and the modulated absorption signal, are used as inputs to the mixer. The mixer output is verified to scale as the cosine of the phase difference between the two RF inputs.

In the second part of the experiment, a commercial lock-in module attached to the laser controller is used to study the dispersion-shaped error signal shown in Fig. A.8. For this experiment, the modulated saturated absorption signal and the modulation from a built-in function generator are used as inputs to the lock-in. The dependence of the error signal on lock-in phase is studied by scanning the laser across a suitable atomic resonance, as shown in Fig. A.9. To lock the laser, the error signal is first minimized by varying the phase, as shown in Fig. A.9(b). The phase is incremented

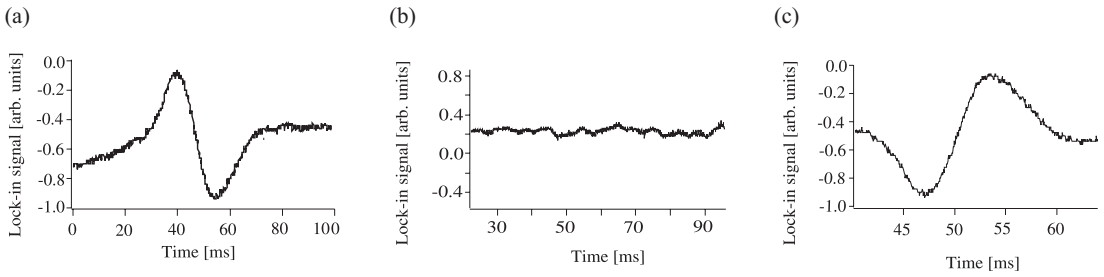

Figure A.9: Lock-in output (error signal) obtained by scanning the laser across a resonance line for various phase shifts between the absorption signal and the modulation: (a) $\phi = 0°$, (b) $\phi = 90°$ and (c) $\phi = 180°$.

by $\pm 90°$ to maximize the error signal, as shown in Figs. A.9(a) and (c). It can be determined that the laser will remain locked for one of these settings and that it will be forced away from resonance for the other setting. To lock the laser, the scan amplitude is reduced and the feedback loop is engaged by sending the error signal to the laser. After locking the laser to a particular spectral line, the frequency stability of the laser is determined by recording the fluctuations in the DC level of the error signal, as shown in Fig. A.10. This figure also illustrates the frequency excursions of the laser without feedback.

Atom trapping experiments require frequency stabilized lasers to drive specific atomic transitions. The lab manual presents both a physical model of the error signal [101], as well as a more mathematical treatment [102].

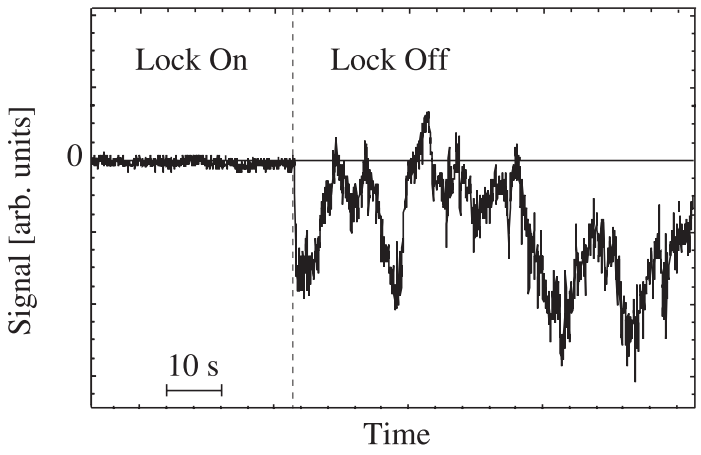

Figure A.10: Lock-in error signal recorded with and without engaging the feedback loop. For both parts of the trace, the scan amplitude has been turned off, whereas the modulation remains on. The amplitude variations are mainly due to laser frequency fluctuations, which are greatly reduced with the feedback loop engaged (lock on). Under typical operating conditions, the diode laser remains locked for about 30 minutes.

A.1.5 RF components and optical heterodyne detection

Students are introduced to the function of RF components in the first part of this experiment. Simple experiments that utilize a voltage-controlled oscillator (VCO) are used to understand working principles of amplifiers, mixers, power splitters, frequency doublers, and TTL switches. For example, students can design a frequency doubler by connecting two outputs of a power splitter into a mixer and filtering out the low-frequency component. Other experiments include measuring the frequency range and power output of a VCO and measuring the on/off ratio of RF pulses using a mixer or a TTL switch.

In the primary experiment, a cw RF signal from an amplifier is used to drive an AOM. Light from one of the ECDL-based experiments described previously is aligned through the AOM. The first-order diffracted beam is rendered co-propagating with the undiffracted beam using a combination of mirrors and a 50/50 beam splitter, as shown in Fig. A.11(a). The undiffracted beam from the AOM serves as an optical local oscillator (LO). A photodiode placed in the path of overlapped beams records a heterodyne beat note at the RF frequency used to drive the AOM. Under typical operating conditions, the intensity of the diffracted beam is comparable to that of the undiffracted beam. If the AOM is driven at low power, the diffracted beam can represent a weak signal. With the LO blocked, the photodiode can be used to detect

the signal as a change in intensity. With the LO unblocked, the signal can be detected by the presence of the beat note. Other extensions of this experiment could include studying the size of the beat signal versus the power in the diffracted beam and comparing the smallest signals that can be measured using heterodyne and intensity detection.

The remainder of the experiment involves pulsing the RF signal driving the AOM and recording the diffracted pulse detected by the photodiode. Pulsing the amplitude of the RF signal from a VCO is accomplished using a function generator and a TTL switch, as shown in Fig. A.11(a). The photodiode records a time-delayed optical pulse, as shown in Fig. A.11(b). The envelope of the optical pulse exhibits the heterodyne beat note. The time delay between the trigger pulse used to drive the AOM and the corresponding optical pulse is measured. The distance between the transducer attached to the AOM crystal and the laser beam is recorded. These measurements allow the speed of sound through the AOM crystal to be inferred. The rise time of the diffracted pulse can be used to measure the size of the laser beam passing through the AOM. Additional exercises relating to this experiment could include demonstrations of setting up AOMs in a dual-pass configuration [66].

The background covered in the lab manual includes the theory of Bragg diffraction in an AOM and a derivation of the frequency shift of the diffracted beam based on the first-order Doppler shift for sound waves. In the atom trapping course, students

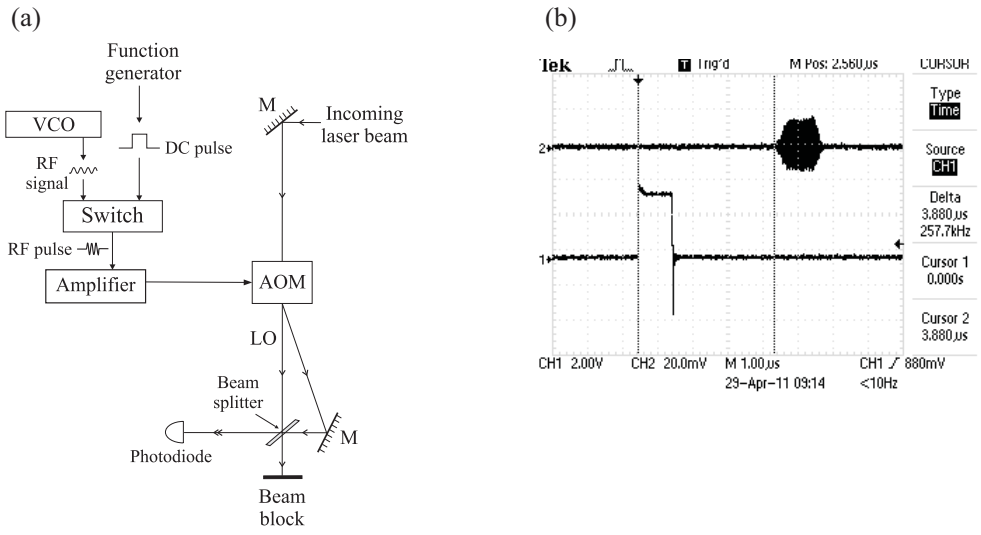

Figure A.11: (a) Heterodyne detection set-up. The incoming beam is generated by an ECDL operating at 780 nm. The optical LO is the undiffracted beam from the AOM. The first-order diffracted beam from the AOM is rendered co-propagating with the LO using a beam splitter and mirrors so that a heterodyne beat signal can be detected by the photodiode. The RF input to the AOM is either cw or pulsed, and the control electronics are shown. The output of the TTL switch is an RF pulse that drives the AOM. (b) The square pulse used to amplitude-modulate the AOM and corresponding time-delayed optical pulse detected by the photodiode. The square pulse is the signal input to the electronic TTL switch, which also triggers the oscilloscope. The optical pulse exhibits a beat note at the AOM drive frequency. The time delay between the onset of the square pulse and the beginning of the optical pulse is $(3.45 \pm 0.05)\mu$s. This delay is consistent with the estimated time for an acoustic wave to propagate from the transducer at the edge of the AOM crystal to the location of the laser beam passing through the AOM.

use an AOM to derive the frequency-shifted trapping laser beam from a diode laser locked to an atomic spectral line. The trapping laser can be amplitude modulated for a range of cold-atom experiments.

A.1.6 Optical detectors

This experiment is designed to provide a working knowledge of three different optical detectors: photodiodes, PMTs, and charged coupled devices (CCD cameras). In a preliminary experiment, cw light intensity is measured using both photodiodes and PMTs so that the dynamic range, saturation characteristics, and signal-to-noise ratios associated with these detectors can be estimated. Using an AOM, it is also possible to demonstrate pulsed detection. The response time of an optical detector with a 1-MΩ termination resistance is measured. The time constant of the detection system is modified by changing the termination resistor so that the rise time of the optical pulse from the AOM can be measured.

A triggered CCD camera and frame grabber are used to measure the fluorescence generated by an electron beam moving across the phosphor screen of an analog oscilloscope, as shown in Fig. A.12. The characteristic decay in fluorescence intensity as the beam sweeps across the screen is shown in Fig. A.13. We find that the decay time of the phosphor coating on the oscilloscope screen is strongly dependent on both the electron beam intensity and the oscilloscope time-base settings. For this

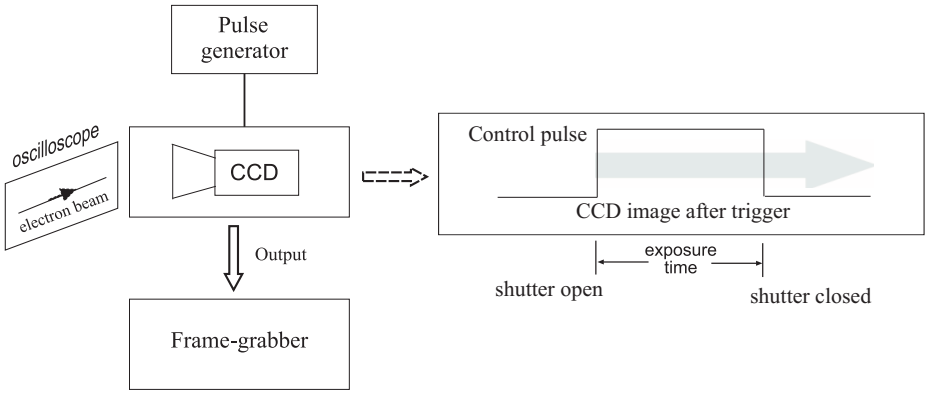

Figure A.12: A CCD camera and frame grabber are used to measure the fluorescence of an electron beam as it sweeps across the screen of an analog oscilloscope. A pulse generator is used to generate a TTL pulse that controls the shutter of the CCD camera.

measurement, we used an oscilloscope with a P31 phosphor.

Triggering the CCD prepares students for atom trapping experiments since photographing the electron beam fluorescence is analogous to photographing the ballistic expansion of a cloud of laser-cooled atoms after turning off the confining forces. CCD imaging is a standard technique used for measuring the temperature of trapped atoms [103]. PMTs and photodiodes are also extensively used in atom trapping. For example, a PMT can be used to measure trap fluorescence and estimate the number of trapped atoms and a photodiode can be used for measuring the absorption spectrum of the cold sample [23].

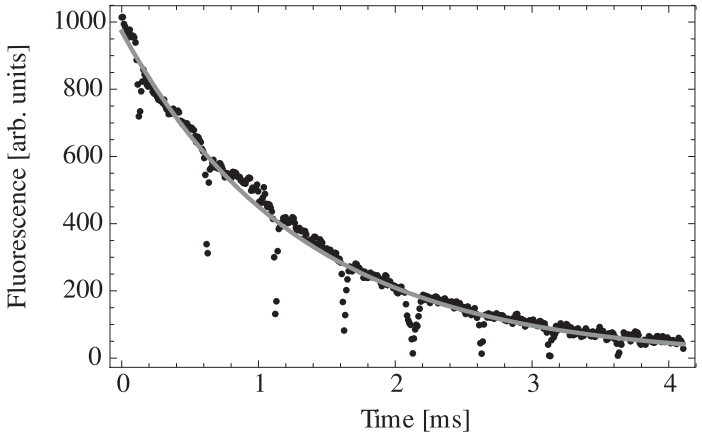

Figure A.13: Intensity of fluorescence due to an electron beam sweeping across the screen of a line-triggered oscilloscope recorded by a shutter-controlled CCD camera. The dips in intensity correspond to the grid lines on the oscilloscope. The spacing between the grid lines is determined by the time base setting of the oscilloscope, thereby allowing the pixel axis to be converted to a time scale. The solid curve is the best fit to the data based on a decaying exponential. The fit gives a decay time of (1.30 ± 0.03) ms.

A.1.7 Gaussian beam propagation and optical fiber coupling

This lab builds on earlier experiments in second-year optics, where students are introduced to techniques for obtaining the spatial profiles of laser beams. These techniques include scanning a pinhole or knife edge across the profile of a beam while measuring the transmitted intensity, or measuring the intensity through a series of calibrated apertures centered on the beam. In this dissertation, all measurements of the spatial profile are carried out using a commercially-available scanning knife-edge beam profiler.

In the first part of the experiment, the spatial profile of a focused He-Ne laser is measured along two orthogonal directions perpendicular to the direction of propagation of the laser beam. The measured beam size of a focused laser beam as a function of position is shown in Fig. A.14(a). The Rayleigh range and beam divergence can be determined from fits to the beam profile as a function of the distance from the position of the focus.

The second part of the lab demonstrates how spatial filtering can be used to improve the beam profile. Both pinhole filtering and optical fiber coupling are demonstrated. Since the experiment involves very few optical elements and the laser beam propagates over a limited distance on the optical table, a scratched cover slide is used to distort the beam profile. The effect of spatially filtering this beam using an optical

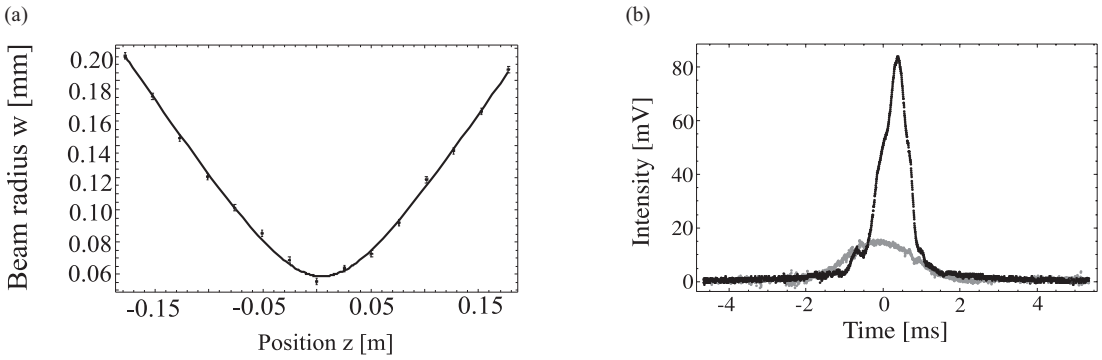

Figure A.14: (a) Beam radius, w, orthogonal to the direction of propagation as a function of distance (z) from a 20-cm focal length plano-convex lens. The beam size was measured using a scanning knife-edge beam profiler. The position $z = 0$ represents the focal spot. The solid line is a fit to the equation $w = w_0[1 + (z - z_1)^2/z_0^2]^{1/2}$, where $z_0 = \pi w_0^2/\lambda$. Here, w_0 is the minimum beam radius, z_0 is the Rayleigh range, and z_1 is an offset that specifies the location of the minimum beam radius from the origin. The fit gives $w_0 = (58.7 \pm 1.3)$ μm, $z_0 = (5.8 \pm 0.2)$ cm, and $z_1 = (4.6 \pm 0.8)$ mm. (b) Spatial profile of a laser beam before (black) and after (grey) passing through an optical fiber. The profile at the entrance to the fiber was obtained by distorting the beam using a scratched cover slide. The profiles represent the analog outputs of a scanning knife-edge spatial profiler.

fiber is shown in Fig. A.14(b).

Further appreciation of spatial profiles is emphasized in the atom trapping experiment, since the number of atoms that can be trapped in a MOT depends critically on the beam profile.

A.1.8 Vacuum components and pumping techniques

This experiment provides a working knowledge of some vacuum pumps and pumping techniques. The experimental set-up is shown in Fig. A.15. In the first part of the experiment, students use a roughing pump to pump on a vacuum chamber with a volume of ∼13 L. The pumping speed is investigated with different bellows hose lengths, apertures, and leaks. In all these cases, the decrease in the fore line pressure is measured as a function of time using a Pirani gauge and a stopwatch. We find that the change in pressure can be suitably modelled as a decaying exponential immediately after the pump down commences. For the geometry with the highest pumping speed, the transition from the viscous flow regime to the molecular flow regime is estimated to occur for pressures less than 10 mTorr. In the second part of the experiment, the vacuum chamber is pumped using a roughing pump in series with a turbo pump to a pressure of $\sim 10^{-6}$ Torr. The effect of outgassing is illustrated by valving off the turbo pump and by heating parts of the vacuum chamber.

The theoretical background in the laboratory manual includes a discussion of both

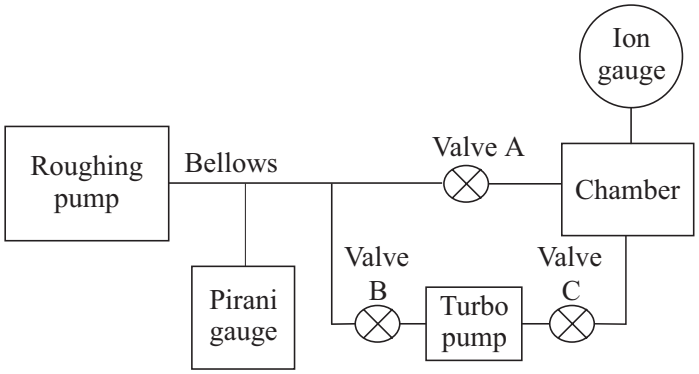

Figure A.15: Vacuum system used in the experiment. In the first stage of the experiment, valves B and C are closed and the chamber is pumped directly using the roughing pump. In the second stage, valve A is closed and the chamber is pumped by the turbo pump in series with the roughing pump.

continuum and molecular flow regimes, mean free path, and the effect of the diameter and the length of a hose on the conductance. The principles of operation of roughing pumps, turbo pumps, diffusion pumps, and entrapment devices such as ion pumps and cryogenic pumps are reviewed. A few common types of pressure gauges are discussed. This experiment provides a suitable background for understanding the conditions in the small volume vacuum chamber used for atom trapping experiments.

A.1.9 Optical tweezers

We have also introduced an optical tweezers experiment based on reference [104]. A suspension of polystyrene beads ($\sim$1-2 μm in diameter) in saline solution is placed

in a channel on a cover slide attached to a translation stage, as shown in Fig. A.16. The beads can be viewed on a CCD camera using a backlight for shadow imaging, as shown in Fig. A.17(a). The beads are trapped using light from a diode laser that outputs ~ 50 mW of power at a wavelength of $\lambda = 532$ nm. Most of the laser light incident on a dichroic mirror [oriented at 45° as shown in Fig. A.16] is focused onto the sample using a microscope objective. A lens mounted on a rail is used to adjust the size of the beam at the entrance to the objective. A small fraction of the back-scattered light from a trapped bead will pass through the dichroic mirror, along the line of sight associated with the backlight. The position of the bead can be tracked using the CCD camera. A LabVIEW interface displays an image of the trapped bead obtained by subtracting the background light, as shown in Fig. A.17(b). The interface allows the data associated with the trapped bead to be displayed either in real time or after the acquisition of a number of frames. Fig. A.17(b) also displays the spatial profiles of light reflected off a trapped bead along two orthogonal directions. These plots represent pixel readouts along directions marked by cursors placed on the image of the trapped bead. Due to the relatively slow processing time of the CCD camera, the data representing the bead positions are well separated in time ($\sim$15 ms) so that correlation effects can be ignored.

Fig. A.18(a) shows the mean-squared displacement of the bead (calculated in software) as a function of the inverse laser power. The spring constant, k_s, of the harmonic

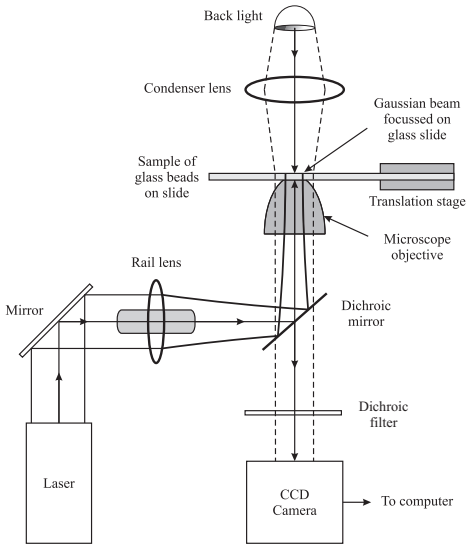

Figure A.16: Schematic diagram of the optical tweezers experiment. The laser source is a diode laser operating at $\lambda = 532$ nm. The dichroic mirror ensures that most of the laser light reaches the microscope objective. The rail lens is used to vary the size of the laser beam. The objective focuses the laser beam to a spot size of $\sim$3 μm. The sample of polystyrene glass beads in saline solution is placed at the focal spot of the laser. The sample is uniformly illuminated by a backlight. Light from this lamp source passes through a condenser lens and the sample. After passing through the microscope objective, it is imaged on a CCD camera. With the laser blocked, the CCD camera can image the glass beads suspended in solution. When the optical dipole force trap is aligned, the dichroic mirror and dichroic filter ensure that a small fraction of the light scattered by the trapped beads reaches the CCD camera. The scattered light follows the same optical beam path as the backlight and is sufficiently intense for the trapped bead to be imaged.

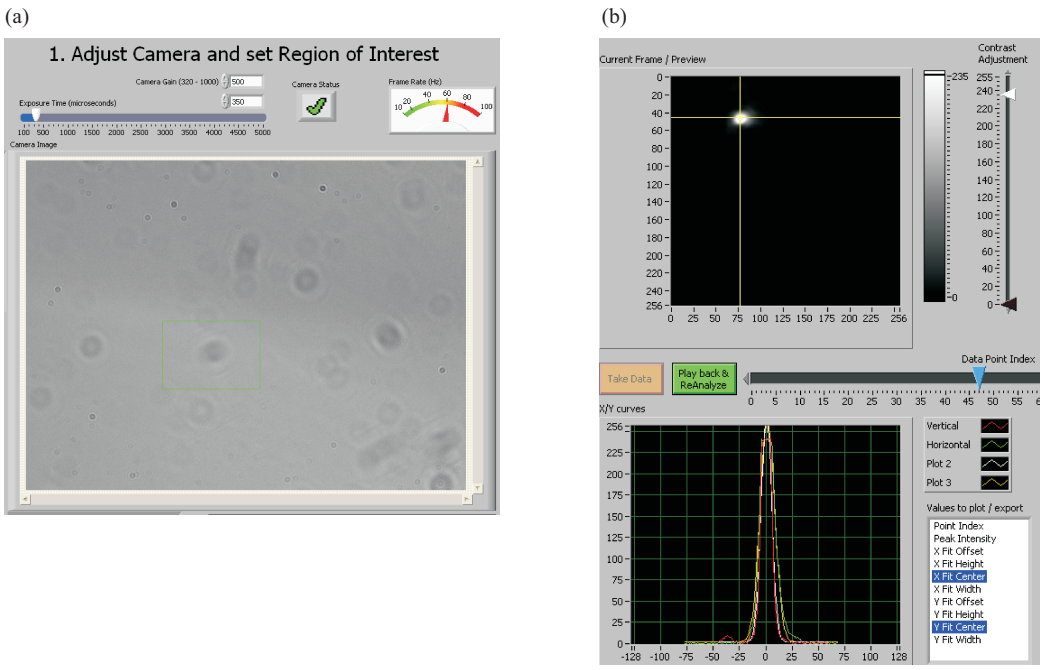

Figure A.17: Display of the LabVIEW interface used to record and analyse CCD images of the trapped beads. (a) Image of beads suspended in solution. (b) The upper frame shows the image of a 2-μm diameter trapped bead. The corresponding intensity profile is displayed in the lower frame.

potential associated with the dipole force trap is proportional to laser intensity. Therefore, the mean-squared displacement is inversely related to laser power in a manner consistent with expectations. The spring constant of the dipole force trap as a function of the laser power is shown in Fig. A.18(b). The spring constant was calculated by using the equipartition theorem and the measured mean-squared displacement. As expected, we find that the spring constant varies linearly with laser power.

The same set-up can also be used to measure the autocorrelation function of a trapped bead. In this case, a position sensitive detector (PSD) with a response time of $\sim$100 μs is used to track the bead position. The PSD is placed at the location of the backlight. To ensure a sufficient signal-to-noise ratio, an iris is placed in front of the PSD to eliminate background light. Fig. A.18(c) shows the bead displacement measured by the PSD over a time scale of 45 ms. An autocorrelation function can be calculated from this data, as shown in Fig A.18(d). The correlation time τ_c is inferred by fitting the data to a Lorentzian function [104]. Fig. A.18(e) shows the correlation time τ_c as a function of the laser power. The inverse dependence is consistent with the prediction for $\tau_c = \gamma/k_s$. Here, γ is the damping rate due to collisions with the solute molecules and the trapped bead.

An even more popular variant of this experiment has been added to the course, which allows students to trap micron-sized particles in free space using the same diode laser, as shown in Fig A.19(a). The simplest particles to trap are carbon-based

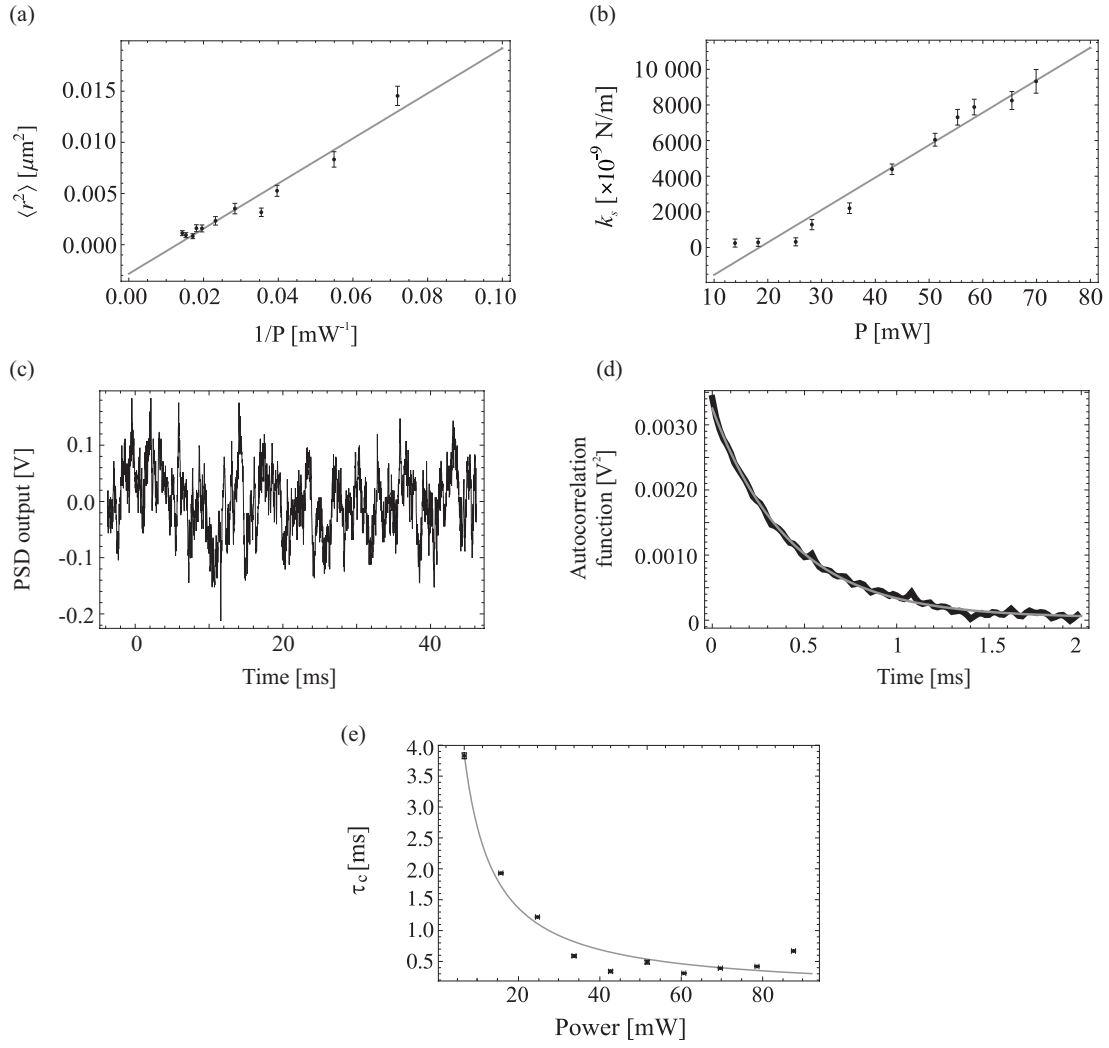

Figure A.18: (a) Mean-squared displacement as a function of inverse laser power. The power represents the measured value at the entrance to the microscope objective. Only ∼50% of the light reaches the sample. (b) Spring constant of the dipole force trap as a function of laser power. The horizontal axis has not been corrected for the power loss at the microscope objective. The points representing the spring constant are calculated from the data in part (a) on the basis of the equipartition theorem. (c) Signal from the PSD which represents the position of the bead as a function of time.

Figure A.18: (cont'd caption) (d) Auto-correlation function (black) calculated from the PSD signal by fitting to a Lorentzian (gray) for a small section of the data such as in part (c). The horizontal axis represents the time lag between the data points in the record. The fit gives a correlation time $\tau_c = (0.422 \pm 0.005)$ ms. (e) Correlation time as a function of laser power.

ink particles ablated from the surface of a permanent marker or saturated cotton swab. The particles are trapped near the location of the minimum beam waist. A plastic enclosure with glass-slide "window" is used to surround the region around the trap to shield the droplets from air currents. Particles can also be introduced into the trapping beam by atomization through one of the windows. In this manner, we have been able to measure the spring constant of the traps for different particles such as charcoal, graphite, and carbon black ink, as shown in Fig. A.19(b). However, the light intensity scattered by these particles is significantly smaller than the light scattered by the polystyrene beads. As a result, measurements of the autocorrelation function could not be carried out. In the recent past, we have overcome this limitation by using a CMOS camera that has the desired light sensitivity and can operate at rates of up to ∼300,000 fps, which is even faster than the response time of the PSD. Therefore, real-time imaging of a number of trapped particles has become possible. Using these results, we are in the process of measuring the damping rate γ using

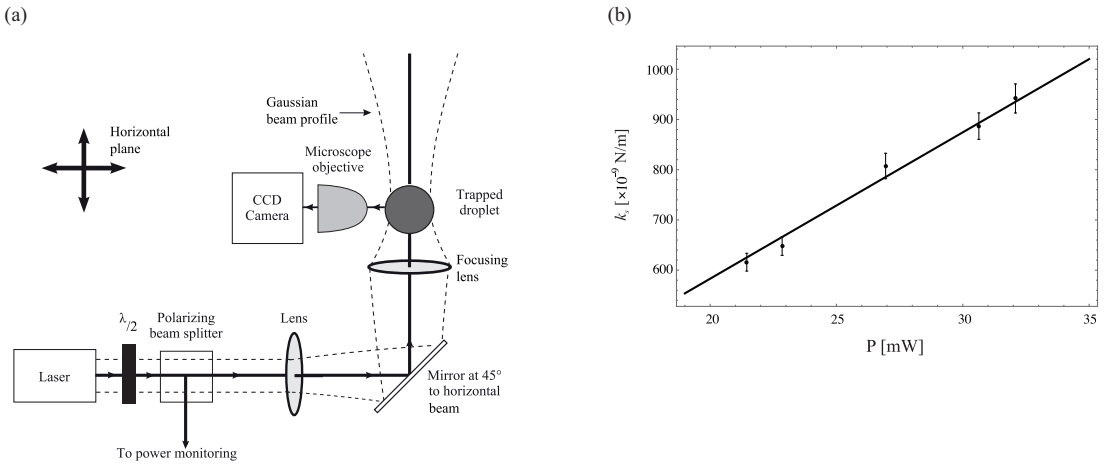

Figure A.19: (a) Modified experimental set-up for free-space trapping experiment. (b) Spring constant of the dipole force trap as a function of laser power for a charcoal particle confined in free space. The horizontal axis has been corrected for the power loss of the microscope objective.

two independent techniques. In the first case, we combine the time constant of the autocorrelation function and the spring constant, as in my preliminary experiments. In the second case, we either drop the particle after switching off the laser field and track its motion, or construct the trajectory of the particle being restored to the center of the trap when the laser field is turned back on. Both these experiments should allow γ to be determined independently.

The lab manual provides an introduction to the origin of the optical dipole force (ODF) on glass beads and discusses the mechanism by which the ODF can trap neutral atoms. The techniques used in this experiment are widely applied in biophysics

to manipulate proteins, DNA, and other organic molecules that can be tethered to glass beads [105, 106]. This experiment has additional relevance to atom trapping, since neutral atoms that are laser cooled and trapped in a MOT can also been loaded into an ODF trap, also known as a far-off resonance trap (FORT). FORTs can be designed to have large potential-well depths and have the advantage of low scattering rates in comparison to MOTs.

A.2 Description of experiments in the Atom Trapping course

The following section provides a description of the experiments in the Atom Trapping course. These experiments provide a suitable background for realizing a MOT and outline methods for characterizing the properties of the atom trap, such as atom number, trap size and density, and trap temperature.

Fig. A.20(a) shows a picture of the atom trapping apparatus. The stainless-steel vacuum chamber has eight symmetrically-aligned view-ports in the horizontal plane and two view-ports along the vertical axis. Six view-ports are used by the three pairs of orthogonally-directed trapping beams. Two view-ports in the horizontal plane are used for detection of trap fluorescence using a photodiode, and for CCD imaging of the atom cloud, as shown in Fig. A.20(b). The two remaining view-ports can be used for experiments such as absorption spectroscopy with a probe laser.

Typically, it takes a few weeks to prepare a vacuum system that is suitable for

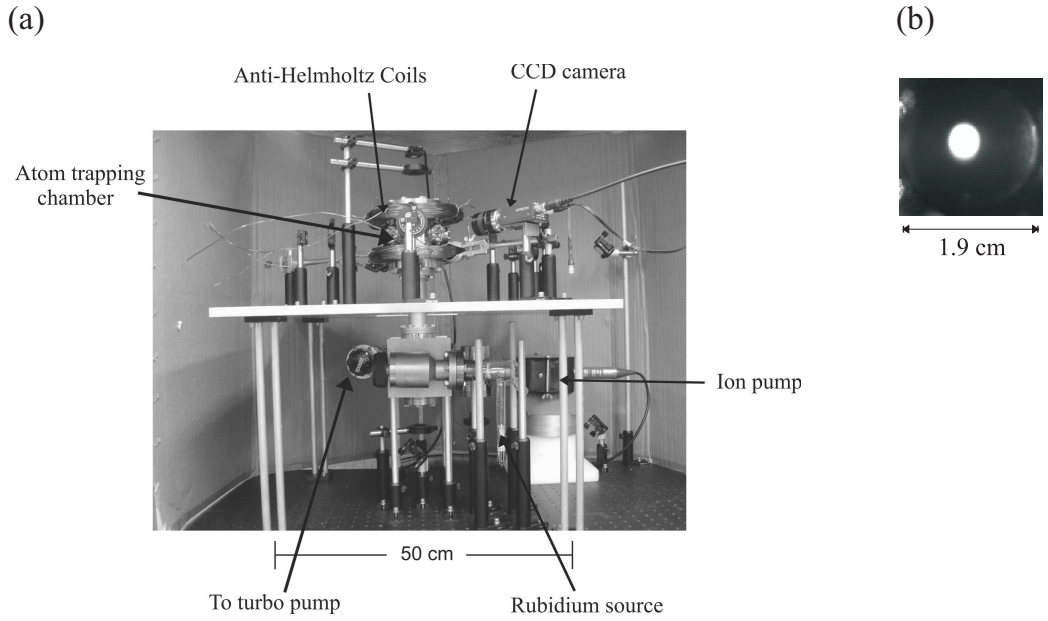

Figure A.20: (a) A portion of the atom trapping set-up. A pair of anti-Helmholtz coils is used to apply a magnetic field gradient. Two pairs of the trapping beams are aligned in the horizontal plane between the anti-Helmholtz coils. An orthogonal trapping beam is aligned along the vertical. (b) Image of trapped ^{85}Rb atoms recorded by a CCD camera. An optimized trap has a $1/e^2$ cloud radius of $\sim$1 mm and holds $\sim 10^7$ atoms. The CCD image of the trap in part (b) is saturated, thereby causing blooming.

atom trapping. The vacuum system is initially pumped down using a turbo pump and baked at $\sim$100°C for a few weeks so that the base pressure is $\sim 10^{-9}$ Torr at the end of the bake-out. The turbo pump is then disconnected and an ion pump with a pumping speed of 8 litres per second is used to maintain the vacuum. The Rb source consists of a sealed ampoule that is fused to a glass-to-metal adapting flange. The Rb source can be fabricated in a glass shop using a commercially-available ampoule and a glass-to-metal adapter. The seal can be broken in vacuum by using a magnet to manipulate a glass-enclosed magnetic striker. During the atom trapping experiments, the typical vapour pressure of Rb atoms in this chamber is $\sim 5 \times 10^{-8}$ Torr.

The number of atoms that can be accumulated in a MOT can be optimized by maximizing the laser-cooling force and the atom-trapping force. The trapping beam diameter, which is set by the available power and laser detuning, determines the laser-cooling force [107]. Typically, the atom-trapping force can be maximized under conditions in which the Zeeman shift is comparable to the Doppler shift. For ^{85}Rb atoms, this is achieved using a magnetic field gradient of $\sim$10 G/cm. The anti-Helmholtz coils of the MOT shown in Fig. A.20(a) (diameter $\sim$20 cm, $\sim$140 turns) can produce the required magnetic field gradient with an operating current of $\sim$5 A. The coils can be constructed by winding magnet wire on a plastic or metal frame.

For a multi-level atom such as ^{85}Rb exposed to a high-intensity laser beam, the laser-cooling force is maximized [108] for a trap laser detuning of $\sim$ 15 MHz below

the $F = 3 \rightarrow F' = 4$ cycling transition [see Fig. A.1(a)]. A second (repump) laser is tuned to the $F = 2 \rightarrow F' = 3$ transition to optically pump atoms out of the $F = 2$ ground state. The recommended power in the trapping laser is > 50 mW. For a trapping beam with 50 mW of power and a diameter of $\sim$1 cm, we find that a repump laser power of $\sim$1 mW is sufficient. We find that the experiments described in the next section of this dissertation can be carried out without the need to actively lock the repump laser due to the power available ($\sim$50 mW). However, the repump laser frequency is carefully monitored to ensure that it coincides with the resonant frequency. The number of trapped atoms can be maximized if the repump laser is combined with the trapping beams along all three axes using polarizing beam splitters. However, it is possible to operate the MOT even if the repump laser is aligned along a separate axis through the center of the chamber.

The trapping laser is aligned along three orthogonal directions of the trapping chamber using polarizing cube beam splitters and $\lambda/2$ wave-plates to control the relative intensities in each direction. At the entrance to the trapping chamber, each incident beam is circularly polarized using a $\lambda/4$ wave-plate and aligned through the centers of the view-ports. After passing through the chamber, each beam is directed through another $\lambda/4$ wave-plate and retro-reflected. This alignment ensures that the polarization of the MOT laser beams is set to a σ^+–σ^- configuration along each orthogonal direction. The incident and retro-reflected beams have opposite angular

momentum with respect to the axis defined by the incident beam. Due to quantum mechanical selection rules, these beams drive atomic transitions between hyperfine states with magnetic quantum numbers that differ by $\Delta m_F = \pm 1$, provided that the quantization axis is collinear with the axis of propagation.

Maxwell's equations ensure that the magnetic field gradients along the three orthogonal directions satisfy the condition that $\nabla \cdot B = 0$. Therefore, it is necessary to ensure that two of the incident trapping beams in the horizontal plane have the same angular momentum due to cylindrical symmetry. The third incident beam (along the vertical axis in this case) is set with the opposite angular momentum. The orientations of the first $\lambda/4$ wave-plate in each of the incident beams should be set carefully to ensure circular polarization. However, the σ^+–σ^- configuration for a MOT can be achieved for any orientation of the second $\lambda/4$ wave-plate.

The MOT is formed at the location where the magnetic field is zero. Therefore, it is important to align the anti-Helmholtz coils so that the field is zero at the center of the apparatus. It is also important to ensure that the laser beams are centred at this location. Ideally, the Earth's magnetic field, which shifts the position of zero field, should be cancelled at the center of the chamber using three pairs of Helmholtz coils. However, cancellation of ambient fields is generally not required in an instructional experiment.

We have described the standard configuration used for a vapour-cell loaded MOT

[109], in which the repump laser is derived from a separate diode laser. Other possible configurations include a system of pyramidal mirrors that ensure the MOT is automatically aligned if the incident beams are directed along the appropriate axis [110]. It is notable that miniaturized vacuum chambers using epoxied glass sheets have been used [111]. It is also possible to introduce an EOM in the trapping laser to generate a side-band that corresponds to the repump transition frequency.

We now provide a step-wise description of the stages involved in the Atom Trapping experiment. A small fraction of laser light is required for setting up saturated absorption for both trap and repump lasers. The repump laser is tuned to resonance with the $F = 2 \rightarrow F' = 3$ transition in ^{85}Rb. The trap laser is locked to the peak of a crossover transition $\sim$ 60 MHz below the $F = 3 \rightarrow F' = 4$ transition in ^{85}Rb [see Fig. A.1(c)]. Most of the trap laser light is aligned through a single-pass AOM operating with a frequency up-shift of $\sim$45 MHz so that the laser frequency of the diffracted beam is $\sim$ 15 MHz below the $F = 3 \rightarrow F' = 4$ resonance. The diffracted beam serves as the trapping laser, and it can be conveniently amplitude modulated using the AOM. This beam is combined with the repump laser using a polarizing beam splitter. The combined beams are split into three paths and aligned through the vacuum chamber. Ideally, the retro-reflected beams should be aligned collinear within a few milliradians with respect to the incident beams. Spatial filtering of the beams using fibers can result in a significant increase in the number of trapped atoms.

However, we avoid the use of fibers since there is a 50% reduction in laser power and increased experimental complexity. The polarization of the three orthogonal trapping laser beams can be conveniently determined throughout the beam paths by measuring the optical transmission through a rotating polarizer.

The next step involves the calibration and alignment of the anti-Helmholtz coils. The Rb source is gently heated so that the fluorescence associated with laser beams passing through the vacuum chamber is visible on a monitor or on a hand-held viewscope sensitive to near-infrared light. If the frequencies of the lasers are adequately controlled and the optical alignment is satisfactory, a MOT can be observed with very few permutations to the experimental configuration. These involve switching the polarization state of the vertical trapping beams between two orthogonal circular polarizations and reversing the direction of current through the anti-Helmholtz coils.

A.2.1 Experiments with laser-cooled atoms

After optimizing the MOT, a number of straightforward experiments relating to the properties of cold atoms are carried out. All these experiments can be performed by monitoring the fluorescence of the MOT using a PMT or amplified photodiode and determining the cloud radius using steady-state images captured by the CCD camera, similar to Fig. A.20(b). Examples include tuning the lasers to trap ^{85}Rb and ^{87}Rb isotopes, studying the atom number as a function of the magnetic field

gradient and laser frequency, measuring the atom number and atomic density using the trap fluorescence and cloud radius, determining the temperature of trapped atoms and gravitational acceleration by photographing the ballistic expansion of the trapped cloud, investigating optical pumping by turning off either the trap or repump lasers, measuring the effect of collisions from the loading rate of the trap, probe-laser spectroscopy, and investigation of the spring constant of the trap. We now review a selection of the aforementioned experiments using ^{85}Rb atoms.

Fig. A.21(a) shows the steady-state atom number, N_{ss}, as a function of trap laser power for a fixed trap laser detuning and trapping beam diameter. The experiment is carried out with trap laser intensities that are significantly larger than the saturation intensity $I_{\rm sat}$ for ^{85}Rb atoms ($I_{\rm sat} = 1.67$ mW/cm^2 for the $F = 3, m_F = 3 \rightarrow F' = 4, m_{F'} = 4$ transition). Under these conditions, it has been predicted that the optimal detuning should be $\Delta = -2.5\Gamma$ [108, 107], which is the value used in this experiment. The data shows that the atom number saturates as the trap laser power is increased. This is a result of the excited-state population saturating for intensities $I \gg I_{\rm sat}$. The ratio $I/I_{\rm sat}$ can be used to quantify the radiation pressure force on atoms.

To understand the steady-state atom number, we note that the MOT operates by slowing and trapping atoms in the low velocity tail of the speed distribution of the background Rb vapour. The trapping beam diameter determines the maximum velocity of atoms (the capture velocity, v_c) that can be trapped. The steady-state

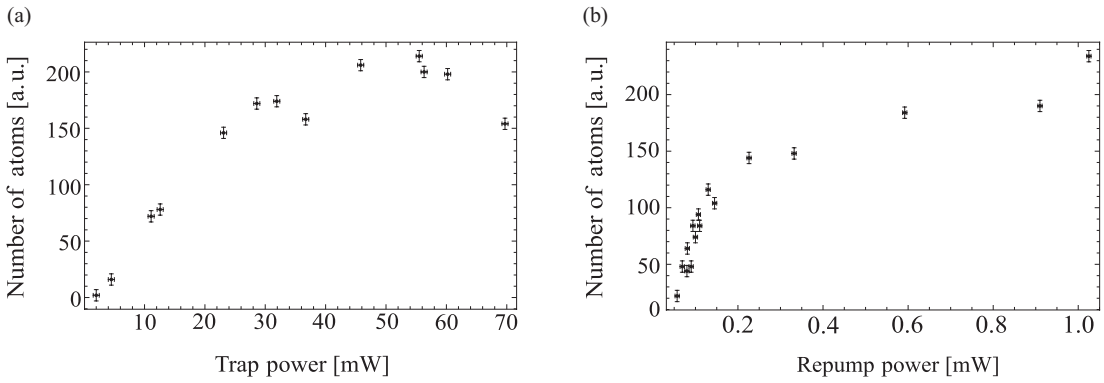

Figure A.21: (a) Steady-state atom number as a function of trap laser power. The atom number is inferred by recording the trap fluorescence on a photodiode. The voltage recorded by the detector can be converted into atom number. The maximum voltage corresponds to an atom number of $\sim 10^7$. Since the trap laser is retro-reflected through the vacuum chamber, the laser power incident on the atoms is approximately twice the trap laser power. (b) Atom number as a function of repump laser power. For both of these experiments, the trap laser detuning was fixed at 15 MHz below resonance, the trapping beam diameter was $\sim$0.90 cm, and the magnetic field gradient was ~ 7 G/cm.

atom number is related to the capture velocity through $N_{ss} = (d^2/\sigma)(v_c/u)^4$ [112, 113], where d is the diameter of the trapping beams, σ is the cross-section for collisions with "hot" background atoms, and u is the most probable speed of the background atoms ($u \sim 242$ m/s for ^{85}Rb at $T = 300$ K).

The repump laser is combined with the trapping laser along all three orthogonal directions. Fig. A.21(b) shows N_{ss} as a function of the repump laser power. Under these conditions, atoms can be cooled over the entire volume of Rb vapour that is illuminated by both trap and repump lasers. The data shows that the atom number saturates with an increase in repump laser power, thereby confirming that the atom number is not limited by repump laser intensity. Under these conditions, the experiment achieves complete optical pumping out of the $F = 2$ ground state.

For dilute traps (optical depth less than unity), photons that are absorbed and emitted by trapped atoms are not re-absorbed by other trapped atoms. Under these conditions, the density of the trap should increase as the atom number is increased [103]. As radiation trapping becomes important, the density of the cloud is expected to saturate, indicating that the cloud volume increases with an increase in atom number due to the outward pressure from re-scattered photons [114]. The data in Fig. A.22 is consistent with these expectations. Here, the atom number is varied by changing the trap laser power. Fig. A.22 also shows that the data is independent of repump laser power. The average density is calculated by combining the atom number

measured from trap fluorescence and the cloud radius measured using a CCD camera. Since the trap density is relatively low, the power requirements for the repump are very modest.

It is possible to obtain atom numbers of $\sim 10^9$ by using larger trapping beam diameters. Under these conditions, it is possible to observe a "bounce trap" [115] if the repump laser intensity is lowered. In this situation, the repump light is highly attenuated at the center of the cloud due to absorption. Only atoms in the outer shell that are cycled on the $F = 3 \rightarrow F' = 4$ transition by the trapping laser contribute to the trap fluorescence, leaving the atoms at the center of the cloud predominantly optically pumped into the $F = 2$ ground state. As a consequence, the trap fluorescence can scale linearly as a function of the surface area of the cloud. In contrast, if the repump laser intensity is large, the trap fluorescence can scale linearly with the cloud volume. However, to study these trends, it is important to consider a suitable method of changing the steady-state atom number without independently changing the cloud size.

The capture velocity for a MOT is a non-linear function of the trapping beam diameter. As a consequence, the atom number is predicted to scale as d^x, where d is the trapping beam diameter, and x typically ranges from $\sim$3 to 4 [113, 107]. The variation in x arises because the atom number must be optimized for a given trapping-beam diameter by varying the detuning, trap laser intensity, and magnetic field gradient.

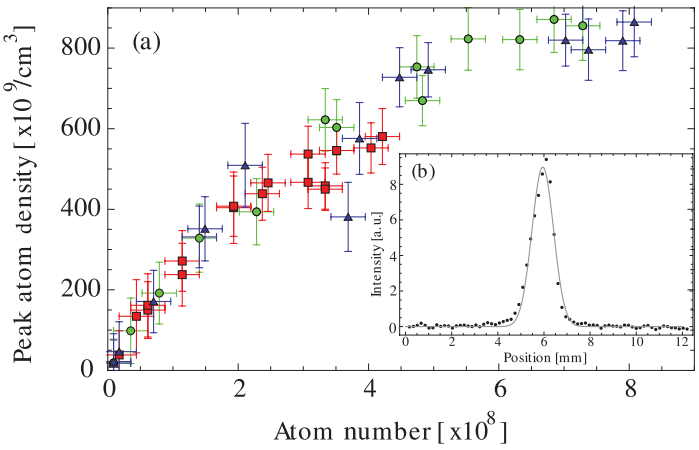

Figure A.22: Variation in average density as a function of atom number. The atom number, inferred from trap fluorescence, was varied by changing the trap laser power. The trap laser detuning was fixed at 15 MHz below resonance, the trapping beam diameter was ~ 0.90 cm, and the magnetic field gradient was ~ 7 G/cm. Three different repump laser powers were used: (0.6 ± 0.06) mW (red squares), (1.0 ± 0.1) mW (green circles), and (50 ± 5) mW (blue triangles). The cloud radius was determined from fits along two dimensions that were summed in quadrature. (b) Spatial profile of the cloud obtained from a CCD camera image for a trap laser power of (75 ± 7) mW, repump laser power of (50 ± 5) mW, and a magnetic field gradient of ~ 7 G/cm. The vertical axis represents the intensity obtained by integrating pixel values. A Gaussian fit gives a $1/e^2$ cloud radius of (0.66 ± 0.01) mm.

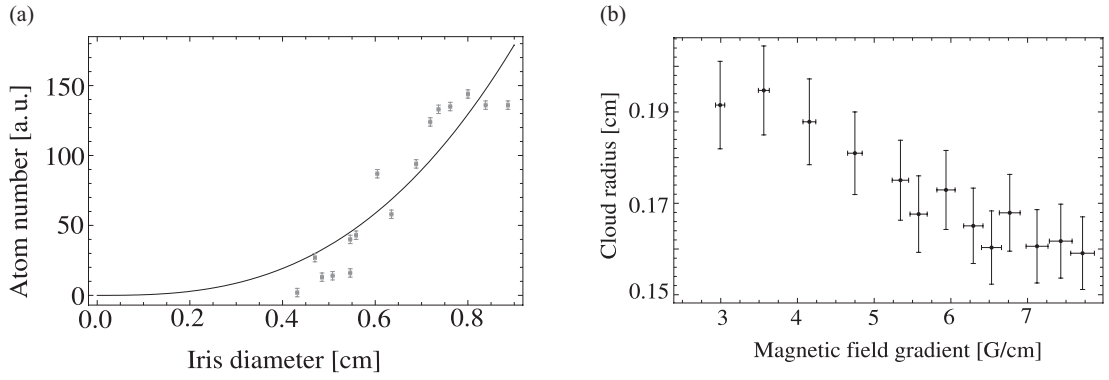

Figure A.23: (a) Atom number as a function of iris diameter, d. The data shows a sensitive dependence on the beam size. For a well-aligned trap and a well-centred iris, the atom number can be expected exhibit a power-law dependence shown by the solid line. For this experiment, the trap detuning was set to 15 MHz below resonance, the trap laser power was ~ 65 mW, the repump laser power was set at ~ 15 mW, and the magnetic field gradient was ~ 7 G/cm. (b) Cloud radius (1/e) as a function of magnetic field gradient along the vertical direction. For this data, the trap laser power was fixed at ~ 75 mW and the trap laser detuning was ~ 15 MHz below resonance with a beam diameter of ~ 1.0 cm. The repump power was $\sim$12 mW.

The sensitive dependence of the atom number on the trapping-beam diameter can be studied by varying the size of an aperture that is centred on the trapping beam. Fig. A.23 shows a strong dependence of the atom number on beam diameter. The atom number falls to zero for a finite beam diameter due to misalignment.

For a small atom number, the linear variation of the density with atom number in Fig. A.22(a) suggests that radiation trapping does not affect the cloud radius for

this data set. As a result, we assume that the temperature of the trapped atoms is not affected by the absorption of re-scattered photons [103]. Careful measurements of the temperature in reference [103] suggest that the effects of radiation trapping influence the temperature even in the linear regime.

If the temperature is assumed constant, the equipartition theorem can be used to argue that the cloud radius should scale as $\sqrt{1/(dB/dz)}$ [103, 116]. This is because $k_B T = k_s r^2$, where k_s is the spring constant of the trap (which is directly proportional to the magnetic field gradient [108]) and r represents the cloud radius. Although it can be challenging to confirm the predicted trend, typical data shown in Fig. A.23(b) qualitatively confirms expectations that the cloud radius decreases monotonically with increasing magnetic field gradient. This is because the stiffness of the trap is proportional to the magnetic field gradient. For an optimally-aligned trap, the position of the centroid of the cloud should not change when the magnetic field gradient is increased. Therefore, studies as a function of magnetic field gradient are also useful as a test of alignment.

Fig. A.24 shows the decay of the fluorescence from the trap after turning off the repump light reaching the trap using an AOM. The AOM has a switching time of < 1 μs. The decay represents optical pumping to the $F = 2$ ground state. Atoms in this state do not interact with the trap laser. The data is fitted to an exponential decay to determine the optical pumping time. The value obtained from the fit is

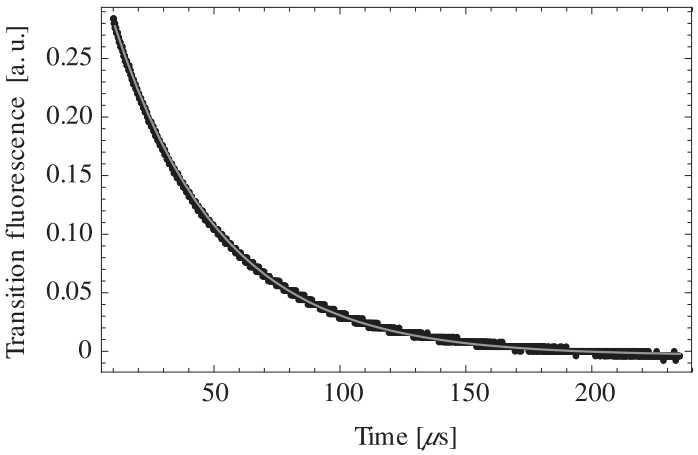

Figure A.24: Fluorescence from the $F = 4 \rightarrow F' = 3$ transition as a function of time after blocking the repump laser. An exponential fit gives a time constant for the decay of (42.42 ± 0.05) μs. The trap laser power was (75 ± 7) mW, the repump power was (50 ± 5) mW, and the magnetic field gradient was ~ 7 G/cm.

consistent with the expected time for optical pumping based on a three-level model. This data is a clear signature of optical pumping, as the time scale for atoms to leave the trapping volume is much longer. This experiment also illustrates the importance of using a repump laser. An important precaution for this experiment is that the time for shutting off the repump laser must be much shorter than the optical pumping time.

Fig. A.25(a) shows a measurement of the loading time of the trap obtained with a separate set-up. To record this data, the magnetic field gradient was initially turned off, with the trap and repump lasers on. In this manner, the trapped atoms were allowed to escape from the trapping volume. The magnetic field gradient was then

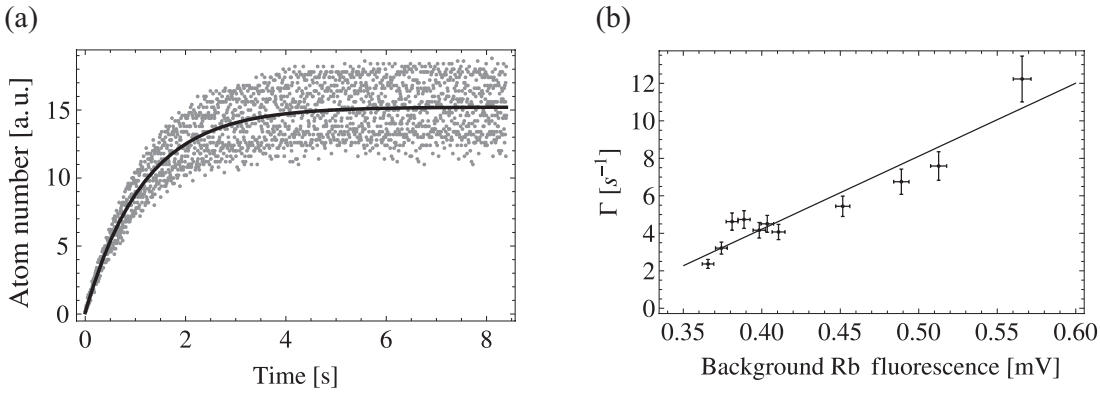

Figure A.25: (a) Loading curve for the MOT. The data was recorded for a fixed n_{Rb}. A fit to the functional form described in text gives $\Gamma^{-1} = (1.17 \pm 0.03)$ s. (b) Variation of the collisional rate with background fluorescence, which is proportional to n_{Rb}.

turned on and the atom number was recorded as a function of time. Alternatively, the magnetic field gradient and repump lasers can be left on, and the trap laser can be amplitude modulated. This approach makes it easier to trigger the experiment. However, it is necessary introduce an RF switch and pulse generator for amplitude modulation.

The loading rate of a vapour-cell loaded MOT can be modelled by a differential equation of the form $dN/dt = R - \Gamma N$ [109]. Here, N is the atom number, $R = n_{\mathrm{Rb}} d^2 v_c^4 / u^3$ is the capture rate of atoms from the background, n_{Rb} is the background density of Rb atoms, and Γ is the collisional rate of cold atoms with background Rb vapour. This equation assumes that there are no collisions between cold Rb atoms that can also result in a change in the atom number. The solution to this differential

equation is $N(t) = N_{ss}(1 - e^{-\Gamma t})$, where $N_{ss} = R/\Gamma$ is the steady-state atom number. The data shown in Fig. A.25(a) is well modelled by $N(t)$. The collisional rate Γ can be extracted by fitting the data to the prediction for $N(t)$.

Loading curves such as those shown in Fig. A.25(a) can be recorded for different background Rb densities by varying the temperature of the Rb source. Since Rb has an appreciable vapour pressure at room temperature (3×10^{-7} Torr) and since the melting point of Rb is 312.5 K, only a small variation in the temperature of the Rb source is required to affect a significant change in the background density. Fig. A.25(b) shows that the collisional rate is a linear function of the background Rb density, n_{Rb}. The relative density was monitored by measuring the fluorescence at the center of the cell. The measured trend is consistent with expectations, since the variation of Γ as a function of density can be described by $\Gamma = n_{\mathrm{Rb}}\sigma v_{\mathrm{rel}}$. Here, σ is the cross-section for collisions between background and laser-cooled Rb atoms, and v_{rel} is the relative velocity between colliding atoms.

It is also an interesting exercise to monitor N_{ss} as a function of the change in background fluorescence due to an increase in the temperature of the Rb source. For low background density, N_{ss} increases because the increase in the capture rate R is larger than the increase in the collisional rate Γ. As the background density increases further, the trap loads faster, and N_{ss} can be observed to decrease.

If the MOT is carefully aligned, it is possible to observe an optical molasses due

to the damping force of the laser beams by turning off the magnetic field gradient. Fig. A.26(a) shows the molasses decay time for typical operating conditions. The decay is monitored by recording the fluorescence associated with cold atoms after the magnetic field gradient is turned off. The relatively fast decrease in trap fluorescence is primarily due to imbalances in the forces due to trapping beams and the failure to cancel background magnetic fields. Typically, the molasses decay time can be extended to several seconds by improving the alignment and cancelling background magnetic fields such as the Earth's field. For these reasons, monitoring the molasses decay time can be a sensitive test of MOT alignment. This experiment was carried out by turning off the power supply driving the anti-Helmholtz coils. The time constant for turning off the current is determined primarily by the self-inductance of these coils. However, this time scale is generally much smaller than the time constant associated with molasses decay. It should be noted that in research labs, magnetic field gradients can be turned off on sub-millisecond time scales using field effect transistors (FETs) or insulated gate bipolar transistors (IGBTs).

Fig. A.26(b) shows a measurement of the temperature of the trap using the release and re-capture technique [117]. With the repump laser and magnetic field gradient on, the trap laser is pulsed off, allowing atoms to leave the central region of the MOT before the remaining atoms are recaptured by the trap light turning back on. The atom number remaining in the central region is measured by varying the "off" time

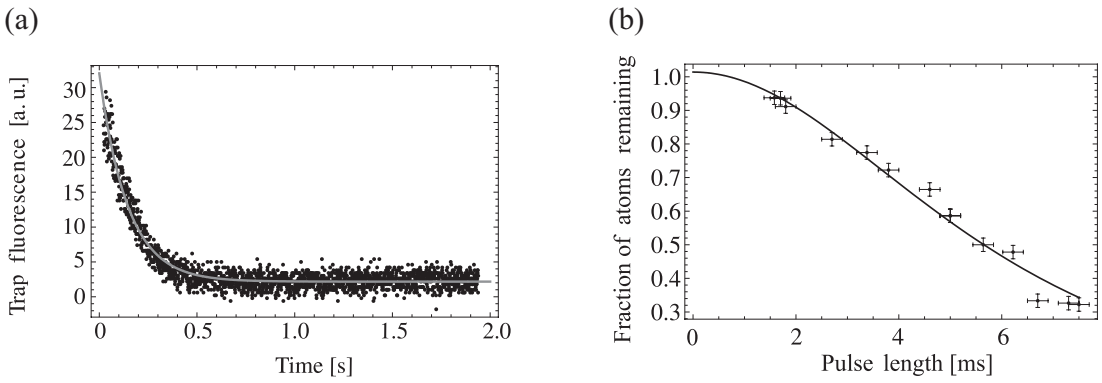

Figure A.26: (a) Measurement of the optical molasses decay time. A fit to a decaying exponential gives a $1/e$ time constant of (0.165 ± 0.002) s. (b) Measurement of the temperature of trapped atoms using the release and re-capture method. The vertical axis represents the fraction of re-captured atoms. The horizontal axis is the free-expansion time. A determination of the most probable speed u from the fit gives a temperature $T = (420 \pm 20)\ \mu$K.

of trap laser light and recording the fluorescence at the time of trap laser turn on. For this experiment, the central region is carefully imaged on an optical detector. Ideally, the repump laser and the magnetic field gradient should also be turned off. However, it is not critical to do so since these parameters have a small effect on the temperature. Turning off the magnetic field gradient and repump laser requires additional equipment. The temperature of the trapped atoms, T, is determined by fitting to an expression of the form $[R_d/R(t)]^3$, where $R(t) = \sqrt{R_0^2 + (ut)^2}$. Here, R_d is the radius of the detection volume, R_0 is the initial cloud radius, $u = \sqrt{2k_BT/M}$ is the most probable speed, and M is the atomic mass. A more complete expression for $R(t)$ can be derived on the basis of references [118, 119].

We note that there are several methods for measuring the temperature of the trapped atoms. For example, references [118, 119] describe time-of-flight techniques used in references [103, 116]. However, these experiments require additional lasers, changes in alignment, and synchronized timing for CCD imaging. Therefore, we find that the release and re-capture technique is generally best suited for an instructional environment.

MOTs are also well suited for several additional experiments including trapping ^{87}Rb and spectroscopy of cold atoms. Absorption spectroscopy can be carried out by scanning the frequency of a probe laser across Rb resonances and comparing it with the saturated absorption spectrum at room temperature. Alternatively, fluorescence

measurements can be carried out by slowly sweeping the trap laser across resonance after the atoms have been trapped.

B Research contributions

B.1 Papers

1. Development of a technique for precise determination of atomic lifetimes based on photon echoes, H. C. Beica, A. Pouliot, P. Dowling, A. Carew, T. Vacheresse, G. Carlse, L. Marmet, A. Kumarakrishnan, Submitted , Physical Review A (2019).

2. Characterization and applications of auto-locked vacuum sealed diode lasers for precision metrology, H. C. Beica, A. Pouliot, A. Carew, A. Vorozcovs, N. Afkhami-Jeddi, T. Vacheresse, G. Carlse, P. Dowling, B. Barron, A. Kumarakrishnan, Accepted, Review of Scientific Instruments (2019).

3. Laboratory Courses on laser spectroscopy and atom trapping, H. C. Beica, S. Winter, C. Mok, B. Barrett, R. Berthiaume, A. Vorozcovs, F. Yachoua, N. Afkhami-Jeddi, M. Aggarwal, A. Pouliot, G. Carlse, K. Borsos, R. Marants, and A. Kumarakrishnan, Submitted, Physics in Canada (2019).

4. An auto-locked laser system for precision metrology and lidar applications, H. C. Beica, A. Carew, A. Vorozcovs, P. Dowling, A. Pouliot, B. Barron, and A. Kumarakrishnan, Proc. SPIE 10191, Laser Radar Technology and Applications XXII, 101910K (2017).

5. An Auto-Locked Diode Laser System for Precision Metrology, H. C. Beica, A. Carew, A. Vorozcovs, P. Dowling, A. Pouliot, G. Singh, and A. Kumarakrishnan, Proc. SPIE 1008610, High-Power Diode Laser Technology XV, 100860W (2017).

6. Investigations of optical pumping for magnetometry using an auto-locking laser system, A. Pouliot, H. C. Beica, A. Carew, A. Vorozcovs, G. Carlse, B. Barrett (U. Bordeaux), and A. Kumarakrishnan, Proc. SPIE, 10637, Laser Technology for Defense and Security XIV, 106370A (2018).

7. Auto-locking waveguide amplifier system for lidar and magnetometric applications, A. Pouliot, H. C. Beica, A. Carew, A. Vorozcovs, G. Carlse, A. Kumarakrishnan, Proc. SPIE 10514, High-Power Diode Laser Technology XVI, 105140S (2018).

8. Comparative investigations of magnetometers based on atomic populations and coherences, A. Pouliot, G. Carlse, H. C. Beica, T. Vacheresse, and A. Kumarakrishnan, In Preparation, Physical Review A (2019).

9. Characterization of micro-scale particles in free-space optical dipole force traps, G. Carlse, K. Borsos, H. C. Beica, J. Perez-Garcia, A. Pouliot, L. Marmet, and A. Kumarakrishnan, In Preparation, Journal of Applied Physics (2019).

10. Prospects for precise measurements with echo atom interferometry, B. Barrett, A. Carew, H. C. Beica, A. Vorozcovs, A. Pouliot, and A. Kumarakrishnan, Atoms, 4, 19 (2016), MDPI, Special Issue on Atom Interferometry (42 pages) (Edited by James F. Babb) (Invited).

11. Technique for magnetic moment and mangetic-state reconstruction of laser-cooled atoms using direct imaging, G. Carlse, A. Pouliot, T. Vacheresse, A. Carew, H. C. Beica, S. Winter, and A. Kumarakrishnan, Submitted, Phys. Rev. A (2019).

B.2 Conference abstracts

1. Precise determination of atomic lifetimes based on optical photon echoes, H. C. Beica, A. Pouliot, P. Dowling, A. Carew, T. Vacheresse, G. Carlse, L. Marmet, and A. Kumarakrishnan, Frontiers in Optics/Laser Science OSA Meeting, Washington D. C., September 2019.

2. Characterization and applications of auto-locked vacuum-sealed diode lasers for precision metrology, H. C. Beica, A. Pouliot, A. Carew, A. Vorozcovs, N.

Afkhami-Jeddi, T. Vacheresse, G.Carlse, P. Dowling, B. Barron, and A. Kumarakrishnan, Frontiers in Optics/Laser Science OSA Meeting, Washington D. C., September 2019.

3. Applications of auto-locked laser systems for precision metrology, H. C. Beica, A. Pouliot, A. Carew, A. Vorozcovs, P. Dowling, G. Carlse, B. Barron, and A. Kumarakrishnan, Proc. CAP Congress, Physics in Canada 74 (2A), page 65, 2018.

4. Auto-locked laser systems for precision metrology, H. C. Beica, A. Carew, A. Vorozcovs, P. Dowling, A. Pouliot, G. Singh, and A. Kumarakrishnan, SPIE Photonics West, San Francisco, January 2017.

5. An auto-locked laser system for precision metrology and lidar applications, H. C. Beica, A. Carew, A. Vorozcovs, P. Dowling, A. Pouliot, B. Barron, and A. Kumarakrishnan, SPIE DCS Defense + Security, Anaheim, April 2017.

6. Applications of auto-locked diode lasers, H. C. Beica, A. Carew, A. Vorozcovs, P. Dowling, A. Pouliot, B. Barron, and A. Kumarakrishnan, Canadian-American-Mexican Graduate Student Physics Conference, Washington DC, August 2017.

7. Free-space optical tweezers, S. Jackson, H. Beica, P. Dowling and A. Kumarakrishnan, CUPC, Kingston, October 2014.

8. New experiments in atomic and laser physics for undergraduate students, H. Beica, B. Barrett, C. Mok, A. Vorozcovs, A. Sibilia, H. Morrison, and A. Kumarakrishnan, CUPC, Halifax, October 2010.

9. Auto-locking waveguide amplifier system for lidar and magnetometric applications, A. Pouliot, H. C. Beica, A. Carew, A. Vorozcovs, G. Carlse and A. Kumarakrishnan, SPIE Photonics West, San Francisco, January 2018.

10. Auto-locking diode laser system for lidar and magnetometric applications, A. Pouliot, H. C. Beica, A. Carew, A. Vorozcovs, G. Carlse, B. Barrett and A. Kumarakrishnan, SPIE Defense + Commercial Sensing, Orlando, April 2018.

11. Comparative investigations of magnetometers based on atomic populations and coherences, A. Pouliot, G. Carlse, H. C. Beica, T. Vacheresse, and A. Kumarakrishnan, Conference on Coherence and Quantum Optics, Rochester, August 2019.

12. Development of a high-power pulsed laser system, G. Carlse, A. Pouliot, H. C. Beica, A. Carew, A. Vorozcovs, B. Baron and A. Kumarakrishnan, CUPC, Ottawa, October 2017.

13. A Review of the Allan variance and its applications, B. Barron, G. Carlse, H. Beica, A. Pouliot, and A. Kumarakrishnan, CUPC, Halifax, October 2016.

14. Design and construction of semiconductor waveguide amplifiers for atomic physics experiments, G. Carlse, A. Pouliot, H. Beica and A. Kumarakrishnan, CUPC, Halifax, October 2016.

15. Development of a home-built tapered amplifier laser system, G. Carlse, A. Pouliot, H. Beica, G. Singh, A. Schiff-Kearn, S. Jackson, J. Goobie and A. Kumarakrishnan, CUPC, Peterborough, October 2015.

16. Applications of high-speed data acquisition in atomic physics experiments, P. Dowling, A. Vorozcovs, H. Beica, A. Carew and A. Kumarakrishnan, CUPC, Kingston, October 2014.

17. Atom trapping laboratory for upper-level undergraduate students, C. Mok, S. Winter, H. Beica, B. Barrett, R. Berthiaume, A. Vorozcovs, F. Yachoua, N. Afkhami-Jeddi, R. Marants, M. Aggarwal and A. Kumarakrishnan, DAMOP, Anaheim, June 2012.

18. Free-space optical trapping of colloidal ink droplets, J. Perez, B. Barron, G. Carlse, H. Beica, A. Pouliot and A. Kumarakrishnan, CUPC, Halifax, October 2016.

19. Technique for in-situ measurement of magnetic sublevel populations in a magneto-optical trap based on free-expansion imaging, G. Carlse, A. Pouliot, T. Vacher-

esse, A. Carew, H. C. Beica, and A. Kumarakrishnan, Conference on Coherence and Quantum Optics, Rochester, August 2019.

20. Free-space optical trapping of colloidal ink droplets, J. Perez-Garcia, G. Carlse, B. Barron, K. Borsos, H. Beica, A. Pouliot and A. Kumarakrishnan, CUPC, Ottawa, October 2017.

Bibliography

[1] B. Barrett, A. Carew, H. C. Beica, A. Vorozcovs, A. Pouliot, and A. Kumarakrishnan. Prospects for precise measurements with echo atom interferometry. *Atoms*, 4(3), 2016.

[2] H. C. Beica, A. Pouliot, A. Carew, A. Vorozcovs, N. Afkhami-Jeddi, T. Vacheresse, G. Carlse, P. Dowling, B. Barron, and A. Kumarakrishnan. Characterization and applications of auto-locked vacuum-sealed diode lasers for precision metrology. *Rev. Sci. Intrum.*, 90(8):085113, 2019.

[3] H. C. Beica, A. Carew, A. Vorozcovs, P. Dowling, A. Pouliot, G. Singh, and A. Kumarakrishnan. An auto-locked diode laser system for precision metrology. *Proc. SPIE*, 10086:100860W, 2017.

[4] H. C. Beica, A. Carew, A. Vorozcovs, P. Dowling, A. Pouliot, B. Barron, and A. Kumarakrishnan. An auto-locked diode laser system for precision metrology and lidar applications. *Proc. SPIE*, 10191:101910K, 2017.

[5] A. Pouliot, H. C. Beica, A. Carew, A. Vorozcovs, G. Carlse, and A. Kumarakrishnan. Auto-locking waveguide amplifier system for lidar and magnetometric applications. *Proc. SPIE*, 10514:105140S, 2018.

[6] A. Pouliot, H. C. Beica, A. Carew, A. Vorozcovs, G. Carlse, B. Barrett, and A. Kumarakrishnan. Investigations of optical pumping for magnetometry using an auto-locking laser system. *Proc. SPIE*, 10637:106370A, 2018.

[7] A. Pouliot, G. Carlse, H. C. Beica, T. Vacheresse, and A. Kumarakrishnan. Comparative investigations of magnetometers based on atomic populations and coherences. *Phys. Rev. A*, In preparation, 2019.

[8] G. Carlse, A. Pouliot, T. Vacheresse, A. Carew, H. C. Beica, and A. Kumarakrishnan. Technique for in-situ measurement of magnetic sublevel populations in a magneto-optical trap based on free-expansion imaging. *Opt. Lett.*, In preparation, 2019.

[9] X. Baillard, A. Gauguet, S. Bize, P. Lemonde, Ph. Laurent, A. Clairon, and P. Rosenbusch. Interference-filter-stabilized external-cavity diode lasers. *Opt. Comm.*, 266:609–613, 2006.

[10] M. Gilowski, Ch. Schubert, M. Zaiser, W. Herr, T. Wubbena, T. Wendrich, T. Muller, E. M. Rasel, and W. Ertmer. Narrow bandwidth interference filter-

stabilized diode laser systems for the manipulation of neutral atoms. *Opt. Comm.*, 280:443–447, 2007.

[11] W. J. Riley. Handbook of frequency stability analysis. *NIST*, 1065:1–123, 2007.

[12] C. E. Wieman and L. Hollberg. Using diode lasers for atomic physics. *Rev. Sci. Instrum.*, 62(1):1–20, 1991.

[13] A. C. Carew. *Apparatus for inertial sensing with cold atoms.* PhD thesis, York University, 2018.

[14] G. Carlse, K. Borsos, H. C. Beica, J. Perez-Garcia, A. Pouliot, L. Marmet, and A. Kumarakrishnan. Characterization of micro-scale particles in free space optical dipole force traps. *Journal of Appl. Phys.*, In preparation, 2019.

[15] H. C. Beica, S. Winter, C. Mok, B. Barrett, R. Berthiaume, A. Vorozcovs, F. Yachoua, N. Afkhami-Jeddi, M. Aggarwal, A. Pouliot, G. Carlse, K. Borsos, R. Marants, and A. Kumarakrishnan. Laboratory courses on laser spectroscopy and atom trapping. *Phys. in Canada*, Submitted, 2019.

[16] J. Perez-Garcia, G. Carlse, B. Barron, K. Borsos, H. Beica, A. Pouliot, and A. Kumarakrishnan. Free-space optical trapping of colloidal ink droplets. Canadian Undergraduate Physics Conference, Ottawa, 2017.

[17] J. Perez-Garcia, B. Barron, G. Carlse, H. Beica, A. Pouliot, and A. Kumarakrishnan. Free-space optical trapping of colloidal ink droplets. Canadian Undergraduate Physics Conference, Halifax, 2016.

[18] C. Mok, S. Winter, H. Beica, B. Barrett, R. Berthiaume, A. Vorozcovs, F. Yachoua, N. Afkhami-Jeddi, R. Marants, M. Aggarwal, and A. Kumarakrishnan. Atom trapping laboratory for upper-level undergraduate students. Division of Atomic, Molecular, and Optical Physics, Anaheim, 2012.

[19] S. Jackson, H. Beica, P. Dowling, and A. Kumarakrishnan. Free-space optical tweezers. Canadian Undergraduate Physics Conference, Kingston, 2014.

[20] H. Beica, B. Barrett, C. Mok, A. Vorozcovs, A. Sibilia, H. Morrison, and A. Kumarakrishnan. New experiments in atomic and laser physics for undergraduate students. Canadian Undergraduate Physics Conference, Halifax, 2010.

[21] H. C. Beica, A. Pouliot, P. Dowling, A. Carew, T. Vacheresse, G. Carlse, L. Marmet, and A. Kumarakrishnan. Development of a technique for precise determination of atomic lifetimes based on photon echoes. *Phys. Rev. A*, Submitted, 2019.

[22] C. W. Oates, K. R. Vogel, and J. L. Hall. High precision linewidth measurement of laser-cooled atoms: resolution of the Na 3p $^2P_{3/2}$ lifetime discrepancy. *Phys. Rev. Lett.*, 76:2866–2869, 1996.

[23] S. Cauchi, A. Vorozcovs, M. Weel, S. Beattie, O. Gagnon, and A. Kumarakrishnan. Absorption spectroscopy of trapped rubidium atoms. *Can. J. Phys.*, 82:905–916, 2004.

[24] U. Volz and H. Schmoranzer. Precision lifetime measurements on alkali atoms and on helium by beam-gas-laser spectroscopy. *Phys. Scr.*, T T65:48–56, 1996.

[25] J. E. Simsarian, L. A. Orozco, G. D. Sprouse, and W. Z. Zhao. Lifetime measurements of the 7p levels of atomic francium. *Phys. Rev. A*, 57:2448–2458, 1998.

[26] E. L. Hahn, N. S. Shiren, and S. L. McCall. Application of the area theorem to photon echoes. *Physics Letters*, 37A(3):265–267, 1971.

[27] I. D. Abella, N. A. Kurnit, and S. R. Hartmann. Photon echoes. *Phys. Rev.*, 141:391–406, 1966.

[28] L. Allen and J. H. Eberly. *Optical resonance and two-level atoms.* Wiley, 1975.

[29] E. L. Hahn. Spin echoes. *Phys. Rev.*, pages 580–594, 1950.

[30] E. L. Hahn. Free nuclear induction. *Physics Today*, 6:4, 1953.

[31] R. Beach, S. R. Hartmann, and R. Friedberg. Billiard-ball echo model. *Phys. Rev. A*, 25:2658, 1982.

[32] C. Affolderbach and G. Mileti. A compact laser head with high-frequency stability for Rb atomic clocks and optical instrumentation. *Rev. Sci. Instr.*, 76:073108, 2005.

[33] M. T. Hummon, S. Kang, D. G. Bopp, Q. Li, D. A. Westly, S. Kim, C Fredrick, S. A. Diddams, K. Srinivasan, V. Aksyuk, and J. E. Kitching. Photonic chip for laser stabilization to an atomic vapor with 10^{-11} instability. *Optica*, 5(4):443–449.

[34] D. Akamatsu, Y. Nakajima, H. Inaba, K. Hosaka, M. Yasuda, A. Onae, and F.-L. Hong. Narrow linewidth laser system realized by linewidth transfer using a fiber-based frequency comb for the magneto-optical trapping of strontium. *Opt. Expr.*, 20(14):16010–16016, 2012.

[35] Y. Cheng, K. Zhang, L.-L. Chen, W.-J. Xu, Q. Luo, M.-K. Zhou, and Z.-K. Hu. Low-phase noise and high-power laser for Bragg atom interferometer. *AIP Advances*, 7:095211, 2017.

[36] T. M. Niebauer, G. S. Sasagawa, J. E. Faller, R. Hilt, and F. Klopping. A new generation of absolute gravimeters. *Metrologia*, 32:159–180, 1995.

[37] D. Naughton, R. Bedington, S. Barraclough, T. Islam, D. Griffin, and B. Smith. Design considerations for an optical link supporting intersatellite quantum key distribution. *Optical Engineering*, 58:1, 2019.

[38] R. Kingsbury. *Optical communications for small satellites.* PhD thesis, Massachusetts Institute of Technology, 2015.

[39] A. S. Arnold, J. S. Wilson, and M. G. Boshier. A simple extended-cavity diode laser. *Rev. Sci. Instr.*, 69(3):1236–1239, 1998.

[40] M. G. Littman and H. J. Metcalf. Spectrally narrow pulsed dye laser without beam expander. *Applied Optics*, 17(14):2224–2227, 1978.

[41] S. Stry, S. Thelen, J. Sacher, D. Halmer, P. Hering, and M. Murtz. Widely tunable diffraction limited 1000 mW external cavity diode laser in Littman/Metcalf configuration for cavity ring-down spectroscopy. *Appl. Phys. B*, 85:365–374, 2006.

[42] T. P. Dinneen, C. D. Wallace, and P. L. Gould. Narrow linewidth, highly stable, tunable diode laser system. *Opt. Comm.*, 92:277–282, 1992.

[43] B. Dahmani, L. Hollberg, and R. Drullinger. Frequency stabilization of semiconductor lasers by resonant optical feedback. *Opt. Lett.*, 12:876, 1987.

[44] H. Chang, K. Myneni, D. D. Smith, and H. R. Liaghati-Mobarhan. High-precision, accurate optical frequency reference using a Fabry-Perot diode laser. *Rev. Sci. Instr.*, 88:063101, 2017.

[45] W. Lewoczko-Adamczyk, C. Pyrlik, J. Hager, S. Schwertfeger, A. Wicht, A. Peters, G. Erbert, and G. Trankle. Ultra-narrow linewidth DFB-laser with optical feedback from a monolithic confocal Fabry-Perot cavity. *Opt. Expr.*, 23(8):9705–9709, 2015.

[46] Q. Lin, M. A. Van Camp, H. Zhang, B. Jelenkovic, and V. Vuletic. Long-external-cavity distributed Bragg reflector laser with subkilohertz intrinsic linewidth. *Opt. Lett.*, 37(11):1989–1991, 2012.

[47] Stanford Research Systems. Model PRS10 Rubidium Frequency Standard, Dec. 2015. Ver. 1.5.

[48] B. Bernhardt, T. W. Hansch, and R. Holzwarth. Implementation and characterization of a stable optical frequency distribution system. *Opt. Expr.*, 17(19):16849–16860, 2009.

[49] K. G. Libbrecht, R. A. Boyd, P. A. Willems, T. L. Gustavson, and D. K. Kim. Teaching physics with 670 nm diode lasers - construction of stabilized lasers and lithium cells. *Am. J. Phys.*, 63(8):729–737, 1995.

[50] L. Ricci, M. Weidemuller, T. Esslinger, A. Hemmerich, C. Zimmermann, V. Vuletic, W. Konig, and T. W. Hansch. A compact grating-stabilized diode laser system for atomic physics. *Opt. Comm.*, 117:541–549, 1995.

[51] Sebastian D. Saliba, Mark Junker, Lincoln D. Turner, and Robert E. Scholten. Mode stability of external cavity diode lasers. *Appl. Opt.*, 48(35):6692–6700.

[52] A. V. Carr, Y. H. Sechrest, S. R. Waitukaitis, J. D. Perreault, V. P. A. Lonij, and A. D. Cronin. Cover slip external cavity diode laser. *Rev. Sci. Intrum.*, 78:106108, 2007.

[53] E. C. Cook, P. J. Martin, T. L. Brown-Heft, J. C. Garman, and D. A. Steck. High passive-stability laser-diode design for use in atomic-physics experiments. *Rev. Sci. Instrum.*, 83(4):043–101, 2012.

[54] F. Kunze, S. Wolf, and G. Rempe. Measurement of fast frequency fluctuations: Allan variance of a grating-stabilized diode laser. *Opt. Comm.*, 128:269–274, 1996.

[55] K. Fukuda, M. Tachikawa, and M. Kinoshita. Allan-variance measurements of diode laser frequency-stabilized with a thin vapor cell. *Appl. Phys. B*, 77:823–827, 2003.

[56] L. D. Turner, K. P. Weber, C. J. Hawthorn, and R. E. Scholten. Frequency noise characterisation of narrow linewidth diode lasers. *Opt. Comm.*, 201:391–397, 2002.

[57] D. W. Allan. Statistics of atomic frequency standards. *Proceedings of the IEEE*, 54(2):221–230, 1966.

[58] H. Talvitie, M. Merimaa, and E. Ikonen. Frequency stabilization of a diode laser to Doppler-free spectrum of molecular iodine at 633 nm. *Opt. Comm.*, 152:182–188, 1998.

[59] D. A. Steck. Rubidium 85 D Line Data, revision 2.1.4, December 2010. http://steck.us/alkalidata.

[60] K. G. Libbrecht and J. L. Hall. A low-noise high-speed diode laser current controller. *Rev. Sci. Instrum.*, 64(8):2133–2135, 1993.

[61] K. S. Repasky, A. R. Nehrir, J. T. Hawthorne, G. W. Switzer, and J. L. Carlsten. Extending the continuous tuning range of an external-cavity diode laser. *Appl. Opt.*, 45(35):9013–9020, 2006.

[62] A. Dinovitser, M. W. Hamilton, and R. A. Vincent. Stabilized master laser system for differential absorption lidar. *Appl. Opt*, 49(17):3274–3281, 2010.

[63] J. A. Whiteway, L. Komguem, C. Dickinson, C. Cook, M. Illnicki, J. Seabrook, V. Popovici, T. J. Duck, R. Davy, P. A. Taylor, J. Pathak, D. Fisher, A. I. Carswell, M. Daly, V. Hipkin, A. P. Zent, M. H. Hecht, S. E. Wood, L. K.

Tamppari, N. Renno, J. E. Moores, M. T. Lemmon, F. Daerden, and P. H. Smith. Mars water-ice clouds and precipitation. *Science*, 325(58):68–70, 2009.

[64] P. Piironen and E. W. Eloranta. Demonstration of a high-spectral-resolution lidar based on an iodine absorption filter. *Opt. Lett.*, 19(3):234–236, 1994.

[65] C. J. Grund and E. W. Eloranta. University of Wisconsin High Spectral Resolution Lidar. *Optical Engineering*, 30(1):6–12, 1991.

[66] G. Spirou, I. Yavin, M. Weel, A. Vorozcovs, P. R. Kumarakrishnan, A. Battle, and R. C. Swanson. A high-speed-modulated retroreflector for lasers using an acoustooptic modulator. *Can. J. Phys.*, 81:625–638, 2003.

[67] M. S. Safronova, C. J. Williams, and C. W. Clark. Relativistic many-body calculations of electric-dipole matrix elements, lifetimes, and polarizabilities in rubidium. *Phys. Rev. A*, 69:022509, 2004.

[68] M. S. Safronova and U. I. Safronova. Critically evaluated theoretical energies, lifetimes, hyperfine constants, and multipole polarizabilities in ^{87}Rb. *Phys. Rev. A*, 83:052508, 2011.

[69] W. I. McAlexander, E. R. I. Abraham, and R. G. Hulet. Radiative lifetime of the $2p$ state of lithium. *Phys. Rev. A*, 54:R5–R8, 1996.

[70] R. F. Gutterres, C. Amiot, A. Fioretti, C. Gabbanini, M. Mazzoni, and

O. Dulieu. Determination of the ^{87}Rb $5p$ state dipole matrix element and radiative lifetime from the photoassociation spectroscopy of the rb_2 $0_g^-(P_{3/2})$ long-range state. *Phys. Rev. A*, 66:024502, 2002.

[71] C. E. Tanner, A. E. Livingston, R. J. Rafac, F. G. Serpa, and K. O'Kukla. Measurement of the 6p $^2P_{3/2}$ state lifetime in atomic cesium. *Phys. Rev. Lett.*, 69:2765–2767, 1992.

[72] L. Young, W. T. Hill III, S.J. Sibener, S. D. Price, C. E. Tanner, C. E. Wieman, and S. R. Leone. Precision lifetime measurements of Cs 6p $^2P_{1/2}$ and 6p $^2P_{3/2}$ levels by single-photon counting. *Phys. Rev. A*, 50:2174–2181, 1994.

[73] S. A. Blundell, W. R. Johnson, and J. Sapirstein. Relativistic all-order calculations of energies and matrix elements in cesium. *Phys. Rev. A*, 43:3407–3418, 1991.

[74] V. A. Dzuba, V. V. Flambaum, A. Ya. Krafmakher, and O. P. Sushkov. Summation of the high orders of perturbation theory in the correlation correction to the hyperfine structure and to the amplitudes of E1-transitions in the caesium atom. *Phys. Lett. A*, 142(6):373 – 377, 1989.

[75] S. Svanberg and S. Rydberg. Level crossing investigation of the 6p $^2P_{3/2}$ and 7p $^2P_{3/2}$ levels of Cs^{133}, Cs^{135}, and Cs^{137}. *Z. Physik*, 227:216–233, 1969.

[76] S. Rydberg and S. Svanberg. Investigation of the np $^2P_{3/2}$ level sequence in the Cs I spectrum by level crossing spectroscopy. *Phys. Scr.*, 5:209–212, 1972.

[77] J. Marek and P. Munster. Radiative lifetimes of excited states of rubidium up to quantum number n = 12. *J. Phys. B: Atom. Molec. Phys.*, 13:1731–1741, 1980.

[78] N. Bendali, H. T. Duong, and J. L. Vialle. High-resolution laser spectroscopy on the D1 and D2 lines of ^{39,40,41}K using RF modulated laser light. *J. Phys. B: Atom. Molec. Phys.*, 14:4231–4240, 1981.

[79] Y. C. Chen, K. Chiang, and S. R. Hartmann. Spectroscopic and relaxation character of the $^3P_0$–$^3H_4$ transition in LaF_3: Pr^{3+} measured by photon echoes. *Phys. Rev. B*, 21:40–47, 1980.

[80] R. Macfarlane and R.M. Shelby. Sub-kilohertz optical linewidths of the $^7F_0 \leftrightarrow {}^5D_0$ transition in $Y_2O_3 : Eu^{3+}$. *Opt. Comm.*, 39:169–171, 1981.

[81] P. C. Becker, H. L. Fragnito, C. H. Brito Cruz, R. L. Fork, J. E. Cunningham, J. E. Henry, and C. V. Shank. Femtosecond photon echoes from band-to-band transitions in GaAs. *Phys. Rev. Lett.*, 61:1647–1649, 1988.

[82] A. Flusber, T. Mossberg, and S.R. Hartmann. Excited-state photon-echo relaxation in Na vapor. *Opt. Comm.*, 24:207–210, 1978.

[83] C. K. N. Patel and R. E. Slusher. Photon echoes in gases. *Phys. Rev. Lett.*, 20:1087–1089, 1968.

[84] D. A. Wiersma. Coherent optical transient studies of dephasing and relaxation in electronic transitions of large molecules in the condensed phase. *Adv. Chem. Phys*, 47:421, 1981.

[85] G. W. Biedermann, H. J. McGuinness, A. V. Rakholia, Y.-Y. Jau, D. R. Wheeler, J. D. Sterk, and G. R. Burns. Atom interferometry in a warm vapor. *Phys. Rev. Lett.*, 118:163601, 2017.

[86] S. L. McCall and E. L. Hahn. Self-induced transparency. *Phys. Rev.*, 183:457–485, 1969.

[87] E. A. Rotberg, B. Barrett, S. Beattie, S. Chudasama, M. Weel, I. Chan, and A. Kumarakrishnan. Measurement of excited-state lifetime using two-pulse photon echoes in rubidium vapor. *J. Opt. Soc. Am. B*, 24:671–680, 2007.

[88] X. H. Qi, L. Yi, Q. L. Ma, D. W. Zhou, X. J. Zhou, and X. Z. Chen. Study of phase coherence degradation induced by a tapered semiconductor amplifier with frequency-modulated continuous-wave and pulsed seed lasers. *Appl. Opt.*, 48(22):4370–4374, 2009.

[89] F. C. Cruz, M. C. Stowe, and J. Ye. Tapered semiconductor amplifiers for optical frequency combs in the near infrared. *Opt. Lett.*, 31(9):1337–1339, 2006.

[90] A. Turlapov, A. Tonyushkin, and T. Sleator. Optical mask for laser-cooled atoms. *Phys. Rev. A*, 68:023408, 2003.

[91] A. Kumarakrishnan, U. Shim, S. B. Cahn, and T. Sleator. Ground-state grating echoes from Rb vapor at room temperature. *Phys. Rev. A*, 58:3868–3872, 1998.

[92] J. L. Cohen and P. R. Berman. Transit-time effects in coherent transient spectroscopy. *Phys. Rev. A*, 54(6):5256, 1996.

[93] J. E. Thomas and R. A. Forber. Transverse atomic motion in transient polarization phenomena. *Opt. Lett.*, 9(2):56–58, 1984.

[94] H. C. Beica, A. Pouliot, A. Carew, A. Vorozcovs, P. Dowling, G. Carlse, B. Barron, and A. Kumarakrishnan. Applications of auto-locked laser systems for precision metrology. *Proc. CAP Congress, Physics in Canada*, 74(2A):65, 2018.

[95] G. Carlse, A. Pouliot, T. Vacheresse, A. Carew, H. C. Beica, and A. Kumarakrishnan. Technique for in-situ measurement of magnetic sublevel populations in a magneto-optical trap based on free-expansion imaging. Conference on Coherence and Quantum Optics, Rochester, 2019.

[96] E. Paradis, B. Barrett, A. Kumarakrishnan, R. Zhang, and G. Raithel. Observation of superfluorescent emissions from laser-cooled atoms. *Phys. Rev. A*, 77:043419, 2008.

[97] T. Mikaelian, M. Weel, A. Kumarakrishnan, P. R. Battle, and R. C. Swanson. A high-speed retro-reflector for free-space communication based on electro-optic phase modulation. *Can. J. Phys.*, 81:639–650., 2003.

[98] C. Mok, M. Weel, E. Rotberg, and A. Kumarakrishnan. Design and construction of an efficient electro-optic modulator for laser spectroscopy. *Can. J. Phys.*, 84:775–786, 2006.

[99] B. Barrett, A. Carew, H. C. Beica, G. Carlse, and A. Kumarakrishnan. *Manual for PHYS 4061 and PHYS 4062.* 2018.

[100] S. Winter, C. Mok, and A. Kumarakrishnan. Tools for laser spectroscopy: The design and construction of a faraday isolator. *Can. J. Phys.*, 84:845–855, 2006.

[101] M. Weel and A. Kumarakrishnan. Laser-frequency stabilization using a lock-in amplifier. *Can. J. Phys.*, 80:1449–1458, 2002.

[102] K. Sowka, M. Weel, S. Cauchi, L. Cockins, and A. Kumarakrishnan. A home-built lock-in amplifier for laser frequency stabilization. *Can. J. Phys.*, 83:907–918, 2005.

[103] A Vorozcovs, M Weel, S. Beattie, S. Cauchi, and A. Kumarakrishnan. Measurements of temperature scaling laws in an optically dense magneto-optical trap. *J. Opt. Soc. Am. B*, 22:943–950, 2005.

[104] J. Bechhoefer and S. Wilson. Faster, cheaper, safer optical tweezers for the undergraduate laboratory. *Am. J. Phys.*, 70:393–400, 2002.

[105] T. T. Perkins, D. E. Smith, and S. Chu. Direct observation of tube-like motion of a single polymer chain. *Science*, 264:819–822, 1994.

[106] S. Henon, G. Lenormand, A. Richert, and F. Gallet. A new determination of the shear modulus of the human erythrocyte membrane using optical tweezers. *Biophys. J.*, 76:1145–1151, 1999.

[107] K. Lindquist, M. Stephens, and C. Wieman. Experimental and theoretical study of the vapor-cell zeeman optical trap. *Phys. Rev. A*, 46:4082, 1992.

[108] H. J. Metcalf and P. van der Straten. *Laser Cooling and Trapping*. Springer-Verlag, New York, 1999.

[109] C Monroe, W Swann, H Robinson, and C Wieman. Very cold trapped atoms in a vapor cell. *Phys. Rev. Lett.*, 65(13):1571, 1990.

[110] A. S. Mellish and A. C. Wilson. A simple laser cooling and trapping apparatus for undergraduate laboratories. *Am. J. Phys.*, 70:965–971, 2002.

[111] C. Wieman, G. Flowers, and S. Gilbert. Inexpensive laser cooling and trapping experiment for undergraduate laboratories. *Am. J. Phys.*, 63:317–330, 1995.

[112] K Gibble and S Chu. Laser-cooled cs frequency standard and a measurement of the frequency shift due to ultracold collisions. *Phys. Rev. Lett.*, 70:1771, 1993.

[113] K. E. Gibble, S. Kasapi, and S. Chu. Improved magneto-optic trapping in a vapor cell. *Opt. Lett.*, 17:526–528, 1992.

[114] T. Walker, D. Sesko, and C. Wieman. Collective behavior of optically trapped neutral atoms. *Phys. Rev. Lett.*, 64:408, 1990.

[115] W. Ketterle, K. B. Davis, M. A. Joffe, A. Martin, and D. E. Pritchard. High densities of cold atoms in a dark spontaneous-force optical trap. *Phys. Rev. Lett.*, 70:2253, 1993.

[116] C. D. Wallace, T. P. Dinneen, K. Y. N. Tan, A. Kumarakrishnan, P. L. Gould, and J. Javanainen. Measurements of temperature and spring constant in a magneto-optical trap. *J. Opt. Soc. Am. B*, 11:703–711, 1994.

[117] S. Chu, L. Hollberg, J. E. Bjorkholm, A. Cable, and A. Ashkin. Three-dimensional viscous confinement and cooling of atoms by resonance radiation pressure. *Phys. Rev. Lett.*, 55:48, 1985.

[118] I. Yavin, M. Weel, A. Andreyuk, and A. Kumarakrishnan. A calculation of the time-of-flight distribution of trapped atoms. *Am. J. Phys.*, 70:149–152., 2002.

[119] I. Yavin, T. Mikaelian, and A. Kumarakrishnan. Calculation of the transfer efficiency between dual magneto-optical traps and simulation of a ioffe trap for bose einstein condensation. *Can. J. Phys.*, 81:651–661, 2003.